Assessment of ASR-Affected Concrete Specimens via Vibration Testing and FE Model Updating

by

Dikshaiye Mathoora

B.Sc. E (Civil Engineering, University of New Brunswick, 2020)

A Thesis Submitted in Partial Fulfillment
of the Requirements for the Degree of

Master of Science in Engineering

in the Graduate Academic Unit of Civil Engineering

Supervisor: Kaveh Arjomandi, PhD, PEng, Department of Civil Engineering

Examining Board: Ashlee Hossack, PhD, PEng, Department of Civil Engineering
Alan Lloyd, PhD, PEng, Department of Civil Engineering
Mohsen Mohammadi, PhD, PEng, Department of Mechanical Engineering

This thesis is accepted by the
Dean of Graduate Studies

THE UNIVERSITY OF NEW BRUNSWICK

August 2026

©Dikshaiye Mathoora (2026)

ABSTRACT

This exploratory study evaluates the use of experimental and operational modal analysis (EMA and OMA) paired with a finite element modal model updating (FEMU) procedure for the recovery of damage proxy indicators for the Alkali Silica Reaction (ASR) in the form of Young's Modulus (MOE) values.

Laboratory testing performed on reactive and non-reactive ASR blocks yielded modal parameters on the ARTeMIS platform, and cross validated on custom Matlab scripts. The modal data obtained was used as optimisation parameter in an Isight controlled Abaqus finite element model on three different model types.

The results indicate that the modal analysis method tested depend heavily on test setup, equipment, and the specimen excitation with respect to both user and environmental sources. While frequency measurements were only reliable for the fundamental mode, the resulting FEMU representative stiffness proved to be a viable basis for comparative testing. Further physical and modal testing is necessary to fully validate these findings.

DEDICATION

To the One Above All.

To my Mother, who gave everything for me and supported me till the very end.

To my supervisor, Dr. Michael Thomas, who made concrete mixing the most fun activity, who also supported me until the end.

ACKNOWLEDGEMENTS

I acknowledge my current supervisor, Dr. Kaveh Arjomandi, who has been the structural load-bearing column of my academics since 2016, and who has guided my graduate endeavours through this multi-disciplinary study with patience and rigour in equal measure. I thank the technical staff of the University of New Brunswick, Dennis Connors, Andrew Sutherland, and Chris Forbes, who met every experimental need, however unconventional, with great patience and ingenuity. I offer my sincerest gratitude to the other professors who have guided me along the way, and have helped shape this thesis, and myself, to what they are today.

I also thank the late Dr. Michael Thomas, whose foundational work on the UNB exposure site provided the specimens and the institutional knowledge without which this thesis could not exist.

A special thanks to my dog, Montgomery, who was always present and snoring while I was working.

Table of Contents

ABSTRACT ..... **ii**

DEDICATION ..... **iii**

ACKNOWLEDGEMENTS ..... **iv**

Table of Contents ..... **v**

List of Tables ..... **x**

List of Figures ..... **xii**

List of Symbols, Nomenclature or Abbreviations ..... **xv**

1 Introduction **1**

1.1 Background and Motivation 1

1.2 Research Scope, Objectives & Limitations 4

1.2.1 Scope and Objectives 4

1.2.2 Limitations 5

1.3 Contributions 6

1.4 Thesis Layout 7

1.5 Disclaimer: Use of AI 7

2 Literature Review **9**

2.1 The Alkali Silica Reaction (ASR) 9

2.2 Experiments in Codes, Prescribed Approach towards ASR Determination 10

2.2.1 Codified approaches on length changes 10

2.2.2 ASR and Vibration 11

2.3 The Effects of ASR on the Properties of Concrete 12
2.4 Modelling Approaches of ASR in Literature 19
2.4.1 Micro / Mathematical Models 19
2.4.2 Meso Models 20
2.4.3 Macro Models 21
2.5 Vibration testing 23
2.5.1 Introduction 23
2.5.2 OMA 23
2.5.3 EMA 25
2.6 Modal Model Updating 28
2.7 Literature Review – Summary and Conclusion 31
2.7.1 Summary 31
2.7.2 Conclusion 32
3 Experimental Studies 33
3.1 Introduction 33
3.2 Specimens 33
3.3 Experiment Design 37
3.3.1 Orientation and layout 37
3.3.2 Experimental Regime 44
3.4 Summary and Conclusions 51
3.4.1 Summary 51

3.4.2 Conclusions 52

4 Modal Analysis 54

4.1 Expected Data Description from FE Model 54

4.2 Analysis Regime 57

4.2.1 Pre-Processing 58

4.2.2 Mode Selection 60

4.2.3 Validation 66

4.2.4 Matlab Cross-Validation 69

4.2.5 Final Analysis Sequence 75

4.3 Results 77

4.3.1 Frequency Results 77

4.3.2 Comparison of Frequency against Expansion 79

4.4 Discussion 82

4.4.1 Mixed Modes and Instrumentation Concerns 82

4.4.2 Input Excitation 84

4.4.3 Mode Order 84

4.4.4 Ending Remarks 85

4.5 Summary and Conclusions 86

4.5.1 Summary 86

4.5.2 Conclusions 87

5 Finite Element Modelling 90

5.1 Introduction 90

5.2 Preliminary Studies 90

5.2.1 Modelling assumptions 90

5.2.2 Model generation 91

5.2.3 Mesh convergence studies 92

5.3 Investigation of MOE on Eigenfrequencies 100

5.4 Conclusions of Preliminary Studies 102

5.5 The Finite Element Model Updating (FEMU) Process- Introduction 103

5.6 Finding a Suitable Algorithm 105

5.7 FE Models 109

5.7.1 Level 1: Single MOE Model 109

5.7.2 Level 2: Skin vs Core Model 110

5.8 Modelling Regime 112

5.8.1 Part 1: Data Table Approach 112

5.8.2 Part 2: 1 MOE – 1 NF optimisation 114

5.8.3 Part 3: Detailed Simulation Approach 115

5.9 Combined Results and Discussion 120

5.10 Discussion 125

5.10.1 Models 125

5.10.2 What the FEMU Step Contributes 127

5.10.3 Process Recommendations 128

5.11 Summary and Conclusion 129

6 Study Wise Conclusions and Summary 131

6.1 Summary of Experimental Findings 131

6.2 Evaluation of FEMU Process and Conclusions 133

6.2.1 The FEMU Process 133

6.2.2 Study Conclusions 134

6.3 Recommendations 136

6.4 Limitations 138

6.5 Future Works 140

6.5.1 Immediate Follow-up Tests 140

6.5.2 Second Campaign on Purpose Cast Specimens 141

6.5.3 Modelling Extensions 142

6.6 Avenues of Research and Application 143

Bibliography 145

Appendix A: Instrumentation 157

Appendix B: Modal Analysis Results – Block A 180

Appendix C: Level 1 Data Table 194

Curriculum Vitae

List of Tables

Table 2-1: Survey of Experiments, adapted from Mohammadi et al. (2020) 14

Table 2-2: Relative sensitivities of concrete properties with respect to ASR..... 18

Table 2-3: Summary of studies in OMA..... 25

Table 2-4: Summary of studies in EMA 27

Table 2-5: Summary of studies on FEMU 30

Table 3-1: UNB exposure site block details 34

Table 3-2: Test methods used 48

Table 4-1: FE analysis results: mode shapes and modal frequencies of a typical block. . 55

Table 4-2: Analysis methods available in ARTeMIS 57

Table 4-3: Automatic estimator results: Frequency Domain 63

Table 4-4: Automatic estimator results: Time Domain 63

Table 4-5: S1 over S2 Matlab selection peaks from ARTeMIS 72

Table 4-6: Modal testing results: Modal Frequencies..... 78

Table 4-7: Summary of frequency to strain comparison values 81

Table 5-1: Mesh convergence study on the effects of mesh element density..... 93

Table 5-2: Comparison of mode shapes and frequencies for the 125 and 21952 element models 95

Table 5-3: Comparison of Hex element types against EF results 99

Table 5-4: Tabulated values of differences in EF with changing MOEs..... 101

Table 5-5: Part 1 Modelling results, reactive blocks 114

Table 5-6: Part 1 modelling results, non-reactive blocks 114

Table 5-7: Part 2 modelling results 115
Table 5-8: Part 3 results: Best fit 2 MOE pairing per block 120
Table 5-9: Combined modelling results 121
Table 5-10: MOE result table with strain and EF1 data 124
Table A1: Sensor inventory 159
Table A2: Excitation hardware 159
Table A3: Data acquisition inventory 159
Table A4: Mounts and consumables 160
Table A5: Software inventory 160
Table A6: Hammer Spectral Densities 176
Table A7: X-channel spectral densities 177
Table B1: Power Spectrum Densities- block A 181
Table B2: Combined estimator selection Table for block A 186
Table B3: Pre-selection of OMA Basketball mode shapes 189
Table B4: Pre-selection of EMA – Hv Mode shapes 190
Table B5: Pre-selection of EMA H1 mode shapes 191
Table B6: Selected mode Table 192
Table C1: Level 1 Reference Data Table 195

List of Figures

Figure 1-1: Exploratory study poise. 4

Figure 2-1: Compressive strengths of various concretes under normal and ASR induced conditions (Munir et al. 2018) 16

Figure 2-2: View of FE model of concrete sample with a zoom in on aggregates. (Comby-Peyrot et al., 2009)..... 20

Figure 3-1: UNB exposure site 35

Figure 3-2: ASR expansion data for selected blocks 36

Figure 3-3: Simple Support setup (a), Install process (b) 39

Figure 3-4: Accelerometer configurations for simple support, (a) In line 3. (b) Evenly spaced 11..... 40

Figure 3-5: View of stand-up block setup with (a) showing direct ground contact and (b) showing insulation between the ground and the block. 42

Figure 3-6: View of the underside of the block showing the three steel supports being set. 42

Figure 3-7: Typical test setup for OMA (a) and EMA (b)..... 44

Figure 3-8: Impact hammer and accompanying tips..... 46

Figure 3-9: EMA trial operation 47

Figure 3-10: SVD plot of OMA setup with Ambient excitation only 50

Figure 3-11: SVD plot of OMA setup with Forced Ambient excitation 50

Figure 4-1: Pre-processing step SVD line for block A with harmonic peak detection overlaid 58

Figure 4-2: Zoom in section of block A SVD plot showing frequency range between 1 and 2 kHz. 59
Figure 4-3: Block A EFDD automatic selection plot..... 65
Figure 4-4: Block A SSI-UPCx automatic selection plot 65
Figure 4-5: MAC diagrams for FDD and EFDD for block A basketball automatic selections..... 67
Figure 4-6: Initial modal model. As tested (left), in ARTeMIS (right) 68
Figure 4-7: Refined model shown for mode at 189 Hz showing full motion on original geometry (OG) in a. and rigid body removed (RBR) in b. 68
Figure 4-8: Matlab mode shape reconstruction for block A 189 Hz Ambient test..... 69
Figure 4-9: Cross MAC plot from Matlab for block A OMA Ambient vs Basketball on EFDD 70
Figure 4-10: S1 / S2 Matlab rendered validation for block A Basketball 72
Figure 4-11: Mode Shapes obtained from the block A Basketball S1 over S2 investigation. 73
Figure 4-12: MAC diagram for the block A Basketball S1 over S2 investigation in ARTeMIS..... 74
Figure 4-13: Modes at 15 and 74 Hz for block A for Basketball with MAC diagram 77
Figure 4-14: Bar chart of first measured frequencies (Hz) 79
Figure 4-15: Scatter plot of normalised frequency and expansion strains to block AC ... 81
Figure 5-1: Variation of EF with different MOE..... 101
Figure 5-2: Overview of Isight components. 104

Figure 5-3: Variation of algorithm performance for block A level 2 skin MOE optimisation..... 108
Figure 5-4: Level 1 Single MOE model with boundary conditions shown 110
Figure 5-5: Level 2 models. symmetric variant (a). Asymmetric variant (b). 111
Figure 5-6: Erms Heatmap for Part 3 Modelling results..... 118
Figure 5-7: Erms heatmap for Level 3 modelling for first two mode pairs 119
Figure 5-8: Relationship between NF and 1 MOE values from all modelling parts 122
Figure 5-9: NF1 - MOE to strain map 125
Figure 5-10: Multi MOE model..... 126
Figure A1: Sensor layout on specimens..... 158
Figure A2: Experimental considerations 162
Figure A3: Accelerometer - mounting type deviations (PCB Piezotronics, 2004)..... 164
Figure A4: Typical Mounting Pad 165
Figure A5: Adhesive experiment on a surplus concrete beam. 167
Figure A6: Adhesive removal experiment. Solvents in (a), Torque in (b). 168
Figure A7: Accelerometer pad removal..... 169
Figure A8: Accelerometer pad cleanup step. Rethreading procedure shown in (a) and residue removal in (b). 170
Figure A9: Crack protection of the concrete specimens. 172
Figure A10: Impact hammer response curves on steel mass (PCB Piezotronics, 2025) 173
Figure A11: Accelerometer time data window for hard tip 174

List of Symbols, Nomenclature or Abbreviations

Contextual Symbols

ε: Epsilon, denoting expansion value.

ξ: Xi, denoting damping ratio.

Ø: Diameter symbol

Δ: Delta, denotes a change, usually with respect to different values.

Material abbreviations

AAR: Alkali Aggregate Reaction. Used interchangeably with ASR in this text.

ASR: Alkali Silica Reaction.

ACR: Alkali Carbonate Reaction

FE: Finite Element

FEM: Finite Element Method

FEMU: Finite Element Model Updating

SCM: Supplementary Cementitious Materials

MOE: Modulus of Elasticity

MOR: Modulus of Rupture

Vibration abbreviations

NF: Natural (measured) frequency from a test specimen as obtained from physical measurements

EF: Eigen (mathematical) Frequency as obtained from a finite element model

EMA: Experimental Modal Analysis

OMA: Operational Modal Analysis

DAQ: Data acquisition system

FRF: Frequency response function

PSD: power spectral density

SVD: Singular value decomposition

MAC: Modal assurance criterion

FDD: Frequency domain decomposition

EFDD: Enhanced FDD

CFDD: Curve fit FDD

SSI: Stochastic subspace identification

PC: Principal component

UPC: Unweighted principal component

UPCx: Extended unweighted principal component

CMIF: Complex mode indicator function

RFPz: Rational fraction polynomial in the z domain

OG: Original geometry, used int the context of the model geometry

RBR: Rigid body removed, in the context of the model geometry, denoting the removal of rigid body motion through mathematical operations to measured and slave nodes.

Nomenclature

Hammer: The hammer used in this study refers to a PCB 086D20 short-sledge impulse hammer used in EMA.

Run: A run, in the context of model updating refers to a complete optimisation set executed for a single specimen.

Iteration: An iteration refers to a specific FE model evaluation within a given run.

1 Introduction

This chapter introduces the research problem, sets out the research questions, and locates the thesis within three streams of literature whose intersection it occupies.

Section 1.1 presents the motivation: the well-documented ASR damage in service structures and the comparatively under-developed framework for non-destructive monitoring of that damage at field-specimen scale and develops the bridging argument that organises the thesis as a whole: the proposition that a coupled modal testing and FEMU pipeline can join three previously parallel research streams into a single methodology. Section 1.2 states the research questions, scope, and limitations. Section 1.3 lists the contributions. Section 1.4 lays out the chapter arrangement. Section 1.5 is the disclaimer on the use of AI.

1.1 Background and Motivation

Alkali silica reaction (ASR) was first reported in the 1940s by Thomas Stanton at the California State Division of Highways (Stanton, 1940). Since then, numerous cases of ASR have been reported across the world in North America, United Kingdom, Europe, Russia, Japan, China, India, Australia and New Zealand (Sims & Poole, 2017). One case of major significance in Canada is the Mactaquac Dam which has experienced serious serviceability and expansion problems due to ASR occurring inside the main water-retaining structure (NB Power, 2016; Shrimer, 2005, p. 3).

Test methods for ASR used at the time of construction on the materials (Portland cement, aggregate, or supplementary cementitious materials, SCM) of a particular project may approve the materials but the structure can show signs of distress years or even

decades after being built. For example, the Mactaquac dam was finished in 1968 but started showing signs of ASR in the 1970s (Beaman, 2005). This indicates that standards or test methods may change over time and improve detection rates of defective material and that there are existing structures that were thought to be ASR free but now exhibit ASR symptoms.

There have been investigations across Canada (C. A. Rogers, 1993) and specifically in the provinces of Ontario (C. Rogers et al., 2000), Alberta-Saskatchewan - Manitoba (Roy & Morrison, 2000), British Columbia (Shrimer, 2000), Quebec (Bérubé et al., 2000), Nova Scotia (Langley, 2000) and New Brunswick (Demerchant et al., 2000) that provide the location and types of reactive aggregates in each province, concrete prism test results and analysis results of provincial cements.

These investigations also show that after the initial diagnosis of ASR through field inspections for visual signs and laboratory petrographic examination of collected samples, the prognosis of the structures is carried out through periodic or continuous in-situ monitoring of the deformations, stresses, and displacements within the structures. Such measurements are then factored in finite element (FE) or numerical models for the structural evaluation of the structure and prediction of ASR induced expansion and structural behaviour (Bérubé et al., 2000).

The sensitivity of vibration-based parameters for the detection of internal swelling reactions was established by Siegert at al. (2005). Their work showed a 12 to 20% reduction in stiffness for manufactured ASR concrete specimens, with the stiffness back calculated from resonant frequency monitoring. This work provided a strong basis for the use of specimen frequencies as proxy for ASR evaluation through a material physical

property. Furthermore, Malone et al. (2021), expanded on this research area through the evaluation of linear and non-linear resonance techniques on manufactured ASR specimens. They found that ASR initiation was very prominent for non-linear methods, but linear resonant frequency shifts are reliable in capturing the overall stiffness loss in concrete.

A Finite Element Model comparison for use in ASR investigation (F. Barbosa & Cremona, 2002) has been carried out at the Laboratoire central des ponts et chaussées (LCPC) and was aimed at developing a framework for comparing the operational modal analysis (OMA) frequencies of beams affected by ASR against FE model frequencies. The programme was run during a period of 1 year, but no conclusive test outcomes were reported in terms of ASR effects on frequencies.

This study aims at combining the investigative studies of Siegert and Barbosa, resulting in an evaluation of operational and experimental modal analysis (OMA and EMA) on ASR reactive vs nonreactive specimens, combined with a damage proxy value recovery from Finite Element Model Updating (FEMU) using the modal parameters. Such a relationship is illustrated in Figure 1-1. The main difference in this study as compared to others in literature is that the specimens used are mature and show signs of a near complete to fully complete expansion, the modal analysis pipeline contains a test comparison between operational and experimental modal analysis, and the use of FEMU for an ASR damage indicator (proxy).

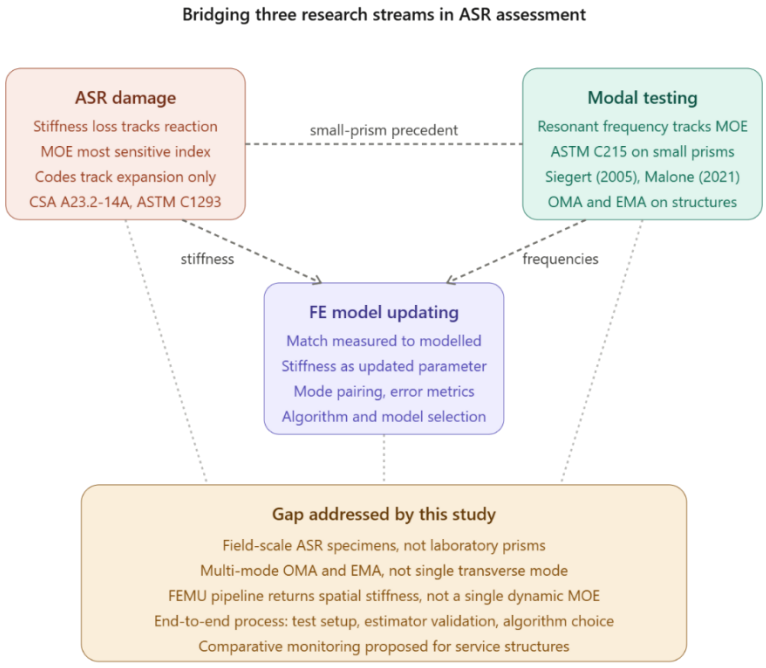


Figure 1-1: Exploratory study poise.

1.2 Research Scope, Objectives & Limitations

1.2.1 Scope and Objectives

This research aims at answering two core questions:

1. Is modal testing able to differentiate ASR reactivity within concrete and if so, which of operational or experimental modal analysis is better suited?
2. Is finite element model updating capable of incorporating modal test results to provide a measurement of ASR degradation within concrete specimens?

The feasibility of finite element model updating will be determined for modal parameter-based updating. The challenge in this study is twofold; first is the development of a test protocol for the modal testing and analysis of the available specimens, and second, the model updating process within the Abaqus framework.

The expected results from modal testing are the modal properties of the specimens and a conclusion on the viability of either modal test methods in identifying those modal properties. The result from the model updating section is the viability of the modal model updating process in detecting ASR given test results obtained. Given that this study is exploratory in nature, the following subtopics will be investigated on the way to answering the research questions.

- The challenges to be expected and mitigations of such challenges towards experimenting on nonstandard ASR concrete specimens.
- The issues arising from the data analysis and processing required for validation of data, should the data be incomplete or noisy.
- The process of producing a model for updating, including implementation considerations and methods.

The proposed methodology in this study is as follows:

- Literature investigation for the behaviour of ASR to be modelled, methods of modal testing and modelling.
- Modal testing of the concrete specimens with tools and commercial software available. Analysis of modal data complemented with purpose-built code.
- Model creation and updating with commercial Abaqus-engine based software available.
- Comparison of results and demonstration of proposed process effectiveness.

1.2.2 Limitations

The limitations of this study come from two main areas. The size of the specimen population, and the tools available. The number of specimens to be tested is less than what is required for a normal distribution, therefore the statistical range is irrelevant. The specimens are provided with only information about their mix designs and expansion

data. The lack of tracked material properties is detrimental for the cross comparison of modal properties to degradation, which would have supported this study. The exploration is bounded throughout by a non-destructive constraint that follows directly from the institutional context of the specimens. The blocks tested in this thesis are part of the ongoing ASR exposure-site programme at the University of New Brunswick. They are subject to continuing periodic measurement of expansion strain and visual condition; they cannot be machined, drilled, cored, or otherwise altered in any way that would interfere with that ongoing measurement programme or that would compromise the long-term value of the specimens to the institution.

The tools available, tabulated in Appendix A-2, for the programme are suitable for an exploration but are not representative of the entirety of the modal testing process or finite element modelling process. Therefore, this study is to be understood as a preliminary exploration and not a comprehensive investigation.

1.3 Contributions

This study contributes the following findings and workflows:

1. A non-destructive vibration testing protocol for non-alterable, field scale ASR specimens.
2. A direct OMA-EMA comparison on the same specimens, revealing frequency band specialisation between the two test methods, attributable to differences in input excitation.
3. A documented FEMU pipeline that converts the first measured frequency to a recovered effective MOE for a given specimen.
4. A comparative monitoring framework as the application of the FEMU pipeline for ASR monitoring instead of diagnosis with snapshot measurements.

1.4 Thesis Layout

The thesis is arranged, explaining the FEMU process as follows:

Chapter 2 is the literature review performed to investigate the ASR reaction, modal analysis and testing, and FE modelling and updating.

Chapter 3 covers the experimental studies. The specimens, the design of the experiment and the final experimental conditions are discussed.

Chapter 4 discusses the modal analysis of this study. The analysis pipeline is presented and discussed, justifying any analysis choices where appropriate, resulting in a set of modal data.

Chapter 5 discusses the finite element modelling process in two sections. The first is the preliminary finite element analysis performed to obtain the expected mode shapes for mode shape picking. The second is the finite element model updating process, where a model and optimisation algorithm framework is built and used to obtain ASR proxy data.

Chapter 6 is the final conclusion of this study whereby all the summary points are reiterated, and conclusions are drawn from the entirety of the study. Recommendations are made as well as any possible future works based on this study's direction.

1.5 Disclaimer: Use of AI

Generative artificial-intelligence agents, primarily ChatGPT, Claude, and Gemini, were used in the preparation of this thesis in a defined and supervised manner. They were used for text review, including grammar, verbiage, written voice, and tone checks on text drafted by the author; for brainstorming and comparative reasoning when evaluating new

instruments, software packages, and analysis methods, with the agents serving as discussion partners rather than as sources; as an extended search engine, after conventional browser-based search, for clarifying terminology and pointing to additional literature; and for coding assistance while writing the MATLAB scripts used for SVD computation, peak picking, and MAC visualisation. Imagery generated by AI agents appears in this thesis only in idea-presentation contexts; all photographs, plots, and presented data are original and reflect the author's own measurements, modelling, or analysis.

AI was used as a tool, under the author's full supervision. No information was copied from any agent without being cross-examined for correctness and fully understood. No section of this thesis was written by an AI agent unsupervised, and no factual claim is sourced to an AI agent.

2 Literature Review

2.1 The Alkali Silica Reaction (ASR)

Alkali silica reaction (ASR) is a subcategory of alkali aggregate reaction (AAR) alongside alkali carbonate reaction (ACR). AAR is the term used to classify deleterious reactions occurring in concrete or mortar whereby the components of the aggregates react with the hydroxyl ions of the alkalis present in the pore solution to form secondary reaction products. These products are generally expansive in nature and contribute to premature deterioration problems and consequent loss of service (Fournier & Bérubé, 2000)

ACR has been documented in only a few cases throughout Canada in southern and eastern Ontario and is the reaction between the alkalis in the binder and carbonates found in certain dolomitic limestone aggregates (CSA, 2005). Gillott and Swenson characterised ACR expansions as being the result of saturation of dry clay minerals following dedolomization of the dolomitic limestones (Gillott & Swenson, 1969). ASR on the other hand is far more common in Canada and in the world with over more than 50 affected countries (Sims & Poole, 2017). ASR occurs when reactive silica from the aggregates reacts with the alkali in the binder to form expansive silica gel consequently causing the concrete to deteriorate.

ACR was defined separately from ASR given the two different accepted mechanisms of occurrence outlined previously but Grattan-Bellew et al. (2010) found presence of ASR gel in ACR affected concrete. Through their research, they tested dolomitic samples from Kingston, Ontario and found that ACR was accompanied by

ASR with a slight modification to the ASR gel formed; the new gel consisting of calcium magnesium aluminium silicate hydrate as opposed to the typical sodium or potassium calcium silicate hydrate gel in ASR. They therefore concluded that ACR is equal to ASR (Grattan-Bellew et al., 2010; A. B. Poole, 2017). The scope of this project is the assessment of ASR in concrete, not ACR. Therefore, in this document, the term alkali aggregate reaction (AAR) is used interchangeably with alkali silica reaction (ASR).

2.2 Experiments in Codes, Prescribed Approach towards ASR Determination

2.2.1 Codified approaches on length changes

The Canadian Standards Association (CSA) and the American Society for the Testing and Materials, ASTM together provide two principal test pairs for ASR. The first is the concrete prism test of CSA A23.2-14A (CSA, 2019a), similar to ASTM C1293 (ASTM, 2020), in which at least three concrete prisms with cross-section 75 by 75 millimetres and length between 275 and 405 millimetres are immersed in a 1-molar sodium hydroxide (NaOH) solution at 38 degrees Celsius for one year while their expansion is measured at intervals with a length comparator. The second is the accelerated mortar-bar test of CSA A23.2-25A (CSA, 2019b), similar to ASTM C1260 (ASTM, 2021), in which mortar bars of 25.4 by 25.4 by 254 millimetres are produced per ASTM C490, stored at 80 degrees Celsius, made with aggregate of 5-millimetre maximum size, and tested over 14 days with three length readings. The European counterpart to CSA and ASTM, RILEM (2000) describes similar procedures with the same dimensions and storage conditions.

Both test pairs are confirmatory for a candidate material choice rather than a diagnostic for an in-service structure. They are appropriate for screening materials before construction; they are not designed to assess ASR damage in service structures, where the boundary conditions, environmental exposure history, and reaction state differ in kind from the controlled laboratory conditioning of the standard tests.

2.2.2 ASR and Vibration

The ASTM C215 (ASTM International, 2019) standard bridges codified approaches and frequency value recovery for concrete. It covers measurement of the fundamental transverse, longitudinal, and torsional resonant frequencies of standard concrete laboratory specimens via forced resonance (shaker/driver) or impact resonance (steel ball impactor) with basic frequency decomposition (BFD) and provides empirical equations and correction factors to back-calculate the dynamic MOE. This method, together with the nonlinear BFD formulation of Lesnicki et al. (2013), has been used to categorise ASR evolution in concrete. Only the first NF is measured; no mode shape, damping, or other modal properties are obtained.

Two studies drawing on these principles are highlighted: Siegert et al. (2005) on resonant frequency monitoring of ASR-damaged concrete, and Malone et al. (2021) on resonance techniques for ASR damage quantification. Siegert et al. tracked NF1 through NF3 of purpose-made 0.5 × 0.25 × 3 m beams (4 reactive, 2 nonreactive) over about a year under controlled exposure, exciting them with an impact sledgehammer and extracting frequencies via BFD; MOE was back-calculated from rigid-body beam-frequency formulae. They found a maximum 20% stiffness reduction, fully recovered by

the end of the tests, and concluded that other effects may have been at play and that such vibration studies require careful interpretation of concrete-environment interactions. Malone et al. tested prisms following ASTM C215 with linear and nonlinear resonance techniques, taking the lowest-amplitude peak of the NIRAS acceleration-vs-frequency curve as the linear datum. They found nonlinear analysis more sensitive: it captured effects from both fine and coarse aggregate, whereas the linear method was sensitive mostly to the coarse aggregate and ineffective in late-stage ASR. Their main hypothesis was that the nonlinear method, being more sensitive to crack formation, can support damage quantification without a baseline, provided parameters are calibrated to specimen dimensions.

Since ASR is shown to be quantifiable through vibration methods, the next step, in Section 2.3 and 2.4 is to identify a concrete property usable as a proxy for damage quantification without invasive laboratory tests.

2.3 The Effects of ASR on the Properties of Concrete

The alkali silica reaction, by its very nature, changes the concrete matrix and therefore alters its mechanical behaviour. Several studies have been conducted to demonstrate the changes in mechanical properties of ASR affected concrete, and a survey of those is found in Table 2-1 which has been adapted from (Mohammadi et al., 2020) to reflect additional details such as concrete mix design and testing lengths and conditions.

The right-hand columns indicate which mechanical properties are reported in each study: compressive strength (C), modulus of elasticity (E), direct tensile strength (T), splitting tensile strength (S), modulus of rupture (R), Poisson's ratio (ν), and dynamic

modulus (D). The experiments surveyed cannot be directly compared to each other as the materials used, the type of specimens, the exposure conditions and the type of tests vary greatly between studies. Therefore, only a general overview of the testing results can be provided per concrete property tested, bearing in mind that this section is to find a suitably responsive concrete property that is indicative of ASR damage.

Table 2-1: Survey of Experiments, adapted from Mohammadi et al. (2020)

Investigation	Mix design (Normal Concrete)	Conditioning		Concrete Property Investigated							
	W/CM \ Max % $Na_{(eq)}$	Curing Time	Specimen Conditioning Time (for relevant property test)								
	Cement: Fines: Coarse Aggregate (Ag.).	Curing Conditions	Conditioning	Length Change Measurement Type	C	E	T	S	R	v	D
Marzouk and Langdon (2003)	0.45\ 1.25 355/790/1040	1d water	2 & 12 weeks 1 M NaOH	CSA A23.2-25A AMBT -	**x**	**x**	**x**		**x**		
Islam and Ghafoori (2018)	0.45(0.47used) \ 0.84 1: 2.15 cement to Ag.	1 d 20 & 80^{0}C water	4 & 26 weeks 20 & 80 ^{0}C ,1 N NaOH	ASTM C12601"x1"*10" MB		**x**					
Islam and Ghafoori (2015)	0.45(0.47 used) \ 0.84 1: 2.15 cement to Ag.	1 d 20 & 80 ^{0}C water	4,8,13,26 weeks 20 & 80 ^{0}C 1 N NaOH	ASTM C12601"x1"*10" MB ASTM C1293 75x75x250mm	**x**						
Barbosa et al. (2018)	- -	- -	- -	- -	**x**						
Li et al. (2016)	0.2 \ 0.88 1:1.25 cement to fines	1 d 80^{0}C water	1 & 4 weeks 80^{0}C 1 N NaOH	ASTM C12601"x1"*10" MB	**x**				**x**		
Shi et al. (2017)	0.47 W/CM (slag) 1:2.25 slag to fines	1d/1d water/steam	1/14/28d 80^{0}C 1 M NaOH	ASTM C1260 1"x1"*10" MB	**x**				**x**		
Munir et al. (2018)	0.47/0.85 1:2.25 cement to Ag.	varies varies	1&6 months varies	varies varies	**x**				**x**		
Yurdas et al. (2013)	0.5\1.15 1:3 cement to fines	28d 20^{0}C sealed	100d 60^{0}C 95% RH	40x40x160mm MB		**x**			**x**	**x**	

Investigation	Mix design (Normal Concrete)	Conditioning		Concrete Property Investigated							
	W/CM \ Max % $Na_{(eq)}$	Curing Time	Specimen Conditioning Time (for relevant property test)								
	Cement: Fines: Coarse Aggregate (Ag.).	Curing Conditions	Conditioning	Length Change Measurement Type	C	E	T	S	R	v	D
Ahmed et al. (2003)	0.5\1.75 1:1.3:3.2	28d 20 ^{0}C water	11 months 38^{0}C water	100x100x500 prisms (DEMEC) 150x300 cylinders	**x**	**x**	**x**	**x**	**x**		
Giaccio et al. (2008)	0.42\1.25 420/710/1090	28d 38^{0}C sealed	varies to 745d 38^{0}C sealed	ASTM C1293 75x75x250mm	**x**	**x**			**x**	**x**	
Tanzer et al. (2017)	0.4 W/SCM (slag) 1:3 slag to Ag.	1d 20^{0}C 65% RH	10 times first 56d, then per 28 d until 224d 40^{0}C 100%RH	40x40x160mm MB							**x**
Na et al. (2016)	0.5\0.9 330/754/1041	1d 23^{0}C 100%RH	0,14,28,42,56d 80^{0}C 1N NaOH	ASTM C1260 1"x1"x10" MB	**x**	**x**					

The compressive strength is found to be the most surveyed property in terms of ASR studies, followed by the moduli of concrete. The compressive strength of ASR-affected concrete can be used as a first indicator of ASR progression regardless of aggregate type as shown in Figure 2-1, presenting the compressive strengths of various types of aggregates in concretes under normal and ASR induced conditions. The figure shows a net decrease in compressive strengths of ASR affected specimens regardless of aggregates used, though the decrease is not by a similar proportion for all concretes. However, Ahmed et al. (2003), and Saouma and Perotti (2006) argue that compressive strength is not a sensitive indicator of ASR expansion as compared to other material properties such as MOE and tensile strength. This occurs when ASR expansion does not cause significant damage compared to the hydration of the concrete or if ASR has already stopped while the concrete is hydrating, causing significant material recovery.

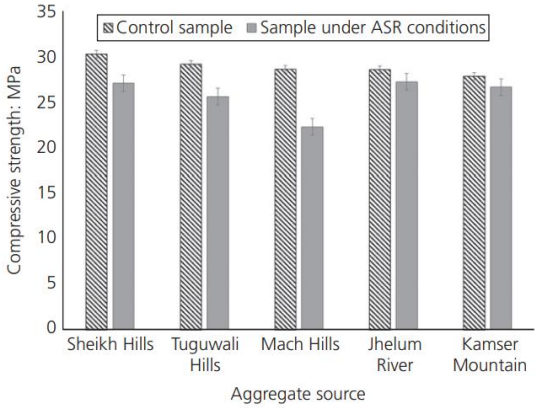


Figure 2-1: Compressive strengths of various concretes under normal and ASR induced conditions (Munir et al. 2018)

This effect is also shown in Marzouk and Langdon's (2003) results of compressive strengths and MOE measured on samples at 28 days and 12 weeks of

conditioning. In their study, normal and high strength concrete, cured in water and sodium hydroxide solution, were tested for compressive strength, MOE, MOR, and tensile strength. While the effects on the mechanical properties of high strength concrete were minimal, the changes in mechanical properties on the normal concrete were significant on moderately and highly reactive types of aggregates used. The compressive strength of the moderately reactive aggregate remained unchanged while the MOE decreased by 20% and for the highly reactive aggregates, the losses in compressive strength and MOE was 28 and 80% respectively. Furthermore, the change in MOR on the concretes was found to be negligible, contrary to the tensile strengths which were found to be highly sensitive to ASR with a decrease of 37 and 31 % for the highly and moderately reactive aggregates.

Studies by Islam et al. on mortar bars for compression loss (2015) and for MOE loss (2018) is shown that the change in MOE is consistently higher than for the same change in compressive strength, thereby indicating a higher sensitivity of MOE to ASR than compressive strength. While some other properties of concrete such as dynamic modulus (Tänzer et al., 2017), and Poisson's ratio (Maruyama et al., 2014), have been investigated as a function of ASR expansion or time elapsed, their susceptibility to ASR cannot be established because of a lack of thorough investigations.

A summary compiling a relative range of changes for concrete properties is tabulated in Table 2-2. The ranges have been selected to reflect those encountered in standard concrete as far as possible. The table shows that there is a variability in terms of concrete property that needs to be chosen as ASR comparator. The MOR is also discarded on the basis of conflicting or incomplete test data. The tensile strength and

MOE remain strong contenders for the ASR comparison and their modelling implementation will determine which one is to be used for this study. Since measurement is not a concern for this study, the direct tensile strength and the MOE are strong contenders as ASR proxy values.

Table 2-2: Relative sensitivities of concrete properties with respect to ASR

Index	**Sensitivity**	**Change Magnitude (%) | Source**
Compressive Strength	Least	Negligible to -28 for moderately to highly reactive aggregates | (Marzouk and Langdon. 2003) Negligible | (Ahmed et al. 2003)
MOR (Flexural Strength)	Fair	None to low | (Marzouk and Langdon 2003) -72 to -90 | (Ahmed et al. 2003)
Tensile Strength	High	-31 to -37 for moderately to highly reactive aggregates. | (Marzouk and Langdon. 2003) -50 to -80 significant reductions | (Ahmed et al. 2003)
MOE	Highest	-20 to -80 for moderate to highly reactive aggregates. | (Marzouk and Langdon. 2003) -50 to -80 | (Ahmed et al. 2003)

The materials literature converges on the MOE as the most sensitive measurable index of ASR damage, as for the direct tensile strength. The literature does not, however, address the recovery of MOE from non-destructive vibration measurement at field-specimen scale.

While the beam-frequency formulae, as employed by Siegert et al. (2005) to back calculate the MOE would have offered a closed formed solution, the applicability of these formulae on nonstandard specimens is questionable. Section 2.4 addresses this issue through an investigation into the modelling techniques employed for ASR, with the end goal of obtaining the MOE values from a finite element (FE) engine.

2.4 Modelling Approaches of ASR in Literature

ASR models are classified by scale (micro, meso, and macro), by physics type (chemical, mechanical, or coupled) or by input parameters (expansion, pressure) (Esposito & Hendriks, 2019, 2012; T. Pan et al., 2018; Revoredo et al., 2021). An overview of various modelling scales is provided in this section in order to justify the FE engine model.

2.4.1 Micro / Mathematical Models

These models aim at providing a better understanding of the reaction itself and seldom find applications in large scale structural applications other than for research of the reaction itself. The mathematical models (Bazant & Steffens, 2000; V. E. Saouma et al., 2015) reviewed showed that such models focus on the kinetics of the reaction with respect to particle size and distribution, paired with water movements. The first model related the development of the swelling pressure around an aggregate particle, the effect of particle size and the pessimum size for an aggregate. The second model provided a better understanding of the estimation of residual reaction components at the end of the reaction, of the influence of the initial concentration of the reaction constituents in the final gel concentration, and the fact that alkalis limit the reaction more than the supply of silica, amongst others.

These models would be too complex for implementing an MOE recovery framework paired with modal data and therefore other avenues are explored.

2.4.2 Meso Models

These models focus on the aggregate level of the reaction and consider the aggregate size distribution and location (J. Pan et al., 2012). One such model investigated by Comby-Peyrot et al. (2009); their model is a three-dimensional finite element (FE) model based on velocity-pressure formulation. It was created to have as much realism possible concerning the heterogeneity of the aggregate distribution within the concrete matrix, complete with a sensitivity analysis on the aggregate volume, distribution and diameter on the modelled damage of ASR. Their finite element model, as shown in Figure 2-2, is an accurate depiction of a skeleton of aggregates. Based on a mix design calculation of particles in this representative sample, they reached 87 443 495 particles of coarse to fine aggregates within a 70 x 70 x 280 mm sample. Comby-Peyrot et al. modelled the concrete as a two-phase material consisting of coarse aggregates within a mortar paste instead to limit the number of particles to 935 linear tetrahedral elements. The arrangement is shown in Figure 2-2.

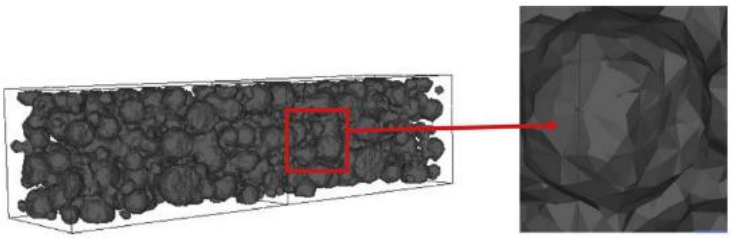


Figure 2-2: View of FE model of concrete sample with a zoom in on aggregates. (Comby-Peyrot et al., 2009)

The material properties used to calibrate the model were obtained through laboratory testing. This type of model requires an intensive ‘pick and place’ phase while

modelling the sample in the FE engine. While the variation of the MOE and the tracking of ASR could be achieved within this model, the labour and data required for the FE modelling is a strong deterrent given the scope and limitations of this study.

2.4.3 Macro Models

While the microscopic models aim at understanding and predicting the reaction from either chemical (kinetic) or mechanical perspectives, macroscopic models try to emulate real life scenarios to predict structural distress (Guo et al., 2019; Sanchez et al., 2014). The main model of this model scale is the parametric (CTMR) model, labelled as such since it uses input factors such as compressive stress, C, temperature, T, moisture, M, and aggregate reactivity, R. The CTMR model is a refinement of the previous parametric models in the field whereby the chemistry of the reaction was not overly considered, and the strain was a resultant of an applied temperature increase (J. W. Pan et al., 2012). The formulation for an example model by Leger et al (1996) uses the following strain equations for ASR modelling.

$$\varepsilon_{AAR}^{element}(t) = \beta^{element}(t) * (F_c(\sigma, t) * F_t(t) * F_M(t) * F_R(t))^{element} \quad (2\text{-}1)$$

$$\varepsilon_{AAR}^{element}(t) = \beta^{element}(t) * (CTMR)^{element} \quad (2\text{-}2)$$

Where F are normalised factors for each of the CTMR parameters denoted through subscripts, t is time, and σ is the stress state of the element. The term β is a calibration factor for the model for the adjustment of observed compared to calculated displacements and is calibrated on a per model basis. Furthermore, in terms of parameters needed for the analysis, used in the development of the effective material matrix, it is

noted that the following were prominently used: the Poisson's ratio, the tensile strength, MOE, and creep coefficient of the concrete. To consider the effects of ASR on the cracking and loss of stiffness, the formulations of the tensile strength and elastic modulus were incorporated as time dependent functions. The results of the modelling, as modified by the least square error minimisation algorithms include tensile stresses, cracking and compressive stress response of the structure.

The model proposed was used to investigate a spillway pier of a hydroelectric plant in Quebec as a 2D model with main objective to estimate the stress state in the structure from 1966 to 1989. There were two methods of analysis chosen. First, the CTMR model with nonlinear analysis accounting for cracking and effect of AAR induced compressive stress on the expansion rate. Second, a linear elastic analysis with temperature as the imposed strain. The CTMR model was found to better model cracking and tensile stresses than the linear method.

ASR modelling was found to range from complex mathematical to simpler parametric global models. The damage characterisation of ASR was also implemented in the same order of complexities for the models. The main trade off in choosing these models for use was subtly found to be following the type of results needed. Mathematical and meso models focus on the reaction itself and on the aggregate level reactions respectively. CTMR models were found to be used for real world applications in large scale structures. This study would also benefit using these types of generalised models since only the structure level results are needed, not results for interactions within the matrix.

2.5 Vibration testing

2.5.1 Introduction

This section briefly introduces the modal test methods to be used in this study. Operational modal analysis (OMA) and experimental modal analysis (EMA) are explained and compared for information pertaining to their implementation in this scoping study. A literature survey was carried out and presented in tabular format on top of the test specific considerations for this study.

2.5.2 OMA

Operational modal analysis is a vibration analysis method whereby the excitation required is obtained from the environment of the test subject. It can be performed on a structure while it is in operation as the input considered comes from environment factors such as usage, wind flow, and large equipment (Brinker & Ventura, 2015). Furthermore, the modal parameters obtained through OMA are representative of the system in its operating conditions as opposed to laboratory or altered conditions for EMA. The system is better represented by OMA because the 'white' ambient noise is assumed to excite a wider range of modes in the structure at similar excitation levels than can be done with EMA shakers in the field (Cunha & Caetano, 2006; Rainieri & Fabbrocino, 2008). Therefore, more mode shapes can be captured through OMA for structural systems using cheaper equipment setups.

OMA analysis methods are different than for EMA methods in the sense that the input is assumed to be random due to the overall characteristics of the ambient conditions of a structural system (Brinker & Ventura, 2015). Instead of the FRF, correlation and

power density functions obtained from the outputs are used for the parametric and nonparametric methods of analysis. Parametric methods fit a model to the output data and include least square complex exponential (LSCE), eigensystem realisation algorithm, autoregressive moving average (ARMA), stochastic subspace identification (SSI), and maximum likelihood frequency domain methods. These methods are more complex and compute time demanding than the nonparametric methods but show better accuracy than the latter. A stabilisation diagram consisting of plotted poles, often overlaid with a power spectrum density, which are used to find and select stable poles, representing the stable frequencies of the test data (Dewesoft, 2021; Rainieri & Fabbrocino, 2008). Parametric methods can be curve fitted to a selected order which is useful when finding a compromise between speed of analysis and data precision.

Nonparametric methods rely on the selection of the peaks occurring at different modal frequencies based on their prominence on power spectrums. These 'classical' methods fall in the frequency decomposition class of analysis and include the peak picking (basic frequency decomposition, BFD), frequency domain decomposition (FDD) and enhanced FDD (EFDD) methods (Batel, 2002; Brinker & Andersen, 2004; Ventura et al., 2001). With the addition of the complex mode indicator function CMIF), the frequency decomposition techniques, are in the frequency domain type of analysis while the other parametric methods are in the time domain (Chen & Ni, 2018). Table 2-3 shows some specific studies investigated based on OMA. OMA has been used on large scale structures as well as on laboratory sized specimens with similar success. The main observation over OMA studies is that frequency domain methods are preferred for analysis and are first performed in the case of multimethod analysis.

Table 2-3: Summary of studies in OMA

Source	Structure Investigated	Method
(Chen & Ni, 2018)	Cable-stayed bridge	Peak picking, SVD decomposition, Ibrahim Time domain, SSI-Covariance & Data driven.
(Mbarek et al., 2018)	Planetary gear system	Peak picking
(Orlowitz & Brandt, 2017)	Laboratory sized plexiglass specimen	Ibrahim time domain method
(Schrötter & Hagara, 2013)	Laboratory sized cantilever beam	Peak picking
(Magalhães & Cunha, 2011)	Arch bridge	FDD, EFDD, SSI-Covariance

2.5.3 EMA

Experimental modal analysis (EMA) is differentiated from OMA primarily with respect to the nature of the input excitation, which comes from a measured source. EMA is most often done in the laboratory on specimens which are relatively easy to induce a response into (a forced vibration), but large-scale civil engineering structures have also been successfully experimentally tested in situ. The aim of this type of test is to correlate the input forced vibrations and the output response through a frequency response function, FRF (Cunha & Caetano, 2006). EMA testing employs controlled vibration inputs with some methods being shakers, impacts, and quick release tests. Briefly put by Brinker and Ventura (2015); shaker tests use permanent magnet shakers, modal shakers or inertial shakers (Dewesoft, 2021) to excite a structure with a broad frequency range and with different excitation frequency types. Civil engineering structures are typically more complex for shaker use as the construction costs of a large enough apparatus and its associated usage and logistics can reach prohibitive levels.

Impact tests use an impact hammer to excite a structure at specific points. The force sensor in the hammer records the input while accelerometers placed at various locations record the output of the system. However, Brinker and Ventura (2015) also noted that the impact hammer is not a suitable way of modal testing for a large structure and the force required to be applied on a structure to sufficiently excite its lower frequency response would result in damage to the structure and as with shakers, would require costly equipment.

Finally, pull back tests are the temporary deformation of a structure then sudden release of the force causing the deformation to study the resulting free vibration. This method has been used on large structures successfully through the use of hydraulic rams, bulldozers or tugboats as methods of application of the deformation force (Brinker & Ventura, 2015).

Table 2-4 shows some of the studies investigated for EMA usage in literature. It was found that (industrial) shakers are more commonly used for civil engineering structures (Cunha & Caetano, 2006) over the use of impact hammers or impulse impactors. Single axis accelerometers were also prevalent, especially on the bridges (Caetano & Cunha, 2004; Sahin & Bayraktar, 2014) where the mode shapes were more easily discernible with vertical data only. EMA was not found to be widely spread in the civil engineering field as much as OMA. Applications in mechanical or aeronautical fields such as by Covioli et al. (2019) on aircrafts are more common. This is attributed to the ease of implementation. It was observed that test procedures for very large structures required large expensive equipment for excitation which severely reduces applicability of EMA, primarily due to cost, but also due to the complex logistics required.

Table 2-4: Summary of studies in EMA

Source	Structure Investigated	Method | Comment
(Sahin & Bayraktar, 2014)	Steel footbridge	Impact hammer with uniaxial accelerometers | Matlab implementation
(Schrötter & Hagara, 2013)	Laboratory sized fixed cantilever	Impact hammer EMA against OMA and FE | EMA is more sensitive to the excitation characteristics.
(Cunha & Caetano, 2006)	Bridges (real and laboratory model), Dams	Shaker | Review paper - highlight of the fact that impact hammers can result in lower excitation energies for some modes.

An important discussion aspect for EMA is the available estimators for the frequency response function (FRF). They are presented and discussed since their selection is a primary step in EMA data collection. The FRF is idealised, in a simple system with no noise or errors as the ratio between the Fourier transforms of the response over the input force. Equations (2-3) to (2-5) show the H_1, H_2, and H_v estimators (Brandt, 2011a, 2011b; He & Fu, 2001).

$$H_1(f) = \frac{G_{yx}(f)}{G_{xx}(f)} \tag{2-3}$$

$$H_2(f) = \frac{G_{yy}(f)}{G_{xy}(f)} \tag{2-4}$$

$$H_v(f) = \sqrt{H_1 H_2} \tag{2-5}$$

Where G_{xx} is the auto spectral density, G_{xy} or G_{yx} is the cross spectral density based on input to output and output to input respectively. The H_1 estimator is predominantly used in cases where the noise is in the output signals, i.e., in the measured accelerometer signals. The Hv estimator on the other hand is used in cases where the

noise is assumed to be on both the input and output (Brandt, 2011). The H_2 function is used where the noise is assumed to be in the input signal (He & Fu, 2001).

Considering that the noise in this study is not well understood, the H_v estimator is to be used as default, with the addition of another estimator if needed. A test evaluating all three estimators needs to be performed to select a second estimator.

2.6 Modal Model Updating

This section shall explore two areas of the model updating process: the updating steps and the modal parameters. Modal model updating is a thorough field in mechanical and civil engineering with a significant difference being the modal data used. The overall FEMU steps are laid out as being the creation of an FE model, obtaining the comparison data from vibration test methods, and the comparison of FE and experimental data based on frequency response functions, eigen to natural frequency comparison, mode shapes, modal assurance criterion (MAC) values amongst others. The model is then updated through direct or iterative methods, from which the latter is most commonly applied (Sehgal & Kumar, 2016).

Table 2-5 shows a summary of the main pieces of literature investigated for this section. The literature survey revealed some pertinent application notes concerning the model updating procedure. While not codified, the FEMU procedure is relatively simple but implemented in various ways, especially at the FE to experimental data correlation and at the updating steps, which will be addressed in this section.

The data correlation step involves matching the experimental data with that of the FE engine in order to reach exact or near exact values. The studies investigated focused

primarily on the matching both sets of mode shapes through the MAC values. The frequency sets were also matched secondarily through the use of percentage difference. An outlier in this category is the use of the energy-based MAC value by D. Ribeiro et al. (2012) for a railway bridge. It has the advantage of being more precise in mode shape matching but requires significant additional computation and custom coding for implementation.

Specific values for correlation have not been used consistently across the literature but sporadically, above 85% for MAC values (Steve McDonald, 2016), 1% for frequencies (Poprawa et al., 2017), and an optimiser stopping criterion in the order of 10^{-4} (Girardi et al., 2020) have been found.

For the optimisation step, the use of iterative optimisation methods dominated the literature surveyed. No direct method was found to be used in either laboratory or in situ tests. Of the literature surveyed, few had specifics laid out on the nature of the algorithm used with customised least squares error function formulation (Dimri & Chakraborty, 2024) and purpose-coded truss region algorithm in Matlab (Girardi et al., 2020).

Table 2-5: Summary of studies on FEMU

Source	Structure	Vibration Test Type	Match Parameters
(Dimri & Chakraborty, 2024)	Concrete slabs	EMA	MAC value, frequencies
(Girardi et al., 2020)	Large scale: arch, dome, clock tower	OMA	Frequencies
(Covioli & Coppotelli, 2019)	Aircraft	OMA & EMA	MAC value
(Poprawa et al., 2017)	Railway bridge	OMA	MAC value, frequencies, displacements, damping
(Steve McDonald, 2016)	Vehicular bridge	OMA	MAC value, frequencies
(Ribeiro et al., 2012)	Railway bridge	OMA	MAC and EMAC values
(Guggenberger, 2009)	Laboratory sizes motor	OMA, EMA, ODS	Frequencies, MAC values (displacement assurance crit. For ODS), local mode shape amplitudes, FRF

2.7 Literature Review – Summary and Conclusion

2.7.1 Summary

The literature review can be summarised based on the three aspects of this study: ASR, vibration testing in the form of EMA and OMA, and the model updating process.

The first part of the literature review details the problem to be investigated, ASR. It was found that the MOE and tensile strength of concrete are the most sensitive indicators of ASR, from a damage standpoint. It might seem contradictory to not use compressive strength since compressive strength is one of the primary concrete performance metrics, but it was found that compressive strength is largely unaffected while concrete is under the stress due to crack closure.

OMA and EMA have been studied extensively and many models for each are available. The modal parameters from the testing can be implemented towards model updating in terms of measured test frequencies, referred to as NF for natural frequencies in this document, being mapped to the frequencies obtained by the FE model, referred to as EF, eigen frequencies. Mode shapes were found to be widely used as well for testing FE model correlation.

However, specifics of testing and data analysis were found to be largely influenced by the analyst's experience and judgement (Avitabile, 2014; Poprawa et al., 2017) since no standardised test procedure was found for vibration testing nor model updating.

2.7.2 Conclusion

The goal of this study is to bridge the gap between ASR diagnostic and/or monitoring using a combined vibration and modal model updating framework while exploring the effectiveness of either EMA or OMA as vibration test methods. ASR, vibration testing, and FEMU are mature fields in their own rights, with intersection with any two of them. For example, ASR and vibration testing as presented in Section 2.2.2, and vibration testing and FEMU as presented in Section 2.6. This study explores the combination of all of them. As for expectations management, it is important to point out that for the entire process of working:

- One or both of OMA and EMA need to be able to reliably measure the differences in ASR reactive or unreactive concrete and produce actionable results for the FE model updating. This would determine if ASR can be 'measured' by modal test. Failure to do so would indicate that only ASR changes can be monitored and a baseline is needed, similar to expansion measurements.
- The FE model correlation being able to update correctly based on reliable test data. The entire path, from model creation, optimisation and result validation, needs to be found using the available software. In essence, the entire process needs to be devised.

3 Experimental Studies

3.1 Introduction

This chapter introduces the specimens used in this study and the experimental regime performed. The design of the experiment is laid out to the level relevant to the OMA or EMA nature of the test whereby in-depth experimental details pertaining to the instrumentation of the blocks have been placed in Appendix A for conciseness. The resulting test data is analysed in Chapter 4.

3.2 Specimens

The specimens used in this study come from a previously started ASR study being carried out at the University of New Brunswick exposure site. These specimens are concrete blocks of varying mix designs, of sizes 0.38 by 0.38 by 0.71 m, and weighing approximately 200 kg. They have been exposed to atmospheric conditions since they were cast, about 19 ± 1 years as of 2022 when vibration tests were performed. The specimens having the least amount of ASR mitigation measures such as admixtures or supplementary cementitious materials were selected from the set and brought to the UNB structural laboratory for testing. Specific details about the specimens are given in Table 3-1. The chosen specimens were cast with a water to cementitious materials ratio of 0.45 and have no supplementary cementitious materials (SCMs) added. These were selected to isolate the effects of alkali expansion only, without interference from the protective effects of added SCMs although the use of different cements and aggregates may change the concrete behaviour.

Table 3-1: UNB exposure site block details

Name	Aggregate	Cement	Alkali Content (%)	Initial Reading Date
A	Mactaquac Greywacke	Brookfield	0.91	September 2005
F	Springhill #3 quarry	Brookfield	0.91	December 2005
R	Springhill #3 quarry	Brookfield	1.25	July 2006
AA	Springhill #3 quarry	Mix	0.75	August 2006
AB	Springhill #3 quarry	Mix	0.50	August 2006
AC	Springhill #3 quarry	Mix	0.62	September 2006
AN	Springhill #3 quarry	Dragon	1.25	July 2007
AS	Springhill #3 quarry	St. Mary's	0.50	November 2007

The specimens were kept at the UNB exposure site at the Fredericton campus in NB since they were cast, outside and exposed to the elements as shown in Figure 3-1. Expansion measurements were taken on these blocks using a 500mm demountable mechanical (DEMEC) strain gauge from Mayes instruments with the locating pins embedded in the blocks at the casting time.

There are 4 reference sets of points, 2 on either side and 2 on the top face of the blocks, all of which are averaged to find the block expansion. The measurements are on the 500 mm gauge but were normalised to 100 mm expansions on the measurement data spreadsheet. The same format has been kept and any further expansions given are 100 mm representative normalisations.



Figure 3-1: UNB exposure site

Figure 3-2 shows the expansion data along with temporal reference points for the specimens. The expansion data was measured as soon as 1 year from their cast date. Other data such as compressive strengths, moduli of elasticity, or tensile strengths have not been constantly recorded for these specimens since ASR monitoring through expansion was the focus of the experiment the specimens were taken from.

The specimens were cast as per ASTM C1293 Standard test method for the determination of length change of concrete due to Alkali silica reaction (ASTM, 2018), similar to the Canadian standard CSA A23.2-27 (CSA Group, 2019).

As a measure of expansion and by proxy, their reactivity, expansion limits from CSA A23.2-27A Table 2 (CSA Group, 2019) have been added. The segment delineated by the lines indicates the limits for a specimen to be qualified as reactive, moderately reactive, highly reactive, and extremely reactive. Given that the ASR expansion limits are to be applied on laboratory sized prisms after a 1-year duration, these limits cannot be directly taken at face value in the figure presented. Accounting for size differences, if the

1-year limit is instead taken as the lifespan of the specimens, they can be classified as extremely reactive (A, AN, F, and R) and non-reactive (AA, AB, AS, and AC).

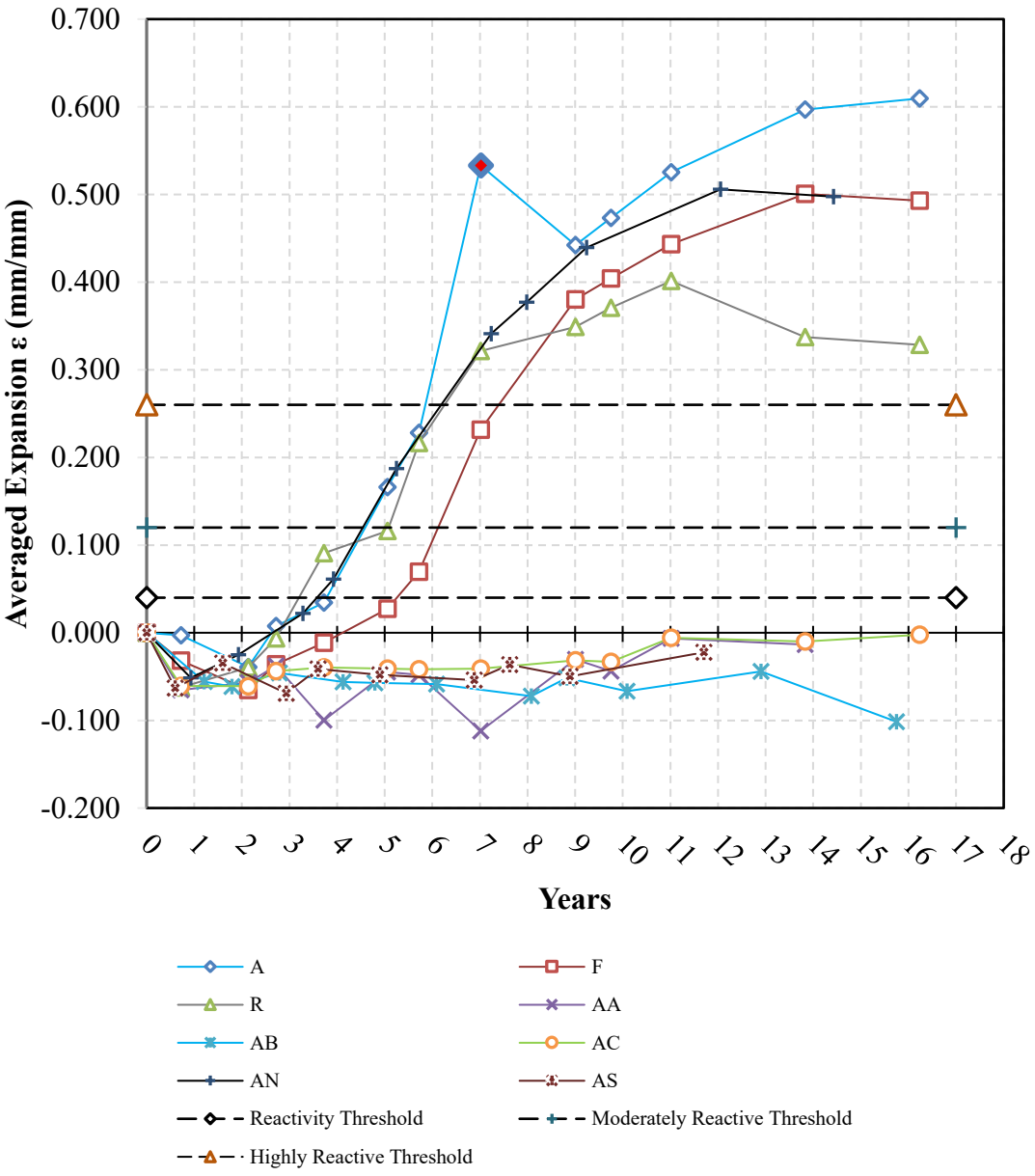


Figure 3-2: ASR expansion data for selected blocks

The reactive blocks seem to have gone through the ASR expansion S curve completely and are stabilising with the exception of block A which appears to have slightly more expansion to undergo. The highlighted point for block A at year 7 is indicative of a crack that appeared and misaligned one of the locating pins. Subsequent measurements omitted that specific pair of misaligned pins. Block R also seems to be experiencing effects other than ASR expansion since the expansion contracted more than the other three blocks. Drying shrinkage might be the culprit but given the haphazard plot points for the block, there might be some faulty DEMEC points at play. For the nonreactive blocks, block AB seem to be experiencing the same contraction as block R.

3.3 Experiment Design

The absolute consideration in the design of the experiments is that the specimens cannot be harmed in any way that would interfere with the natural ASR progression occurring. The specimens, especially the reactive ones, cannot be machined, drilled, or altered in a way that would affect the spacing distribution of moisture and heat across the volume of the specimens. They also cannot be handled in a way that would cause sudden shocks or possibilities of sudden shocks.

3.3.1 Orientation and layout

The blocks, as specified in the introductory subsections, are large and heavy, making their handling and support matters of their own discussion. The purpose of vibration testing is to have the specimens interact with its environment for ambient vibration while being excited by the user with forced vibration.

For the specimen supports, there are a number of possible configurations possible based on the boundary conditions one would require. Common boundary conditions for modal testing are from a combination of the free, fixed, and pinned conditions.

3.3.1.1 Free-free condition

This condition entails that the specimen be suspended in the air while experimentation. This setup provides the least amount of interference on the specimens as they are isolated from the effects of the surroundings. This makes it particularly suitable for EMA whereby the hammer is more isolated from the effects of the surroundings.

However, this set up requires the specimen to be suspended which has the following concerns arise:

- Being suspended makes the specimen prone to sudden shocks or breakage in the event that the suspension mechanism fails.
- Working under or around a large, suspended block, especially in the case of EMA is unsafe due to the block oscillating and collision risks.
- Investigating suspension mechanisms would entail finding the right stiffness of rubber cordage to suspend the block while isolating it and this part of the experiment design would be financially and time consuming.

3.3.1.2 Fixed Condition

Any condition involving the fixed condition would entail having to fix the specimen at the boundary condition. If the z-direction is the direction of gravity and is naturally restraint, restraining any of the other 2 directions would entail having to fasten the specimen with some sort of mechanical device which would damage it. A

workaround to this problem could be to clamp the specimen. However, finding the right clamping force with respect to adequate restraint might prove to be damaging if done incorrectly, and costly to manufacturing such a contraption.

3.3.1.3 Pinned Condition

The samples were first supported on a simple setup used to approximate pinned-pinned conditions. The specimens, shown in Figure 3-3 were placed onto a double steel rod simple support rig. The support rig was made of welded Ø12.5mm spaced at 600 mm, kept apart by similar rods welded on top. The block would fit between the top rods, ensuring that there would not be space between the rods and the ground. The setup was implemented on the heavy flooring in the structural laboratory to ensure limited external noise in the system.



(a) (b)

Figure 3-3: Simple Support setup (a), Install process (b)

The blocks were lowered onto wooden blocks first such that the support could be properly aligned Figure 3-3 b). Then each side of the block would be gently nudged upwards to remove the wooden blocks and rest it on the steel rod. The wooden blocks

acted as a buffer to prevent any sudden shocks on the block and to give clearance to remove the positioning straps. The former were important to ensure cracks would not enlarge during installation.

The specimen was then instrumented and tested using two different accelerometer configurations as seen in Figure 3-4. Part (a) shows the configuration used for EMA while part (b) shows the configuration for OMA. For EMA, the block was excited with the hammer on the top surface and on the sides to try to maximise mode capture.



(a) (b)

Figure 3-4: Accelerometer configurations for simple support, (a) In line 3. (b) Evenly spaced 11.

The results obtained were not conclusive; there were no defined mode shapes or frequencies obtained. Upon investigation, it was discovered that the undersides of the blocks were not completely flat (possibly due to swelling and/or bad casting), and this was introducing unwanted vibrations (wobbling) in the system.

3.3.1.4 Final Pinned-Free condition

The final option considered was to stand up the block on one of their end faces. This would prevent any surface irregularities that were introducing noise. Three setups were tested: one with the blocks being stood up on some felt sheets (consisting of woven plastic fibre sheets of 5 mm thickness with the consistency of firm synthetic wool); second with the blocks being laid on 3 accelerometer mounting pads (stainless steel discs of Ø35 mm and thickness 10 mm), and the third with the blocks being stood directly on the heavy concrete flooring. These setups are shown in Figure 3-5 and Figure 3-6. The first two methods proved to be unstable, with the felt sheets being the most unstable for tip over. The second option was rejected as the blocks did not have a flat surface and the wobbling problem in the previous pinned configuration arose again. The experiment proceeded with the blocks being rested directly on the heavy floor for both OMA and EMA.



(a)



(b)

Figure 3-5: View of stand-up block setup with (a) showing direct ground contact and (b) showing insulation between the ground and the block.



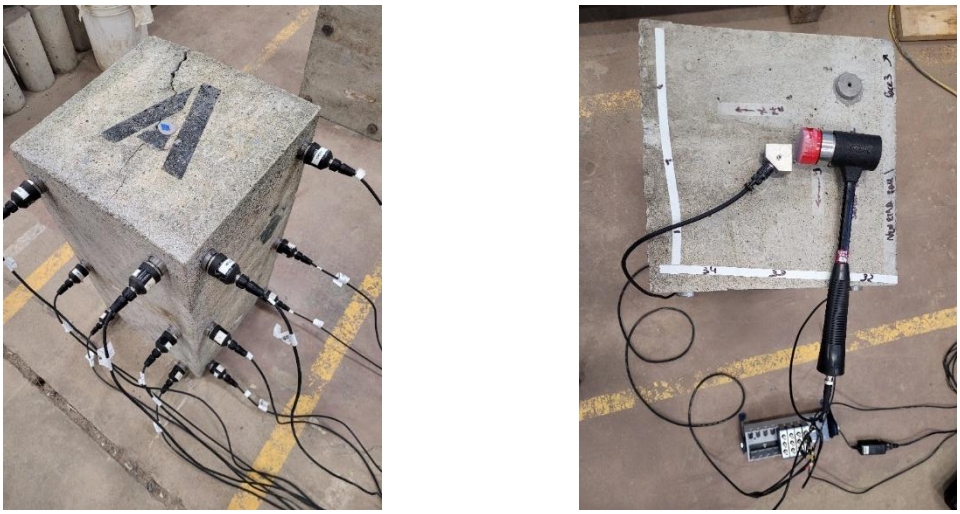
Figure 3-6: View of the underside of the block showing the three steel supports being set.

To be able to compare the results obtained from both test methods, the overall layout of instrumentation and data collection was kept similar. Inputs, in terms of OMA were defined as the accelerometer readings while for EMA, they were the hammer hit points on the specimen as opposed to the accelerometer readings. Therefore, the OMA

accelerometer locations had to match the EMA impact points. Given the limited number of accelerometers available and the need for more accurate mode shapes, the instrumentation plan was as follows:

- OMA: Linear accelerometers were installed on 2 side (long) faces of the blocks.
- EMA: A single tri-axial accelerometer was mounted on the free, top side face of the blocks at the locations where linear accelerometers for OMA were taken as impact points for the hammer. Tentatively, an impact point was also taken to the side of the triaxial accelerometer, at 50 mm from the centre and in the z-axis. It was found that this point introduces more error in the data and was therefore quickly discarded in the analysis.

The constraint is focused on the mode readability of the obtained results. For a face, 4 corners are needed to read twisting modes and a midline to read a bending mode. That would necessitate 6 sensors per face at a minimum, and since there are 12 linear accelerometers, 2 faces are instrumented in equal spaces to be able to get a 3D representation of a mode shape. A typical setup for each type of test is presented in Figure 3-7. Figure 3-7 a) shows the OMA instrumentation layout while b) shows the instrumentation for EMA. To keep measurement locations similar for comparative testing, the accelerometer locations for OMA are taken as hammer impact locations for EMA.



(a) (b)

Figure 3-7: Typical test setup for OMA (a) and EMA (b).

3.3.2 Experimental Regime

3.3.2.1 Sampling

The sampling frequencies used in the measurement of OMA and EMA data were different as there was a change in DAQ for the OMA data collection. For OMA, block R was sampled at 16 kHz, blocks F, AC and AB were sampled at 12.8 kHz (with the Spider 80 system) with the rest of the blocks sampled at 10.24 kHz for OMA on the cDAQ. EMA was also performed at 10.4kHz for all blocks on the cDAQ. The sampling frequency of 10.24 kHz was the maximum achievable frequency on the NI DAQ, and if it is taken as the standard sampling frequency for all blocks, the least Nyquist frequency for the whole set is therefore 5.12 kHz. Given that in Chapter 5, a finite element analysis was performed yielding a maximum 10^{th} modal frequency of 3223 Hz (30 GPa reference model), a clearance of ~2 kHz was judged to be more than adequate to bypass any artefacts that can arise during processing.

3.3.2.2 Input Excitation

For the OMA tests, two variants were explored. The first being ambient vibration from the heavy flooring in the laboratory and the second being manual excitation from the user rebounding a basketball in close proximity to, and around the specimen. These were measured for 10 minutes each. Other considerations for the excitation of the specimen for OMA included being repeatedly hit with a selection of hand tools such as handles out of wood, metal and rubber, but were phased out because of no observable results and difficulty in maintaining a rhythm of one tap for every decay of the specimen. The excitation with hand tools were also not feasible for extended amounts of time due to the awkward position of the impact locations.

The basketball side impact decay was directly observed from the data acquisition window, and the basketball rebounds were timed accordingly, at around 2s interval.

For the EMA tests, the following additional considerations are given in addition to the sampling frequency.

1. The hammer tip stiffness and impact force

The available types of impact hammer heads are Hard, Medium, Soft, and Super Soft, shown in Figure 3-8 along with the impact hammer. For reference, the hard tip has the consistency of a ball pein hammer hitting a steel beam while the super soft tip has the consistency of a dead blow hammer.



Figure 3-8: Impact hammer and accompanying tips

The instruction manual (PCB Piezotronics, 2025) for the impact hammer, a 086D20 short sledge impulse hammer from PCB Piezotronics was reviewed. The most important specification for the hammer is in the form of the frequency response curve for each hammer tip the instrument is supplied with. The frequency response curves are provided in the instruction manual and reproduced in Appendix A-4. One important detail is that these curves are given for impacts on a stiff steel mass. It is seen that the frequency response is within the 600 to 1100 Hz range for all of the tips. For the specimens tested, it is of little importance since:

2. The range investigated is from 0 to 4000 Hz and optimum tip performance is more of a compromise than a hard limit for this range.
3. The reference curves are given for steel. The specimens tested are concrete. The frequency response is expected to vary largely from the reference curves.



Figure 3-9: EMA trial operation

Choosing the appropriate hammer and impact force depends on the level of energy required by the specimen to be excited and show a clear FRF. To find the appropriate tip, a pre-test experiment was carried out to investigate the excitation response with respect to the specimens. This pre-test consisted of investigating the output response with respect to the hammer tips, and with respect to the impact force, the later of which were taken as 400 and 5000 N as reference. The description and results of this test are laid out in Appendix A-4. The medium tip, in red in Figure 3-8, was chosen and used for this study. The trigger level was set to 1200 N but the impact force averaged to 4000 N based on instant power spectrum densities. Though not generalised for every block, top nodes were generally more prone for block shifting at forces above 2000 N. the average force of impact for top nodes was 1500 N. Bottom and middle nodes were more forgiving and were impacted with an average force of 4000 N. The nodes were impacted

and the shape of the impact response, and the accompanying response curve was verified to be correct before the next impacts. A total of eight impacts per node, with varying impact forces were captured for every specimen. This number of impacts was found to be a compromise between the maximum number of impacts that could be carried out to maintain reasonable test time. The following section gives more specifics about the manner in which the data was collected.

3.3.2.3 Data Collection

The specimens were tested under operational and experimental with test setups tabulated in Table 3-2.

Table 3-2: Test methods used

OMA	EMA
Ambient Vibration	H_1
Forced Ambient Vibration	H_v

For the experimental modal tests, all three available estimators in ARTeMIS were tested on block A to investigate their performance. H_2 was found to not be as effective as H_1 and therefore omitted in subsequent tests. Due to the nature of how ARTeMIS modal collects EMA data, changing the estimator in post processing was not possible. EMA tests were therefore performed in duplicates with the only changes as the estimator used, $H_{v \text{ and }} H_1$.

For the operational modal tests, the choice of having a source of excitation by the user (basketball) was made because the ambient vibration of the test environment (the heavy concrete floor of the laboratory) did not provide a broad enough excitation. Figure

3-10 shows the singular value decomposition (SVD) plot of a typical OMA test (block A) with harmonic peaks indicators placed at every multiple of 60 Hz (power / voltage frequency). Figure 3-11 on the other hand shows the same block with the harmonic peaks added, but with an external source of ambient vibration. External being defined here as outside of the specimen / or excitation not directly providing energy to the specimen through contact. A basketball was used through dribbling around the specimen to transmit energy to the specimen through the concrete floor it rested on. Direct excitation was investigated, drawing from EMA, by means of various impacting tools to directly provide energy to the specimen. The tools used were a Ø18mm steel bar, a 50x42mm LVL bar, and a small Ø45mm rubber mallet. The specimens used emulated a range of tip stiffnesses as addressed in EMA testing. While the tools helped with exciting the specimen, they hindered the experiment more than they helped since:

- Impacts could only be performed on the 2 sides of the specimen where the accelerometers were not installed as any hits to the accelerometer or to their wires would introduce noise. This shifted the response since the specimen could not be excited uniformly.
- The reliability of this setup was poor since it was not ergonomic to impact the specimen across both faces with impacts distributed as uniformly as possible over the area over 10 minutes of test data collection.

The basketball proved to be much better in addressing the two points raised since the excitation came from all around the specimen through the floor with timely impacts of around 2s, and consistency of the impacts were preserved due to the better position of

standing throughout the experiment and not having to be hunched over next to the specimen while timing impacts over both faces. The resulting spectrum with the forced ambient vibration has more discernible and less noisy peaks.

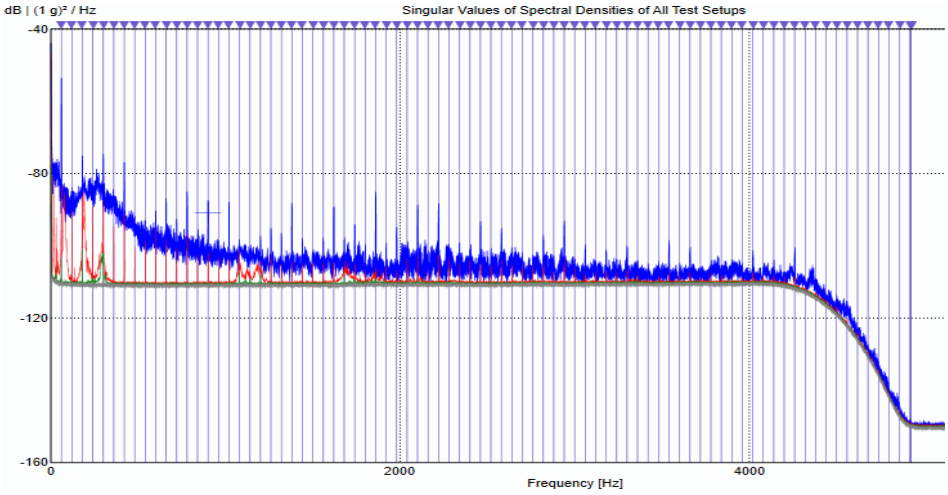


Figure 3-10: SVD plot of OMA setup with Ambient excitation only

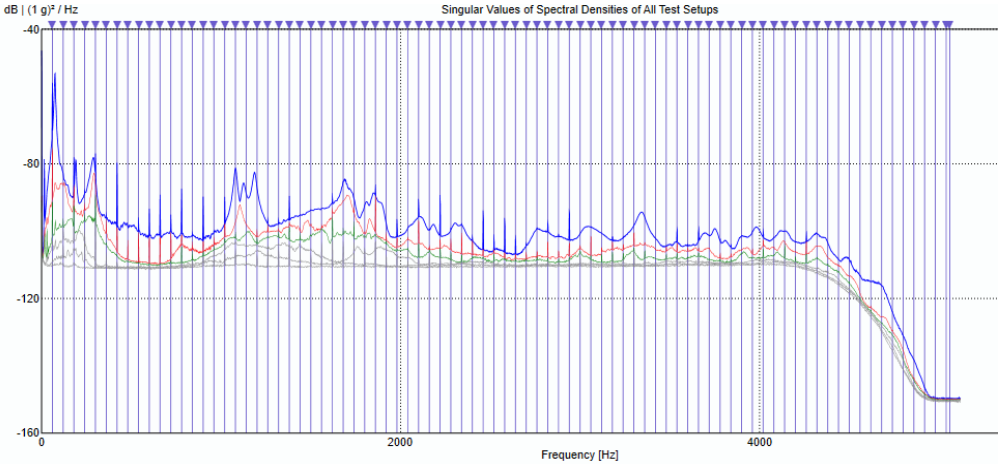


Figure 3-11: SVD plot of OMA setup with Forced Ambient excitation

3.4 Summary and Conclusions

3.4.1 Summary

This chapter detailed the specimens and the experimental regime used in this study. Eight concrete blocks (A, F, R, AA, AB, AC, AN, and AS) were selected from a longer-running ASR study with mix designs without any SCMs and with a similar w/cm. This selection was made to isolate the effects of alkali expansion, although variations in cement type and aggregate source remain across the set. Approximately 19 years of expansion measurements were available for each specimen. Adapting the CSA A23.2-27A laboratory expansion limits to the specimen lifespan rather than to the standard one-year duration classifies blocks A, AN, F, and R as extremely reactive, and blocks AA, AB, AS, and AC as non-reactive.

The experimental design was constrained by the requirement that the specimens not be machined, drilled, or subjected to sudden shocks that could interfere with the ongoing ASR progression. Several boundary conditions were considered. The free-free condition was rejected on safety grounds and because of the cost and time required to develop a suitable suspension mechanism. Fixed conditions were rejected because any mechanical fastening or clamping carried a risk of damaging the specimens. A pinned-pinned configuration on welded steel rod supports was implemented first but produced no defined mode shapes due to wobbling caused by uneven block undersides. The setup was therefore reconfigured to a pinned-free condition with the blocks stood upright on one end face. Felt sheets and accelerometer mounting pads were trialled as interface materials

but proved unstable. The final configuration places the blocks directly on the heavy concrete laboratory floor.

To preserve comparability between OMA and EMA, the instrumentation layout was harmonised across both tests. Twelve linear accelerometers were distributed evenly across the two long side faces of the block for OMA, and a single tri-axial accelerometer was mounted on the top face for EMA, with hammer impact points matching the OMA accelerometer locations. The baseline sampling frequency of 10.24 kHz on the cDAQ gives a Nyquist frequency of 5.12 kHz, which provides ample clearance above the 3223 Hz tenth modal frequency predicted by the finite element analysis presented in Chapter 5. For OMA, both ambient vibration from the heavy floor and forced ambient vibration generated by dribbling a basketball around the specimen were collected over 10-minute windows; the forced ambient case produced cleaner, more discernible SVD peaks than ambient vibration alone, and direct excitation with hand tools was rejected for ergonomic and uniformity reasons. For EMA, a pre-test on hammer tip selection led to the medium tip being adopted, with a trigger level of 1200 N and eight impacts per node were recorded. Both the H1 and Hv estimators were retained for the analysis, with the H2 estimator found to be less effective and omitted.

3.4.2 Conclusions

The work documented in this chapter establishes a non-destructive vibration testing protocol that satisfies the principal experimental constraint of preserving the specimens for continued ASR progression. The final pinned-free configuration, arrived at through iteration on both boundary conditions and interface materials, resolves the

tension between data quality and specimen preservation by eliminating the wobble that contaminated the pinned-pinned setup while requiring no mechanical fastening to the blocks. The lack of proper instrumentation techniques and recommendations was felt in this stage and efforts shown in Appendices A-3 and A-4 aim at covering those gaps for this study.

The deliberate matching of OMA accelerometer locations to EMA hammer impact points preserves direct comparability between the two test types at the node level, which is a prerequisite for the comparative analysis carried out in Chapter 4. The paired dataset generate: 10-minute ambient and forced ambient OMA records, and eight-impact-per-node EMA records with both H1 and Hv estimators, for each of the eight specimens, provides the experimental input to the modal analysis of Chapter 4 and to the finite element model updating exercise discussed later in the thesis.

4 Modal Analysis

This chapter details the work performed primarily on the ARTeMIS platform in the analysis of the data set generated through OMA and EMA tests. Mode shapes were very heavily relied on in the analysis, especially on the validation step and expected shapes obtained from FE analysis in Chapter 5 proved to be significant in terms of clarity.

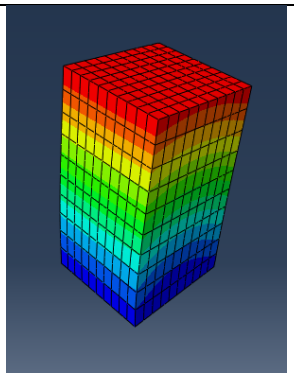
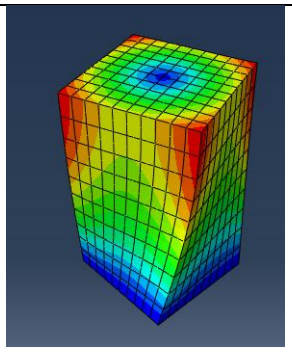
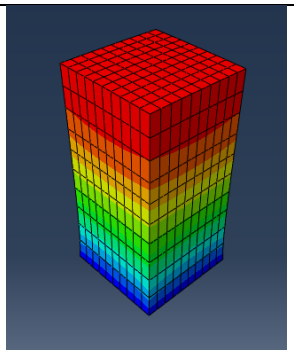
4.1 Expected Data Description from FE Model

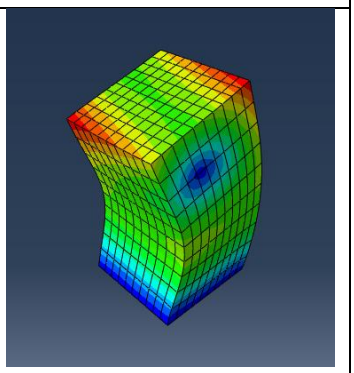
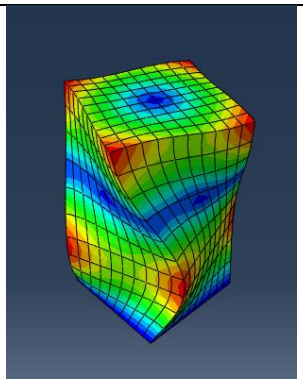
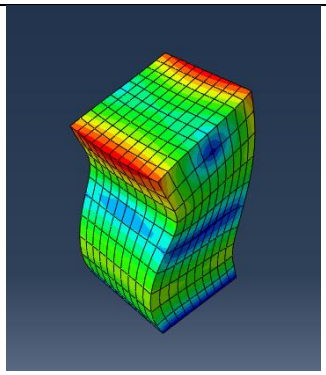
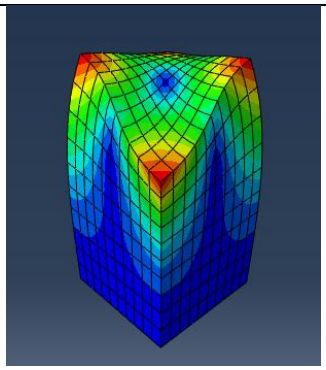
The test data analysis was performed while guided by FE analysis results through the use of the eigen frequencies to locate the regions of natural frequencies and the mode shapes for cross validation.

Section 4.1 describes the results used to guide the test data analysis. The FE study is described in detail in Chapter 5. The model uses concrete with an MOE of 30 GPa, density of 2350 kg/m^3, and Poisson's ratio 0.2 in a linear-perturbation step in Abaqus, with a pinned bottom face.

Table 4-1 shows the end results of the FE analysis and demonstrates the mode number with their associated frequencies and mode shapes for modes 1 through 10. The first mode starts at 370 Hz and has a mirrored (degenerate) pair which is orthogonal to it. This phenomenon is repeated in modes 5 & 6 and 8 & 9 at 1375 and 2857 Hz respectively. As preliminary guidance, the data analysis is performed using the following guide bands to verify the modes (within ± 100 Hz) 300, 700, 1200, 1400, 2800, and 3200 Hz. The mode shapes are heavily referenced during the validation step.

Table 4-1: FE analysis results: mode shapes and modal frequencies of a typical block.

Mode #	Frequency (Hz)	Comment	Shape
1 & 2	370	Cantilever	
3	750	Twisting	
4	1262	Axial Elongation	

Mode #	Frequency (Hz)	Comment	Shape
5 & 6	1375	Bending	
7	2247	Twisting	
8 and 9	2857	Double Bending	
10	3223	Free Face Axial Distortion (Warping)	

4.2 Analysis Regime

This section demonstrates the work performed in order to compile and validate the modal data from the test data. The operations performed in ARTeMIS, and Matlab are laid out in order of operations.

The available analysis methods (estimators) on the Artemis platform are shown in Table 4-2. Data pre-processing was possible only for OMA after collection since for EMA, after the selection of impact characteristics, no further processing is required for the frequency response functions. The pre-processing done for OMA was only in terms of adjusting the frequency bins such that a fine enough resolution of sub-1 Hz frequency is obtained for the proper manual selection of modes in the subsequent analysis methods, and the addition of peak indicators on 60Hz harmonics. The available tools for adjusting the frequency bin were mostly limited to the windowing size and overlap.

Table 4-2: Analysis methods available in ARTeMIS

OMA		**EMA**	
Frequency Domain	Time Domain	Frequency Domain	Time Domain
FDD	SSI-PC	CMIF	RFPz
EFDD	SSI-UPC		
CFDD	SSI-UPCx		

The analysis steps are explained in the following section using block A as example. The general data analysis performed on ARTeMIS was developed after a trial-and-error basis. The main steps of analysis for OMA and EMA are the pre-processing steps for OMA, peak picking (OMA and EMA), and mode shape validation (OMA and EMA).

4.2.1 Pre-Processing

Pre-processing is an OMA only step and is only used for this study to ensure that peaks are user pickable through a fine enough resolution below 1 Hz per frequency line. The full recording at Nyquist frequencies 5120 / 6400 / 8000 Hz are processed with 66 percent default window overlap and 4096 / 8192 / 8192 bins, giving the approximately 0.625 to 1.25 hertz line spacing. The Hanning window is fixed in ARTeMIS and cannot be changed; alternative windows might have helped with noise rejection but were not available within the platform. Channel data information such as kurtosis or skew are not presented as they were not used in this study. Harmonic peak detection lines are overlaid on the plot at 60 Hz, from 0 to 4000 Hz to help with noise peak identification. They are shown on the block A pre-processing step SVD lines, as the vertical blue lines in Figure 4-1.

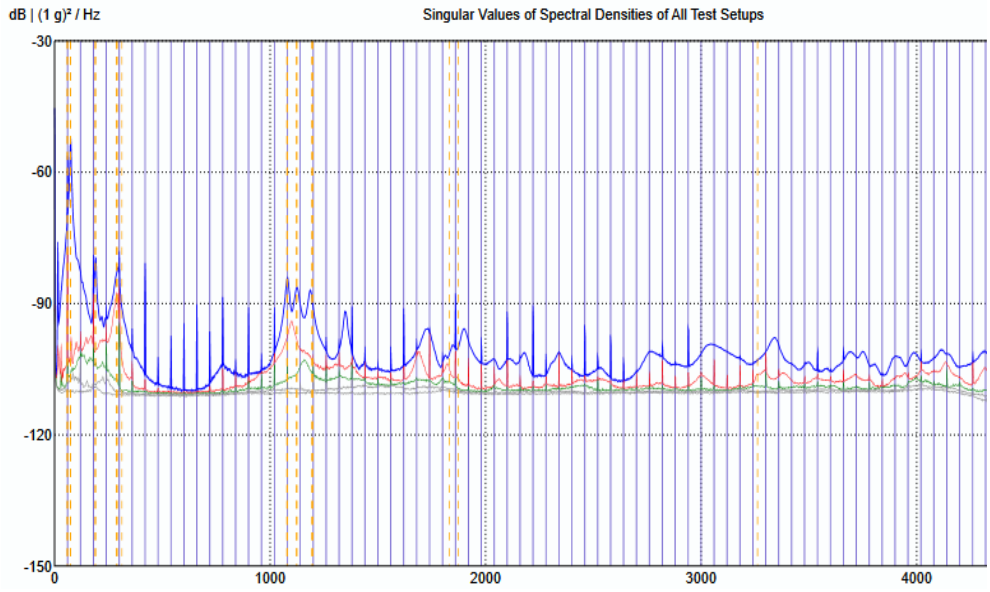


Figure 4-1: Pre-processing step SVD line for block A with harmonic peak detection overlaid

In addition to the harmonic line overlay to help mitigate the selection of electrical noise peaks a few observations were made with respect to noise modes. They are listed shortly and were taken into account in user mode selection and partially in the Matlab cross validation step. The noise peaks were found to be short and slender compared to actual modal peaks on the SVD plots with smaller gap between SVD line 1 and the others. It was found that in contrast to noise peaks, mode peaks were broader and spread out over a range >> 5 Hz and have a rounder cap on top of being well separated from the noise floor.

Figure 4-2 shows a section of block A SVD plot from Figure 4-1, to illustrate the difference between what were found to be noise and actual peaks. Labelled in a black zone are example of noise peaks, while in the red zone are three prominent actual peaks. The separation from the noise floor of actual peaks is shown by the two red arrows, which are compared against the noise peaks stemming directly from the noise floor.

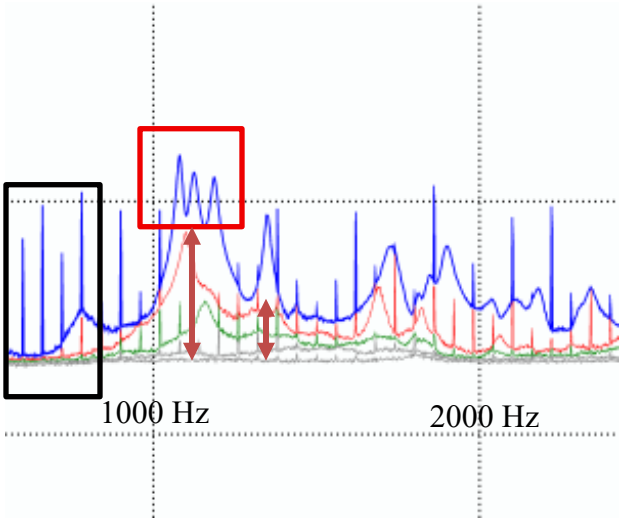


Figure 4-2: Zoom in section of block A SVD plot showing frequency range between 1 and 2 kHz.

4.2.2 Mode Selection

After the data has been pre-processed for OMA, and directly from the recordings for EMA, the variety of estimators could be used in ARTeMIS. The automatic mode detection feature was used to simplify the peak picking process as ARTeMIS provides powerful frequency and time domain automatic mode estimations which are complemented with user picks and deletions.

The parameters used in the automatic mode estimation are as follows:

- The dynamic headroom: a measure of the prominence of peaks with respect to other peaks in the spectrum. A value in dB is specified for which any peaks below the specified threshold from the highest peak in the spectrum is excluded. The default value of ~32 dB was used.
- The maximum damping allowed: It was found to not be very useful since noise modes were usually zero damping modes.
- The MAC rejection Level: It is the correlation of the mode estimate (bell curve reconstruction) in EFDD and CFDD with respect to the peak being investigated. Default value of 0.8 recommended by user manual such that estimation does not force fit noise along the tails of the curve and is accurate at the peak.
- Modal correlation lags: It is the number of frequencies neighbouring the peak being investigated that the software uses to determine the modal coherence. The latter is the average of the dot product of the 1st singular vector at the peak and the neighbouring specified number of frequencies. This coherence is greatest where peaks are

dominating and low where modes are mixed. (It is shown in muted blue background on the SVD plots.)

On the SSI estimators, automatic mode selection is already performed by default during the pre-processing stage. During estimation, only convergence criteria for model orders can be adjusted. These are the deviations in frequency, damping, and mode shape MAC. The frequency and damping deviations have been found to be the most influential in these estimators.

The parameters used for frequency domain automatic mode estimation were found through a series of parametric studies on each parameter when compared to user selection against ARTeMIS automatic selection. They were used consistently across estimators and are as follows:

- Dynamic Headroom: 100 dB
- Max Modes: 30. Only the first 10 modes are needed (for FE updating), however, a greater number is specified to coax the algorithm to continue finding modes should the 10 modes be noisy.
- MAC Rejection: 0.8. Default value used as specified in user manual.
- Modal lags: 30 has been found to generate the most modes with respect to observable peaks.

The parameters used for time domain estimators were:

- Frequency deviation: 0.1
- Damping % deviation: 0.1
- Mode Shape deviation: 0.1

The frequency deviation had the most significance on the stability diagrams. However, changing the maximum deviations on the time domain estimators did not introduce nor remove any mode shapes. Therefore, the deviations were for model order stabilisation only. The automatic results for frequency and time domain estimators for block A are provided in Table 4-3 and Table 4-4 respectively.

For the frequency domain estimators, EFDD and CFDD performed similarly in terms of number of modes found and their respective complexities. The FDD estimator found two more modes than the others. These modes, as compared in the PSD plots, seem to come from well defined, broad peaks on SVD line 1 and are separated from the next SVD line as much as their neighbouring modes. Furthermore, there are peaks in the spectrum which were not selected by any estimators but also have well define peaks such as those around the 1800 Hz region.

For the time domain estimators, the quantity vs quality of modes seemed to be inversely correlated in the order of UPC, PC and UPCx. The quality of UPC seemed questionable since the selection of peaks as seen in its PSD, was observed to be either repetitive (multiple selection around peaks in regions of 75 and 288 Hz) or shifted (stabilisation lines not centred on peaks around 288 and 1200 Hz). PC was observed to select modes better than UPC based on the modes being centred on peaks. However, some repetitive selections were observed around 70 and 288 Hz and an uncertain mode appearing around 1800 Hz. UPCx's selection of modes was the most concise as it either identified many of the lower modes as noise or it did not select any. It also had a slight frequency shift in selection but not as pronounced as the others.

Table 4-3: Automatic estimator results: Frequency Domain

FDD		EFDD			CFDD		
Frequency (Hz)	Complexity (%)	Frequency (Hz)	Damping (%)	Complexity (%)	Frequency (Hz)	Damping (%)	Complexity (%)
74	0.03	74	2.71	0.04	74	2.03	0.04
191	0.15	190	2.08	0.19	190	1.32	0.19
1083	0.37	1081	0.78	0.23	1080	0.46	0.23
1124	2.19	1125	0.91	2.25	1125	0.53	2.25
1187	8.71	1186	0.69	14.4	1186	0.40	14.4
1357	2.32						
3044	43.7	3048	0.95	45.9	3049	0.63	45.9
3339	10.6						

Table 4-4: Automatic estimator results: Time Domain

SSI - UPC			SSI-PC			SSI-UPCx		
Frequency (Hz)	Damping (%)	Complexity (%)	Frequency (Hz)	Damping (%)	Complexity (%)	Frequency (Hz)	Damping (%)	Complexity (%)
55	13.45	13.0	63	8.47	13.39			
75	1.64	0.05	75	2.18	0.41	75	0.96	0.19
191	8.43	13.8	187	8.28	9.99			
289	9.64	18.0	290	11.7	20.9	286	8.39	29.62
			312	3.52	15.2			
1079	1.62	1.85	1077	1.03	1.42	1080	2.07	1.68
1124	2.06	3.14	1123	1.44	3.24	1123	2.45	2.96
1198	3.72	2.03	1192	3.39	6.90	1197	4.44	3.60
1874	7.78	11.3	1833	6.60	12.2			
3262	8.70	35.4						

The automatic estimators used was the EFDD, chosen over FDD as it provided damping estimates, and over CFDD as the later would shift user selection from chosen peaks to curve fit. It is to be noted that the quality of modal estimates is not questioned

between EFDD and CFDD. The MAC diagrams of the latter were clean with no cross correlation between automatic estimates unlike FDD, SSI-PC, and SS-UPC. In the time domain category, the SSI-UPCx was chosen as reference guide for the selection of user defined modes. It was chosen over the other two given its MAC diagram containing the least cross related mode shapes. The remaining estimators were retained as cross-validators rather than as primary identifiers.

Figure 4-3 and Figure 4-4 show the SVD plot for the EFDD selection screen and the stabilisation diagram of SSI-UPCx for block A showing the automatic mode selection on the chosen estimators. On the EFD estimation screen, the additional information provided by ARTeMIS is in the form of the background which represents the MAC value of the specific selected peak with respect to its frequency neighbourhood. On the SSI estimation, the black bands represent the inherent uncertainty component of the stabilisation line. Both sets of information were taken into account but not heavily relied on for peak picking.

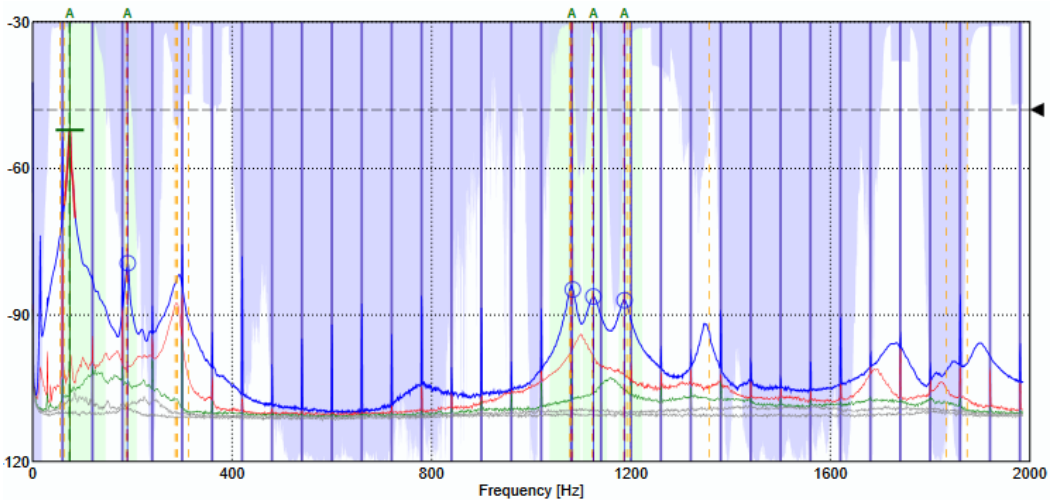


Figure 4-3: Block A EFDD automatic selection plot

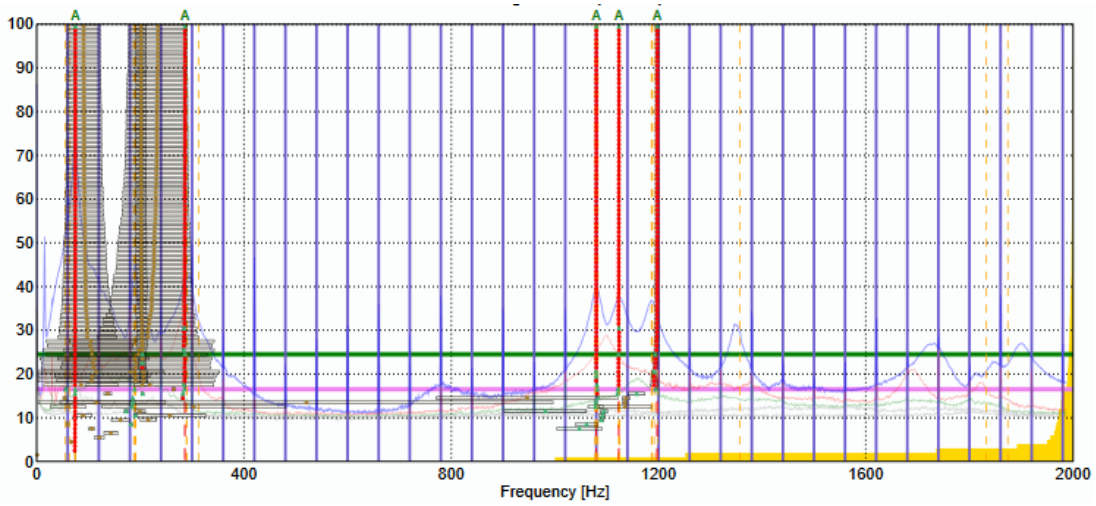


Figure 4-4: Block A SSI-UPCx automatic selection plot

Manual peak picking was restricted to one frequency-domain estimator (EFDD) to avoid circular validation in which the same peak is picked by the operator twice on different estimator displays. Three operator imposed selection criteria were applied

consistently: the peak must be at least 20 decibels above the noise floor of the SVD plot; the peak base must be at least 50 hertz wide, which is a margin against the 5-hertz width of the harmonic markers; and the peak cap must be well-defined, preferably with width below 10 hertz, since flat-top peaks were found in trial cases to give poorly-resolved mode shapes through both MAC analysis and animation.

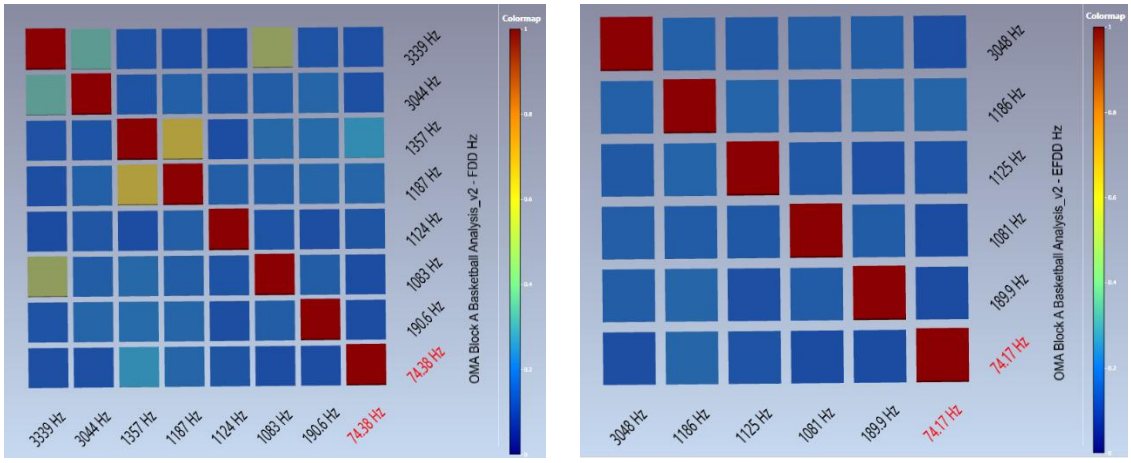
4.2.3 Validation

The modes obtained after manual selection may contain noise or rigid body modes. A final validation is needed to ensure as real modes as possible are obtained for pass-through in the FE model. The main tools available in Artemis is the MAC diagram and the mode shape visualisation animation.

The MAC diagram provides a visual measure of the similarity between the mode shapes identified by the analysis. Figure 4-5 a. and b. show the MAC diagram from block A Basketball for the FDD and EFDD automatic estimates respectively. The difference in estimates between the two is observed in the sense that while FDD provided more mode shapes, they were partly correlated with cross MAC values reaching up to 0.7. The same duplication happened for SSI UPC and PC compared to SSI-UPCx.

Modes which had above 0.2 correlation were flagged for further validation through mode shape animation comparison. Initially, the mode shapes were visualised with a shape based on the arrangement of the accelerometers on the specimens shown in Figure 4-6. This was found to be problematic as the shapes could not be properly identified. A 3D model was then made for visualisation by replicating the movement of non-existent nodes based of moving nodes in the direction of movement. This model

provided some improvement on the visualisation of the overall mode shapes, but identification of rigid body modes was still problematic. The final iteration of the shape involved pinning the bottom layer of accelerometers and removing their motion on the top layers such that rigid body modes would be quickly found and actual modes would be amplified. The first and second iteration of the 3D model is shown in Figure 4-7 and have been named OG for original geometry and RBR for rigid body removed shapes.



a. FDD MAC

b. EFDD MAC

Figure 4-5: MAC diagrams for FDD and EFDD for block A basketball automatic selections

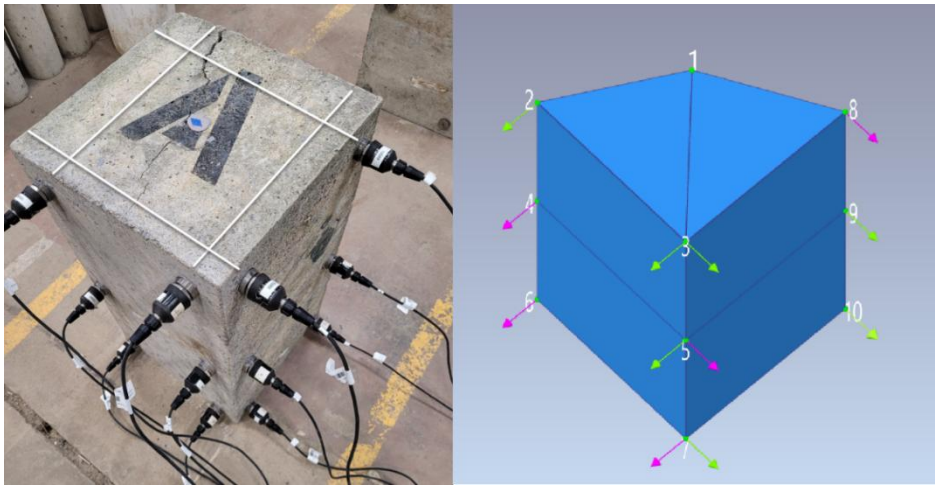
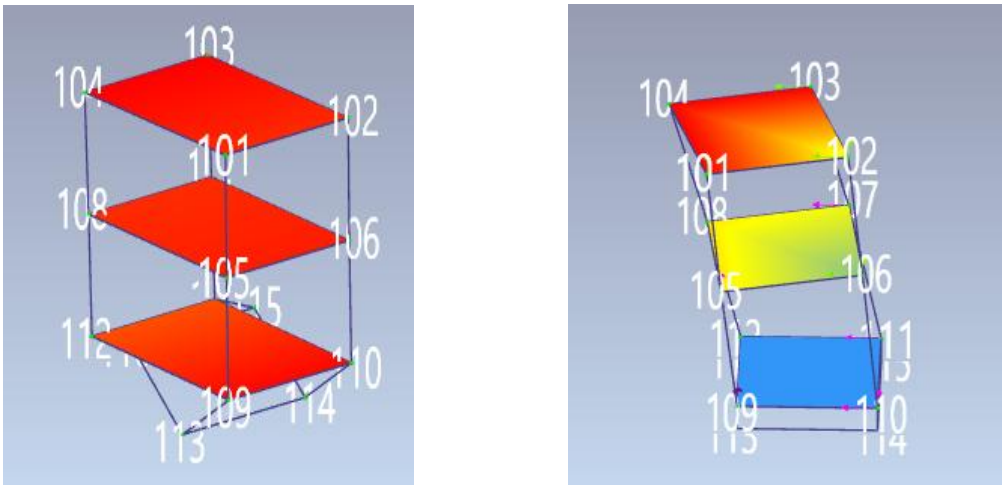


Figure 4-6: Initial modal model. As tested (left), in ARTeMIS (right)



a. **b.**

Figure 4-7: Refined model shown for mode at 189 Hz showing full motion on original geometry (OG) in a. and rigid body removed (RBR) in b.

4.2.4 Matlab Cross-Validation

Further validation and visualisation were sought from Matlab. Shown in Figure 4-8 are, the mode shapes were plotted in columns of isometric, front, side, and top views and rows of unprocessed mode shapes, as OG (top row) and pinned mode shapes, as RBR (bottom row). The latter being like the Figure 4-7 b. where the base was pinned and its movement subtracted from the two upper layers.

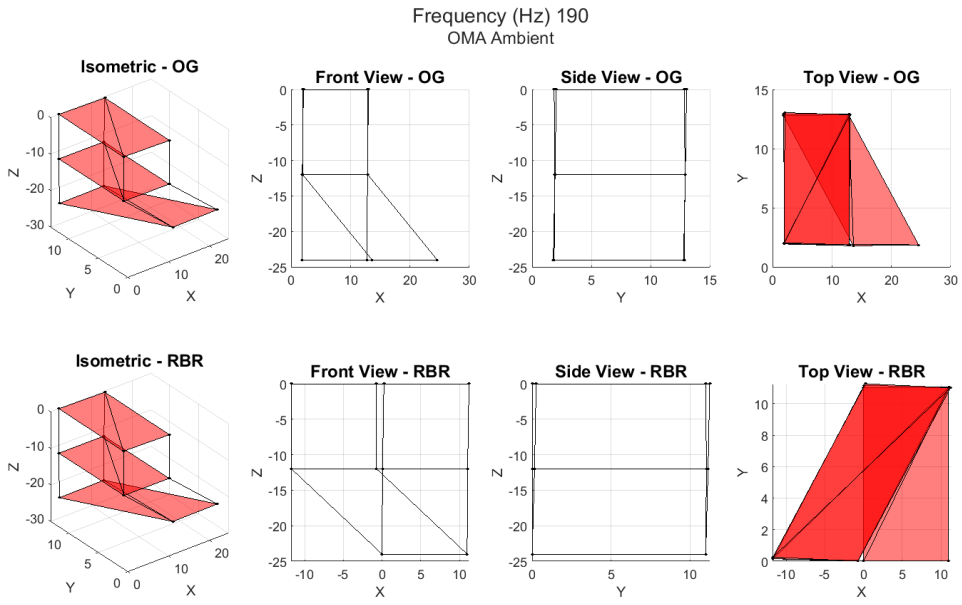


Figure 4-8: Matlab mode shape reconstruction for block A 189 Hz Ambient test

The mode shapes were exported to Matlab to be able to draw cross-estimator MAC diagrams, one function that is not available in ARTeMIS. Figure 4-9 shows the cross-estimator MAC diagram for the EFDD estimator for block A on OMA data comparing the Basketball against the Ambient tests. The expectation was that the cross-MAC would identify mode shapes across experimental methods and estimators. However, it was found to be quite unreliable since MAC values barely crossed the 0.7

threshold in the 1st modes of 15.1Hz. Good correlation was expected in the range of >0.8 to 1.0 and high mode shape complexity were assumed to cause low cross correlation.

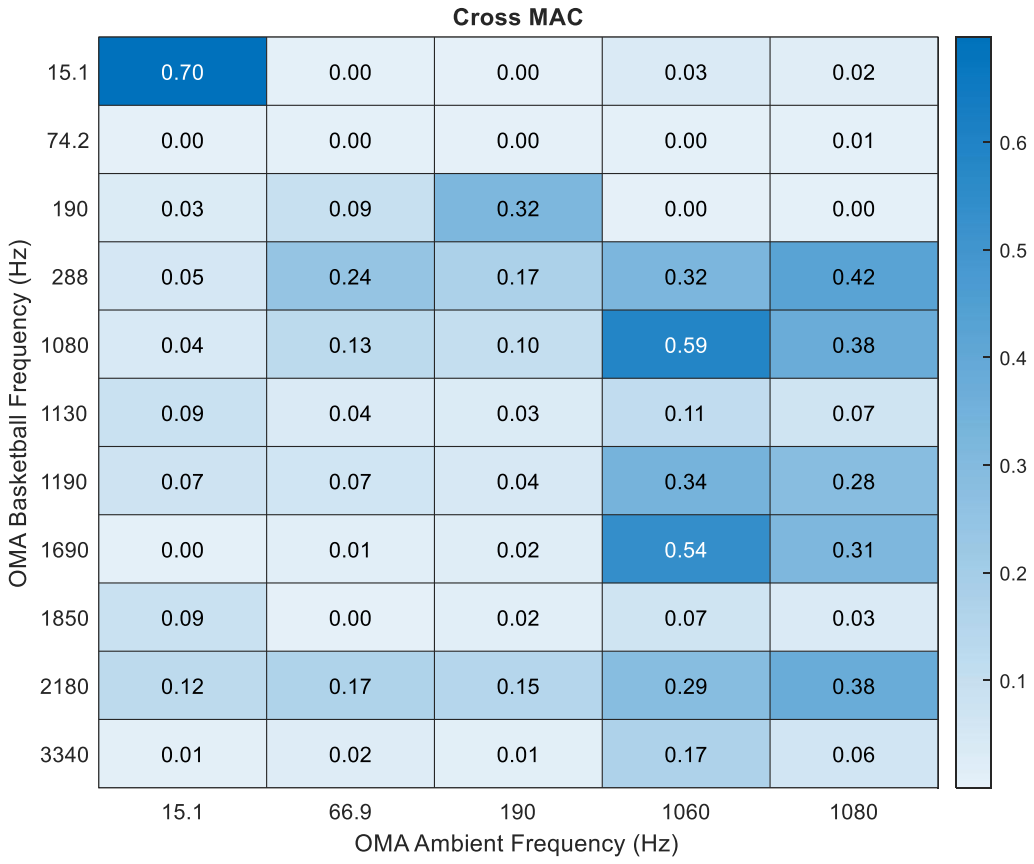


Figure 4-9: Cross MAC plot from Matlab for block A OMA Ambient vs Basketball on EFDD

A secondary form of validation was developed in Matlab after unhelpful results from the cross-estimator MAC diagram, in the form of an automated peak selection tool. Since the peak selection process on EFDD heavily depended on the first and second lines of the SVD plots, a Matlab code was developed to analyse the OMA acceleration data and perform the following: cross power spectrum calculations, SVD lines plotting,

comparison of the first and second SVD lines, and auto selection of peaks. The power spectrums were calculated using as close as block sizes used in Artemis such that the SVD plots are comparable. The Matlab produced SVD plots are included in Appendix B, along the Artemis EFDD SVD plots. The comparison of the chosen SVD lines was done as the difference in magnitude between the two and their quotient. The quotient was preferred and a dividend (S1) to divisor (S2) ratio of 1:10 was assumed to provide an enough relative change in the S1 compared to the S2 line that the first mode would be dominating at that specific point of 1:10 ratio. The difference between the two S lines were important visually in selecting peaks from Artemis but were translated programmatically by the quotient for the Matlab selection. The process is shown using the OMA Basketball SVD quotient from block A in Figure 4-10. All validation figures are also provided in Appendix B, inserted in between the Artemis selection figures. Additionally, the Modal Complexity Factor (MCF) (Structural Vibration Solutions, 2025) was overlaid on the plot. The MCF is intended to help differentiate real from imaginary dominated modes. A value of 1 or 100% on the plot represents an imaginary (bad) mode whereas a value of 0 or 0% represents a real (good) mode. The quotient value was obtained through the division of log values of the S lines, multiplied by an arbitrary scaling factor of twenty for better plot visualisation. The auto peak selection parameters were found through trial and error to be:

- Peak prominence: 10 dB, which translates to 20dB on the plot after being the same treatment as the S line data.
- Inter peak distance: 20 Hz

- Peak width: 5 Hz.

The peak width was especially important to minimise very slim peaks appearing on the selection process, as they often represented noise or rigid modes.

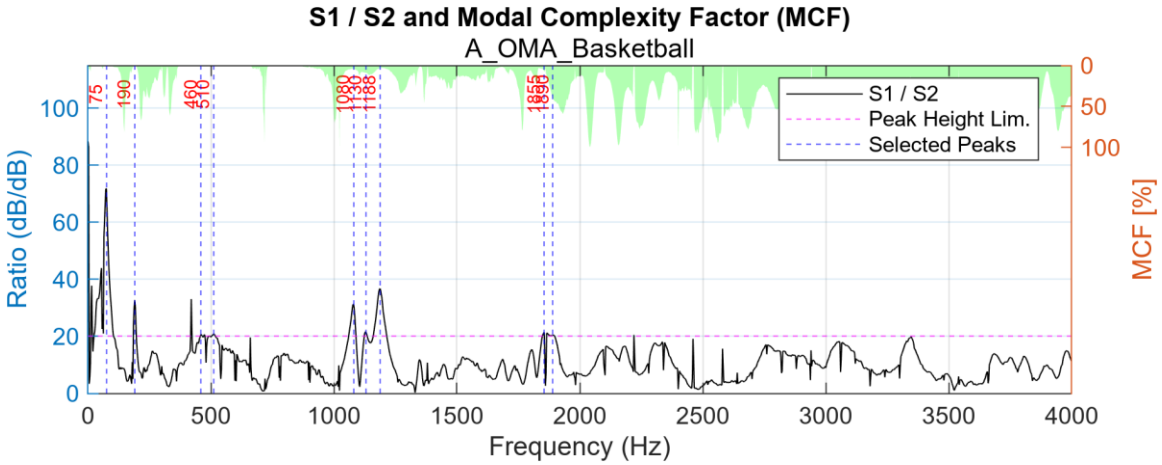


Figure 4-10: S1 / S2 Matlab rendered validation for block A Basketball

The frequencies obtained from Figure 4-10 were taken to ARTeMIS whereby they were manually select on block A Basketball data. Note that since the frequencies of 460 and 510 Hz are not on SVD peaks, there are automatically shifted to a nearest peak in Artemis. Table 4-5 shows the frequencies, damping, and complexities of the S1 over S2 peaks from ARTeMIS. Modes (3, 6, 7, 8, 9) which were selected after the whole process are italicised in the table. The tabulated modes are pictured in Figure 4-11 and the corresponding MAC values are pictured in Figure 4-12.

Table 4-5: S1 over S2 Matlab selection peaks from ARTeMIS

Number	Frequency [Hz]	Damping [%]	Complexity [%]	Mode Shape Comment
1	74	2.98	0.13	Noise.
2	190	1.58	0.27	Rigid body motion.
3	*288*	*0.78*	*27.81*	*First mode.*
4	380	1.26	0.28	Noise

Number	Frequency [Hz]	Damping [%]	Complexity [%]	Mode Shape Comment
5	412	0.45	0.07	Noise
6	*1081*	*0.88*	*4.68*	*Twisting mode*
7	*1126*	*0.85*	*9.30*	*Bending mode + Noise*
8	*1186*	*0.91*	*8.31*	*Bending mode + Noise*
9	1851	0.64	5.45	Twisting mode + Noise

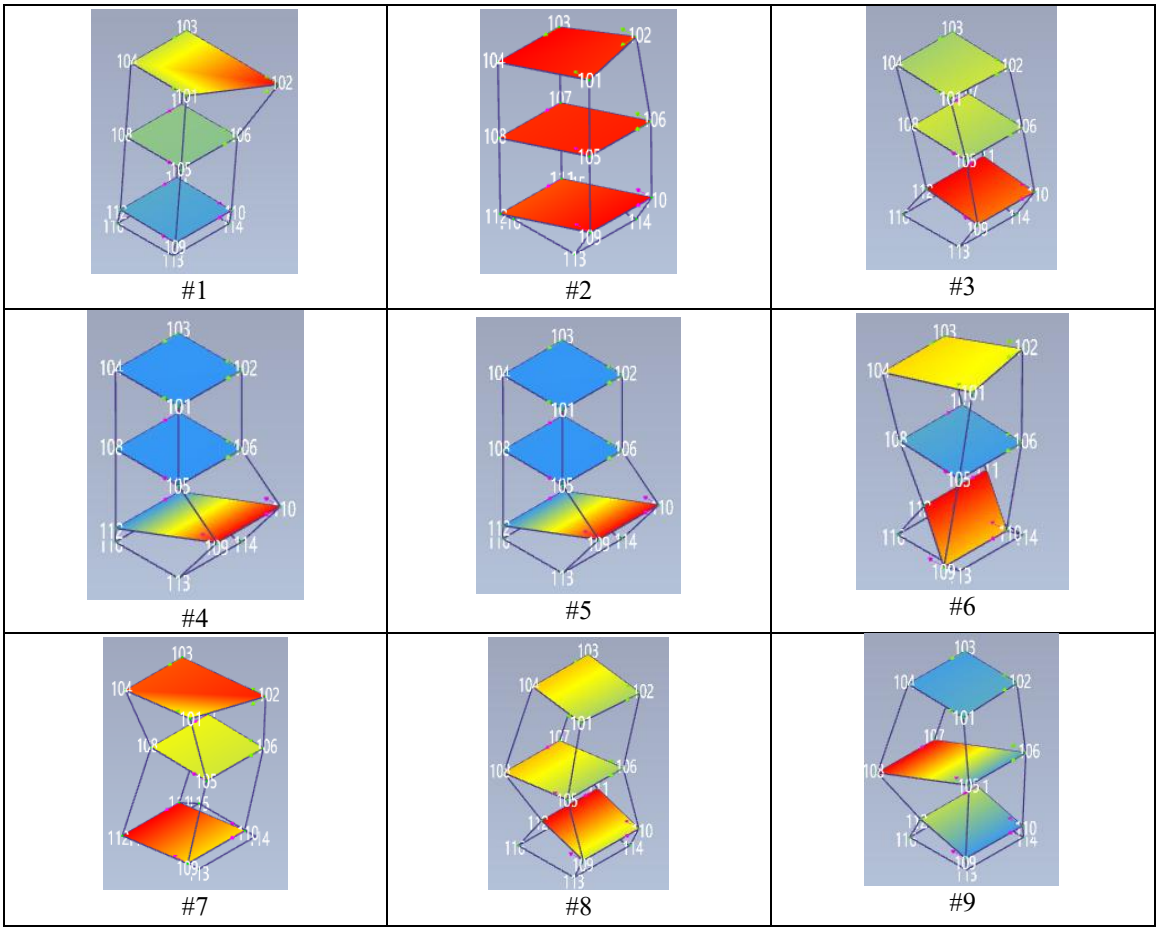


Figure 4-11: Mode Shapes obtained from the block A Basketball S1 over S2 investigation.

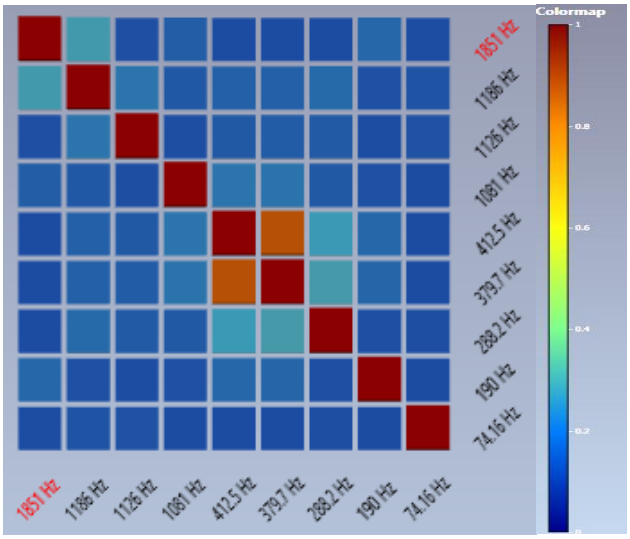


Figure 4-12: MAC diagram for the block A Basketball S1 over S2 investigation in ARTeMIS

The resulting viable modes from the Matlab validation tools developed did not provide any more information than ARTeMIS did, nor did it make the process easier. It was found that across all blocks that the S1 over S2 quotient process missed many of the viable modes, especially the first modes. This is shown in Appendix B for block A, in the table of extracted modal parameters where the Matlab found modes are bolded.

The main selection process for mode shapes depended on ARTeMIS's mode shape animation. Since half of the specimen geometry was not instrumented and the free node movement were paired, the mode animations were compared to Abaqus mode shapes for validation. Developing such capabilities in Matlab would be wasteful for this study since it is already available in ARTeMIS, therefore any Matlab validation was not used to validate modes nor find them. It is noteworthy to point out the Matlab was programmed by the operator to pick out modes using what the operator has been

implicitly applying in ARTeMIS. Tighter parameters were used in Matlab, but they did not help in mode identification.

4.2.5 Final Analysis Sequence

Since validation was sought only within ARTeMIS, the following sequence of operations were implemented on all blocks in ARTeMIS for all test data:

- Pre-processing and addition of harmonics peak indicators.
- Automatic mode estimation from all time and frequency domain estimators.
- On EFDD for OMA and CMIF for EMA, selection of any well shaped peaks that have been missed by any other estimators. Manual selection is made on only one frequency domain estimator to avoid a circular validation.
- Validation step on MAC diagram: removal of any modes with >0.6 correlation to any other three modes. A threshold of three modes has been chosen since some modes may coincide with each other in the case of twisting and bending which may be hard to differentiate.
- Cross validation on animation: modes which show high cross correlation are removed based on complexity or similarity between shapes. This is in addition to keeping the Abaqus mode shape as reference guide.
- Removal of modes selected based on peaks on SVD diagram. In this step, peaks from the SSI or RFPz estimators which are not centred on a peak are removed.

The results of this investigation are presented in Appendix B for block A. The results are laid out in the following manner:

1. Presentation of all plots used for selection, such as, the EFDD and SSI plots for OMA and CMIF and RFPz plots for EMA. The Matlab S1 over S2 validation plots are presented under their respective ARTeMIS counterparts for completeness.
2. Presentation of selected mode shapes based on peaks in a data table format.
3. Presentation of associated mode shapes from the data table. The mode shapes are shown raw (as measured with inactive nodes slaved to measured nodes) and with rigid body motions removed.
4. Selection and presentation of cross validated modes and frequencies.

The animation step was important in cases whereby the MAC diagram would not differentiate modes due to different phases. For example, Figure 4-13 shows two modes on the validation step for Block A forced ambient (basketball) test. The MAC diagram for which blue is zero correlation and red is maximum correlation of 1, does not show any correlation between the two modes. However, the animation step clearly shows that they are similar and are only out of phase by about 180 degrees. This phenomenon arose because of the way the MAC values are calculated as a result of the MAC being a cosine of the angle between two vectors resulting in a +1 value for when the angle is 0 or 180 degrees (Towner & Band, 2012).

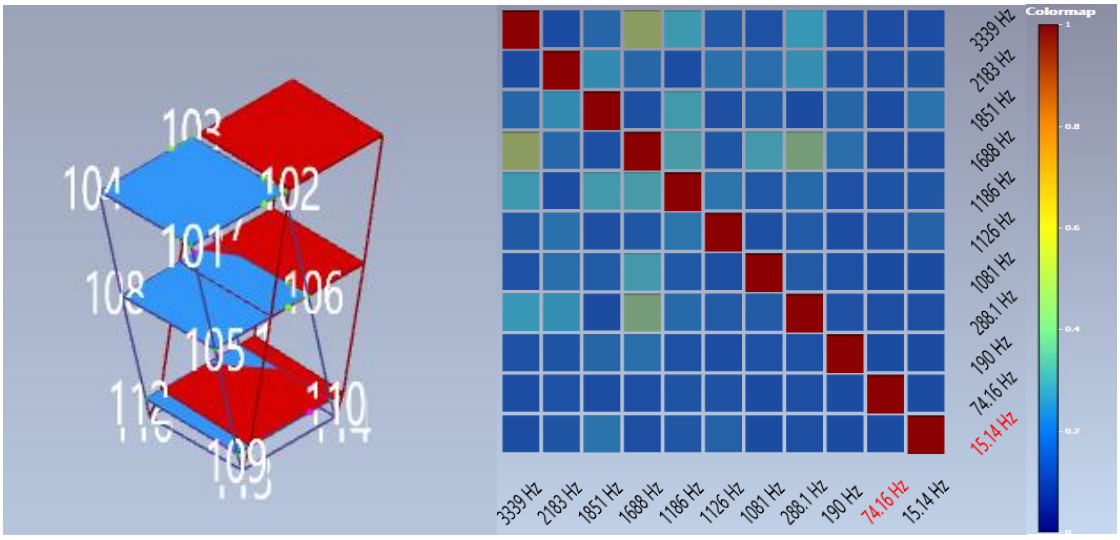


Figure 4-13: Modes at 15 and 74 Hz for block A for Basketball with MAC diagram

4.3 Results

This section presents the results of the modal analysis process performed on the experimental data. Only the frequencies of the blocks tested for mode 1 are deemed reliable to be used in the modelling part of this study in Chapter 5. The modal information is tabulated as selected, then a comparison is performed to investigate whether the first modal frequency can be used to assess ASR progression or extent within the specimens.

4.3.1 Frequency Results

The results of the modal testing for all blocks are presented in Table 4-6. The first column provides the mode names, and the REF columns provide eigen frequency values, as modelled in Abaqus, for uniform MOEs of 10 and 30 GPa. Reactive blocks are bolded and underlined. Mode 4 and 10 are voided since the instruments could not feasibly detect them. The blue highlights modes in the Mode 2-M and 9-M rows indicate (degenerate)

mode pairs, with the M denoting Mirror. The orange highlights denote modes for which the validation step was not conclusive, i.e., they denote low confidence modes.

The frequencies tabulated in Table 4-6 are a band average of several estimators. The averaging process was implemented as follows; for each frequency band denoted as a row in the extracted modal parameters table for any block, the frequency of any selected mode is averaged for all estimators which yielded non noise modes. For example, the reported frequency for the first mode for block A is 285 Hz. The selected frequencies are 288 Hz in EFDD and 281 Hz for SSI-UPCx as shown in the table of extracted modal parameters in Appendix B.

The entirety of the tests yielded only mode 1 frequency results. No mode shape vectors nor other modal parameters were extracted because of the mode shape uncertainties associated with the test data. Due to the out of reference (REF columns) bounds of frequencies of mode 3 and above, and the uncertainty in matching mode shapes to FE shapes, only the first modes of all blocks were judged reliable and correctly ordered to be used.

Table 4-6: Modal testing results: Modal Frequencies

Block	REF-10	REF-30	*A*	AA	AC	AB	*AN*	AS	*F*	*R*
Mode 1	**214**	**370**	285	309	268	246	231	342	191	271
Mode 2-M	214	370		329		266		372	216	296
Mode 3	**434**	**751**	1082	1500	1548	1549	1172	1638	1058	1147
Mode 4	**729**	**1263**								
Mode 5	**794**	**1375**	1113	1567	1689	1768	1295	1837	1172	1163
Mode 6-M	794	1375	1186	1636	1721			1860		1178
Mode 7	**1298**	**2247**	2032				1737		1933	1852
Mode 8	**1649**	**2857**					2054			2109
Mode 9-M	1649	2857								
Mode 10	**1861**	**3223**								

4.3.2 Comparison of Frequency against Expansion.

This section attempts at comparing the resulting first modal frequencies to the individual block expansion levels, as measured in 2022, and by proxy, their ASR extent. A bar chart of the measured first frequencies of all blocks is presented in Figure 4-14. The reference frequencies for 10 and 30 GPa specimens obtained from Abaqus are presented first, followed by the 4 reactive blocks, then the 4 non-reactive blocks. Upon inspection, it is shown that there is no apparent clear delineation between reactive and non-reactive blocks based on the first measured frequency alone. The reactive group spans 191 to 285 Hz; the non-reactive group spans 246 to 342 Hz; the two groups overlap across the 246-to-285-hertz band, with four blocks in the overlap region. The overlap does not preclude a directional difference in the population means, but it does preclude any classification of an individual block on the basis of its first frequency alone.

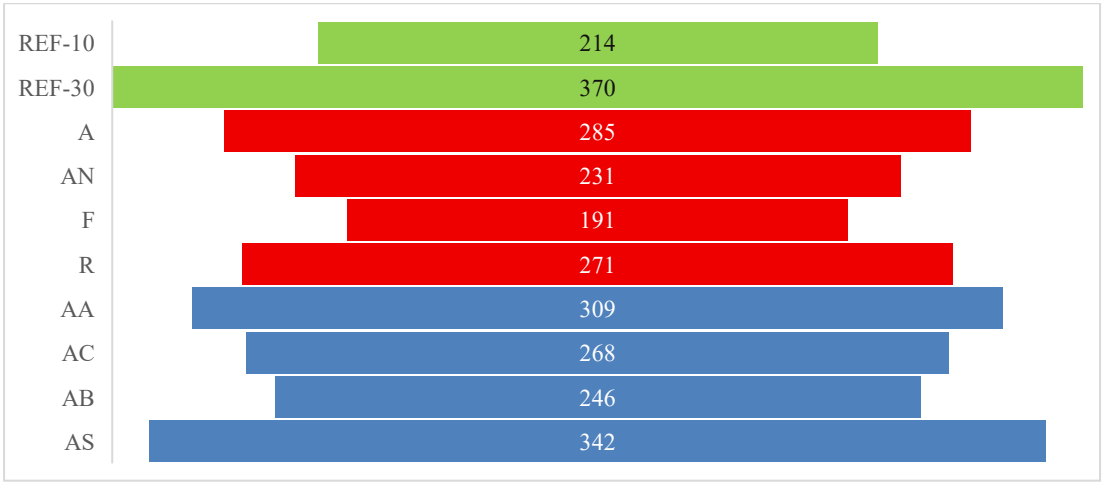


Figure 4-14: Bar chart of first measured frequencies (Hz)

A scatter plot of the normalised frequency difference against expansion strain of the blocks with respect to block AC is provided in Figure 4-15. Block AC has been chosen as reference block because its measured expansion is closest to zero among the specimen set. The expansion is provided as a strain measurement, and the normalised frequencies differences are provided as percentages. The linear regression obtained, R2, is 0.226 and is implicitly the same when non normalised values are compared. The choice of presenting the data this way was to investigate whether a clear relationship of reactive vs nonreactive blocks is present.

Unlike Figure 4-14 which is about frequencies only, it was expected that some differences might have been more visible with the expansion shown and with only the first natural frequencies. It is to be noted that the gap between the < 0 strain and the >0.3 strain is expected as the blocks in the study are either nonreactive or very reactive. The nonreactive blocks are clustered in the 246 to 342 Hz range while the reactive blocks are clustered in the 191 to 285 Hz range. There is an overlap of four specimens (two of each category) in the 240 to 290 Hz range.

Table 4-7 presents the comparison data, except for also providing the normalised strain and frequency values with respect to block AC. Reactive blocks are bolded.

The lack of a clear relationship between the first frequency and expansion implies that at this specimen scale and instrumentation, the first frequency is not a reliable indicator of ASR expansion. Each block had different and unmeasured initial concrete properties, suggesting that the reaction affected these differently based on factors not measured in this study.

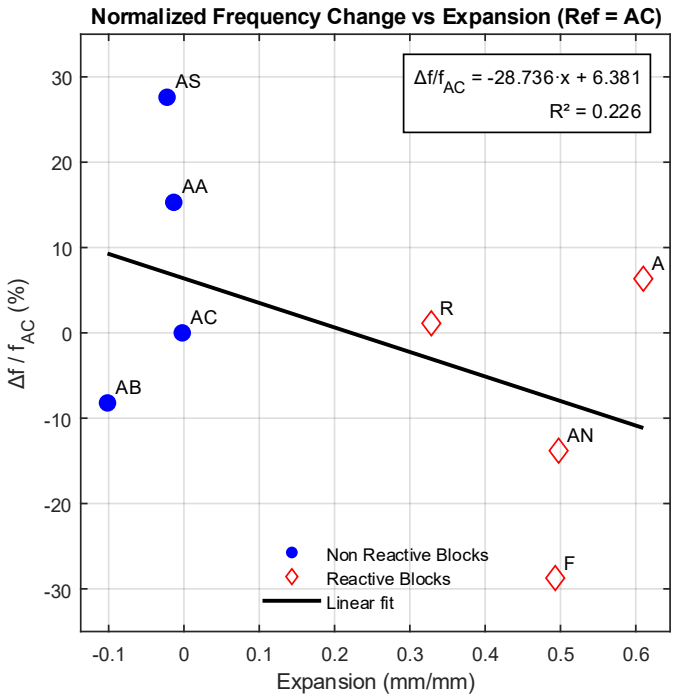


Figure 4-15: Scatter plot of normalised frequency and expansion strains to block AC

Table 4-7: Summary of frequency to strain comparison values

Name	Aggregate	Cement	Alkali Content (%)	Strain (mm/mm)	Strain (AC)	F1(Hz)	F1(AC)
A	Mactaquac Greywacke	Brookfield	0.91	0.610	-270.9	285	1.06
AN	Springhill #3 quarry	Dragon	1.25	0.498	-221.1	231	0.86
F	Springhill #3 quarry	Brookfield	0.91	0.493	-219.1	191	0.71
R	Springhill #3 quarry	Brookfield	1.25	0.329	-146.0	271	1.01
AA	Springhill #3 quarry	Mix	0.75	-0.014	6.0	309	1.15

Name	Aggregate	Cement	Alkali Content (%)	Strain (mm/mm)	Strain (AC)	F1(Hz)	F1(AC)
AC	Springhill #3 quarry	Mix	0.62	-0.002	1.0	268	1.00
AS	Springhill #3 quarry	St. Mary's	0.50	-0.022	10.0	342	1.28
AB	Springhill #3 quarry	Mix	0.50	-0.102	45.1	246	0.92

4.4 Discussion

The results obtained from the data analysis were presented in Table 4-6, with a double line separator underneath the second mode order. The reasoning for this being that it is very highly probable that the natural frequencies identified after the second mode are either erroneous or wrongly placed. The first two frequencies are readily identified as there is a clear mode pair for those modes, and they move perpendicularly given the symmetry of the structure. During the analysis, other than rigid body movement in the 190 Hz range, the first two natural frequencies were found with greater ease than any of the following modes. The areas of difficulty in identifying the higher modes are consequently discussed.

4.4.1 Mixed Modes and Instrumentation Concerns

The presence of mixed mode shapes around actual modes with no clear domination made identification harder, even with the use of the complementary Matlab implemented validation tools. Even with greater scrutiny of mode shapes, possible errors

on the frequency or mode shapes could have passed through. This is especially important on the mode shape aspect.

In the literature review concerning FEMU, the mode shape is often analysed using qualitative or MAC methods. Both proved to be difficult because of the shortage of sensors compared the number of nodes required to properly identify the modes of a block. Two considerations were at play; first, identification of planar modes for which the number of accelerometers increases for each bending 'wave' introduced on the place surface, and secondly, the number of faces measured on the block (4). To better manage the 2 accelerometers with a comparable data from both EMA and OMA, the current test setup was followed. However, not only did this limit EMA tests in the way of limiting the number of faces analysed, not having the other two faces measured for OMA meant that the mode shapes obtained had to be post processed through the introduction of slaved movements to the non-measured faces. This certainly provided better visualised modes, but not actual modes. The slaved nodes could have behaved differently. While this procedure is essential for constant qualitative modal identification, for both the slaved, and slaved + pinned (rigid body movement removed) transformations in Artemis, mode shapes and their associated MAC values would have been better if there were more accelerometers to capture the totality of the specimen movements.

EMA results consistently showed no lower modes indicating a significant issue with the hammer input. This limited the testing capabilities in half, but was unavoidable, lest different hammer sets and specimens support been used. This would have been a parametric study in itself and is surely an endeavour for future studies,

4.4.2 Input Excitation

There is an apparent dead zone in all OMA data in between the 350 to 1100 Hz range where next to no reliable peaks were found. This apparent dead zone in the SVD plots corresponds to modes 3 to 6 on the 10 GPa reference block and to modes 1 to 3 on the 30 GPa reference block. It is highly possible that many modes were mislabelled or completely omitted from the apparent lack of peaks in this zone. A possibility for this phenomenon is the quality of the vibrations exciting the specimen in the laboratory. For example, when comparing the ambient to basketball SVD plots, it is apparent that the ambient only energy is focused on the electrical harmonics. Consequently, the basketball energy content comes primarily from the basketball dribbling with mixed inputs from the experimenter movements, then from the laboratory surrounding. As inferred from the dead zones in the SVD plots, the forced ambient vibrations missed parts of the required frequency bandwidth. This could have been prevented by using a shaker or vibrator, but it would not have been a 'true' OMA test since forced vibration would have been used. Ambient vibrations from the laboratory environment seemed to have been overpowered with electrical noise and the resulting data from the Ambient tests do not correlate with ambient vibration testing surveyed in literature. It can only be assumed that there was not enough random noise to overpower the electrical noise in the power cables and especially the running machines within the laboratory.

4.4.3 Mode Order

The natural frequencies obtained past mode 2 are also found to be out of range from the reference eigen frequencies as blatantly demonstrated in the mode 3 row of

Table 4-6. For example, block A, mode 3 is 1082 Hz. It has been verified by comparison of the mode shapes. However, it only fits in the next reference range, mode 4, which is an axial mode and cannot be seen through mode shape given the lack of triaxial accelerometers. While modes 5 and 6 for block A were placed in their orders by the same reasoning of mode pairs as for modes 1 and 2, mode 3 is an errant, unsure mode. This raises the question of being able to place modes in their orders without MAC values, and without having all modes available. Even if the modal frequencies occur in a range of values, if one of the modes cannot be placed properly, the following modes are therefore very likely to be misplaced as well.

Furthermore, there are 2 axial modes, as identified in the FE modelling phase. Due to a lack of proper number of triaxial accelerometers, those could not be measured. Even though they were interfering with other modes during analysis, these modes could not be validated. While mode 10 is irrelevant in this aspect, mode 4 posed a serious problem in matching natural to eigen frequencies since its position left a blank spot in the match orders.

4.4.4 Ending Remarks

However, modal frequency misidentification or frequency loss in this study is an important finding in itself. Since only the first frequency was reliably identified in this study, it is likely that it will be the case in other studies as well using weighty specimens. Dealing with an incomplete set of modal data, both frequency and shape wise, would be an important consideration for this type of FEMU process.

The nonreactive blocks: AB, AS, A, and AC all have the same SpringHill #3 aggregates, and have an alkali content to less than 0.75%. the only significant difference amongst them would be their strains. Blocks AB and AS are at the extremes of the measured frequencies at 246 and 342 Hz respectively and have relative expansions of 45 and 10 times that of block AC. The available metrics are the alkali content and strain, none of which having a relationship with measured frequencies.

The reactive blocks A, AN, F and R have similar aggregate types, and their alkali contents are in pairs of 0.91 and 1.25%. Blocks A and R have the highest anomalous frequencies at 1.06 and 1.01 times that of block AC but have strains of 270.9 and 146 times that of AC, and they encompass the strains for the other reactive blocks. Since all other parameters in concrete casting were kept the same, there is no relationship between measured first frequencies compared to ASR expansions or block mixes.

4.5 Summary and Conclusions

4.5.1 Summary

The modal analysis operation resulted in three positive outcomes and one operational limitation to the FEMU framework. The first positive result is that the first natural frequency was reliably identified for all eight specimens, spanning the band from 191 hertz (Block F) to 342 hertz (Block AS). The mirror Mode 2 was identified for five of the eight specimens (AA, AB, AS, F, and R). Modes 3 and beyond did not survive cross-validation with confidence at the present instrumentation setup. The second positive result is the frequency-band specialisation between OMA and EMA. The OMA-Basketball regime outperformed both OMA-Ambient and EMA below approximately 1

800 hertz, while EMA-Hv outperformed both OMA regimes above that frequency. This specialisation was not anticipated in advance of the test campaign and has design implications for any subsequent campaign at this specimen scale: a complementary excitation strategy that combines a low-frequency-rich OMA source (basketball or equivalent) with a high-frequency-rich EMA source (impulse hammer with appropriate tip selection) is the natural pairing for the present specimen geometry. The final positive outcome is the cross-validation process in ARTeMIS worked as a reliable filter against noise and rigid body modes. The removal of bottom nodal motion and the use of the mode shape animation were effective against the limitation of half the node point coverage of the specimens during testing.

The operational limitation identified is that no measured frequency was reliably obtained for all blocks past the first mode.

4.5.2 Conclusions

The lack of a clear relationship between frequencies and expansions suggests the following hypotheses:

- The blocks' modal response is affected by factors other than pure expansion, such as environmental to concrete interactions, or ASR degradation is independent of the concrete itself.
- The blocks had non-equal modal and material properties at cast time, none of which were measured, and the reaction has evolved each specimen from a different starting point.

This study is comparative, not direct in the sense that ASR cannot be clearly assessed through modal testing alone. It means that multiple specimens, of varying degrees of expansion were measured at one specific point in time. Multiple measurements need to be made for comparison, and a baseline measurement should have been made when the blocks were cast. Current field ASR measurements are also comparative, such as the length gauge measurements, which also require a baseline to compare against for ASR expansion.

This proposes a new direction for this type of testing, that of comparative compared to direct tests. Comparative testing in this context would mean testing at intervals of time determined by the S-curve of the ASR expansion to obtain modal readings that can be correlated, at a minimum, to the pre-expansion state, the start of the expansion, the maximum rate of expansion and on the descendant of the expansion curve. Such readings could be used to physically compare how modal readings compare with different levels of expansion.

Overall, OMA performed better on the lower frequencies, especially the first one, compared to EMA which was better in frequencies above 1000 Hz. The majority of the actionable data was obtained from OMA since EMA was plagued with poor mode shape visualisation, making order placement poor for higher modes without lower reference modes.

However, a clear distinction of OMA being better for modal testing as opposed to EMA will not be made. Such is the case as the EMA tests were not done to the best of their capabilities. However, to confirm whether OMA is truly better than EMA, both tests need to be conducted using appropriate instruments such as impact sledgehammers or

shakers for EMA paired with roving accelerometer, and for OMA, triaxial accelerometers paired with broadband, random ambient excitation. The most important point being that for both tests, optimum input and outputs needs to be obtained. It is expected that they will perform equally.

5 Finite Element Modelling

5.1 Introduction

This chapter contains all of the finite-element work in this thesis. Sections 5.1 through 5.4 present the preliminary FE analysis used to size the specimens dynamically and to plan the modal experiment. Sections 5.5 through 5.10 cover the model-updating implementation: the algorithm-selection trial, the FE-model levels considered, the modelling efforts undertaken at each level, and the results obtained.

5.2 Preliminary Studies

The preliminary FE studies served two purposes. The first was to investigate the expected frequency range and mode shapes of the specimens, to be used as a guide during specimen testing for the experimental works as well as the modal analysis in Chapters 3 and 4. The second was to obtain a working model for the model updating and to investigate the expected changes in MOE based on changes in eigenfrequencies. The first purpose is discussed in Section 5.2 while the second is discussed in Section 5.3.

The FEMU implementation as from Section 5.5 builds upon the preliminary work and uses the modal analysis data in an effort to quantitatively assess the ASR extent in each of the specimens. The primary constraint is the lack of more than the first modal frequency per specimen as reliable input data.

5.2.1 Modelling assumptions

The model was created in the Abaqus FE engine based on several assumptions as follows:

1. The material is assumed to be a homogenous isotropic material with no inherent damage. Models using non-linear material properties will not be used to keep the FE exploration simple.
2. The elasticity parameters to be assumed for the model are the modulus of elasticity (MOE) or Young's modulus, the Poisson's ratio, and the density. Discussions with the specimens' handler, the late Dr. M.D.A. Thomas (M.D.A Thomas, *personal communication*, 2020), yielded that the samples would have an approximate MOE of 28.5 GPa and a density of 2350kg/m^3, which are within range for normal concrete. While the exact mix design was not found in literature, a similar mix design (Giaccio et al., 2008) was found with MOE values ranging from 13.1GPa for a fast-reacting aggregate and 30.1 for a slow reacting aggregate. The Poisson's ratio was found within a smaller range of 0.19 to 0.22 for the mixes (Giaccio et al., 2008), but a definitive value of 0.2 is taken as recommended by V. Saouma (2013, 6.2.3).
3. The boundary conditions for the block, resting on its end face, would be assumed to be a pinned face instead of an encastre condition. There were no modelling differences between pinned or encastre nodes.

5.2.2 Model generation

The model is a solid extrusion of dimensions 0.38 by 0.38 by 0.71 metres, defined in Abaqus as a three-dimensional deformable solid. The MOE is varied through the analyses from 10 to 50 gigapascal in 5-gigapascal steps in the preliminary sweep (Section 5.3) and from 10 to 40 gigapascal in 0.5-gigapascal steps in the data-table generation

(Section 5.8.1). The analysis step is a linear perturbation in Abaqus, which extracts the eigenfrequencies and eigenmodes of the model.

5.2.3 Mesh convergence studies

Using the generated model, an optimum set of modelling parameters for mesh size, aspect ratio, and element type must be determined to have valid and converging results in the shortest amount of time. A pathway to obtain such modelling parameters is to optimise for mesh size or number of elements, verify if aspect ratio influences the results, then iterate through the available element types.

5.2.3.1 Effects of the Number of Elements

The first step in the convergence study is to investigate if the number of modelled elements has any effect on the results required and up to what number of elements do the results converge. This information can then be used to justify using a lower density of mesh elements as a compromise between execution speed and result accuracy. The mesh convergence study was carried out by varying the number of elements in the model from 8 to 21952 by seeding the edges with different amounts of seed intervals. Table 5-1 shows the results of the mesh convergence study in terms of the eigenfrequencies produced and with their respective percentage difference with respect to the model with 21952 elements as reference. A tight convergence criterion, with respect to the highest mesh density, of 1% was chosen and is reflected in the red highlights in the table.

The computational requirements of tests with up to 2744 elements were negligible and happened within 10s while the last 2 tests required an increased amount of memory allocation than the default nominal value and had computational times of >15s. A final

test of 64000 elements was carried out but had to be aborted due to exorbitant amount of memory and computational time required.

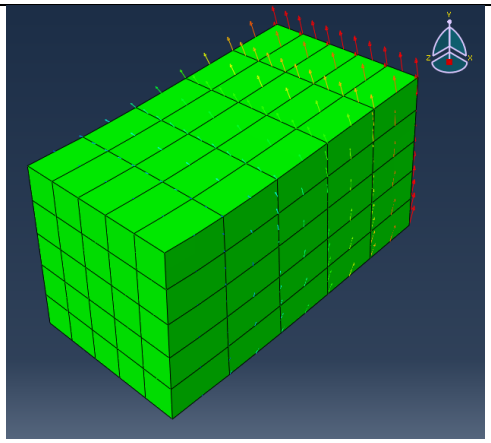
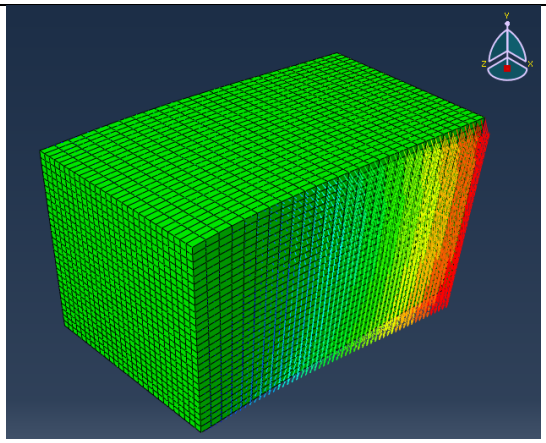
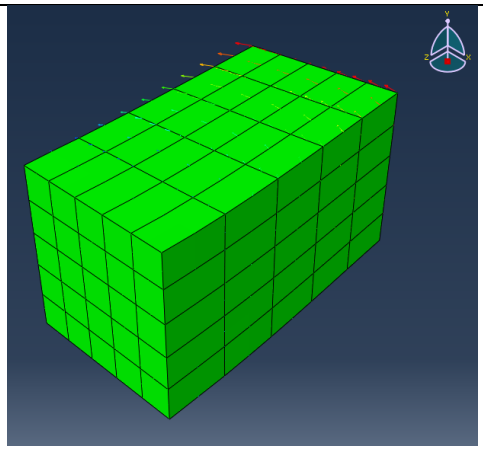
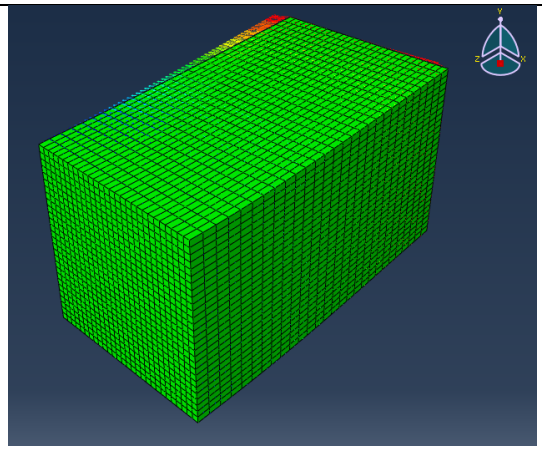
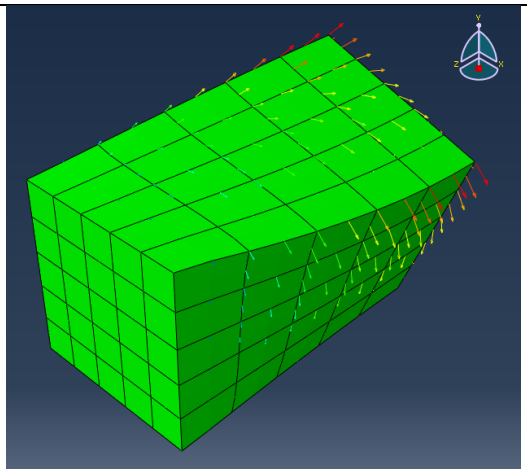
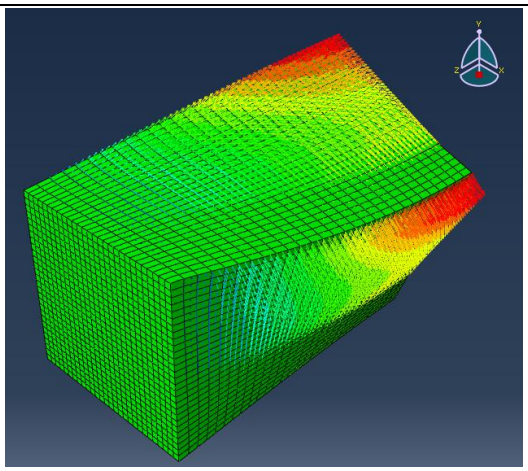
Table 5-1: Mesh convergence study on the effects of mesh element density

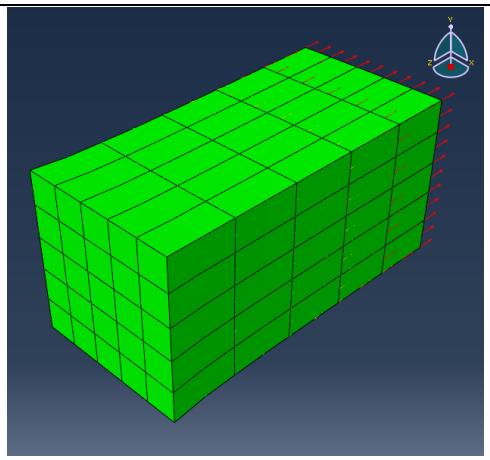
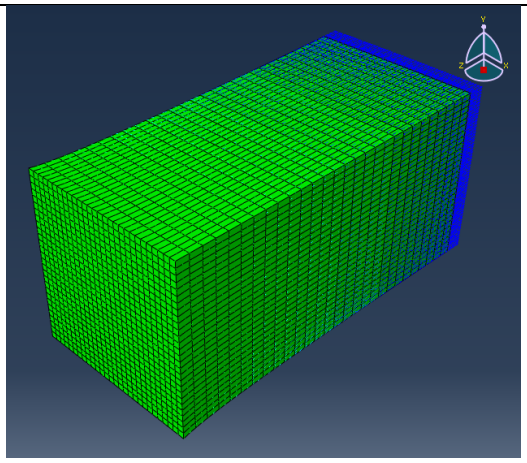
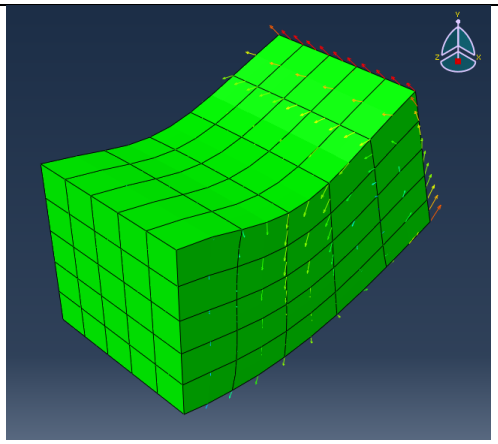
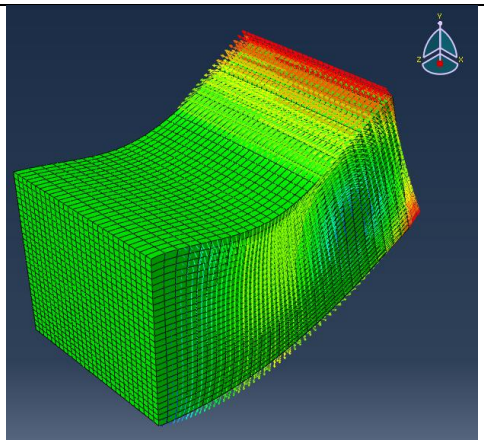
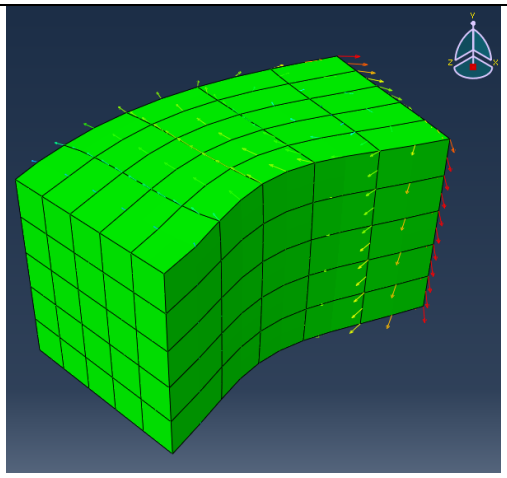
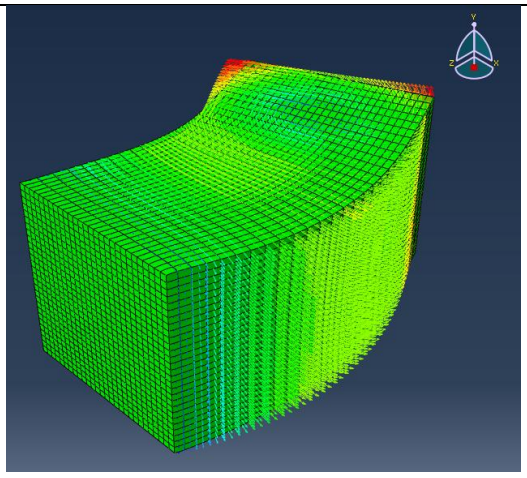
Mesh Size	Eigenfrequency Number									
	Percentage Difference to Max Elements									
	1	2	3	4	5	6	7	8	9	10
8	364.50	364.50	748.00	1234.30	1403.47	1403.47	2320.69	2994.26	2994.26	3124.04
	1.08	1.08	2.09	0.17	4.65	4.65	5.83	7.46	7.46	0.82
64	361.58	361.58	734.94	1233.14	1348.00	1348.00	2204.64	2821.83	2821.83	3147.87
	0.27	0.27	0.31	0.08	0.51	0.51	0.54	1.27	1.27	0.07
125	361.27	361.27	733.96	1232.90	1344.86	1344.86	2198.65	2802.54	2802.54	3149.04
	0.18	0.18	0.18	0.06	0.28	0.28	0.27	0.58	0.58	0.03
216	361.09	361.09	733.49	1232.74	1343.45	1343.45	2196.17	2795.15	2795.15	3149.48
	0.13	0.13	0.11	0.04	0.18	0.18	0.16	0.32	0.32	0.01
343	360.98	360.98	733.23	1232.63	1342.71	1342.71	2194.94	2791.71	2791.71	3149.68
	0.10	0.10	0.08	0.03	0.12	0.12	0.10	0.19	0.19	0.01
512	360.90	360.90	733.07	1232.55	1342.26	1342.26	2194.25	2789.89	2789.89	3149.78
	0.08	0.08	0.05	0.03	0.09	0.09	0.07	0.13	0.13	0.00
729	360.84	360.84	732.97	1232.49	1341.98	1341.98	2193.83	2788.82	2788.82	3149.84
	0.07	0.07	0.04	0.02	0.07	0.07	0.05	0.09	0.09	0.00
1000	360.80	360.80	732.90	1232.44	1341.78	1341.78	2193.56	2788.16	2788.16	3149.87
	0.05	0.05	0.03	0.02	0.05	0.05	0.04	0.06	0.06	0.00
1331	360.77	360.77	732.85	1232.40	1341.64	1341.64	2193.37	2787.71	2787.71	3149.89
	0.04	0.04	0.02	0.02	0.04	0.04	0.03	0.05	0.05	0.00
1728	360.74	360.74	732.81	1232.37	1341.53	1341.53	2193.24	2787.41	2787.41	3149.90
	0.04	0.04	0.02	0.01	0.03	0.03	0.02	0.04	0.04	0.00
4096	360.68	360.68	732.73	1232.29	1341.30	1341.30	2192.96	2786.79	2786.79	3149.92

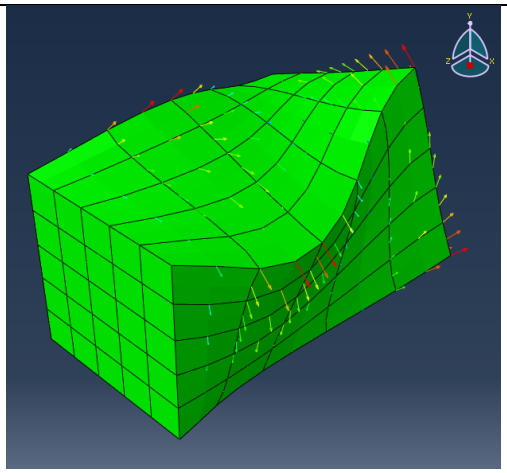
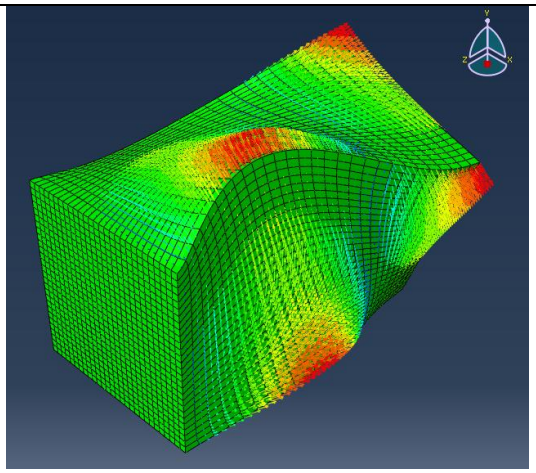
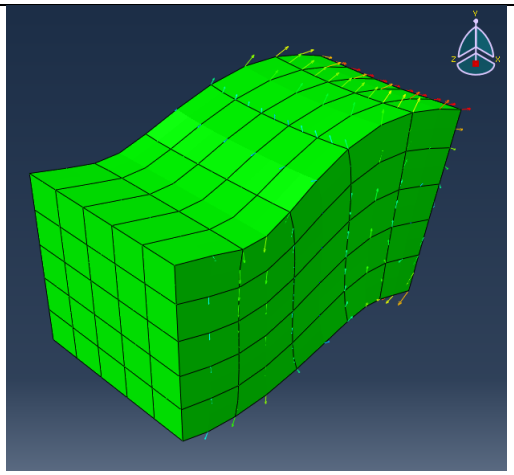
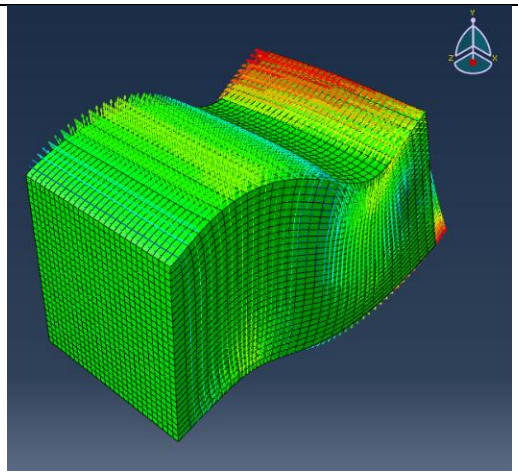
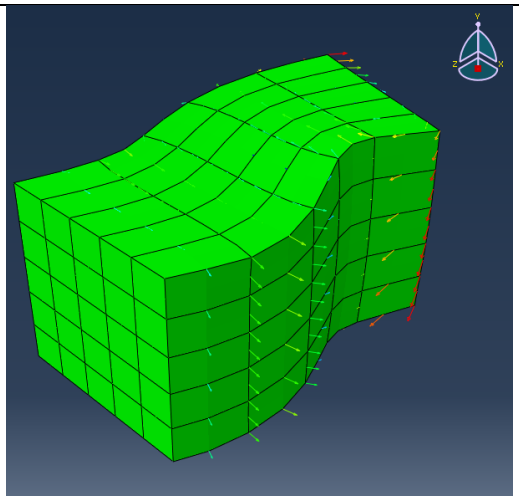
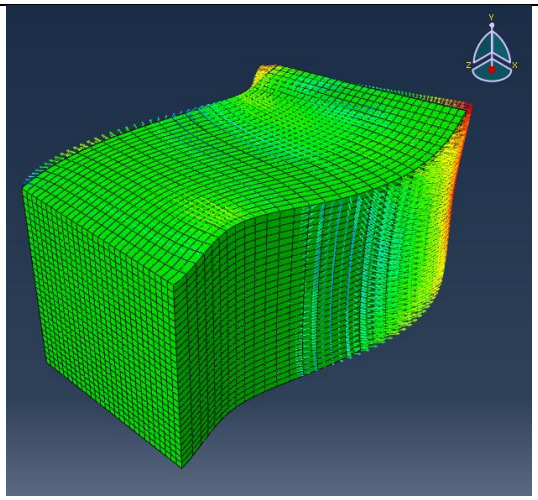
Mesh Size	Eigenfrequency Number									
	Percentage Difference to Max Elements									
	1	2	3	4	5	6	7	8	9	10
	0.02	0.02	0.01	0.01	0.01	0.01	0.01	0.02	0.02	0.00
8000	360.64	360.64	732.70	1232.25	1341.19	1341.19	2192.84	2786.55	2786.55	3149.93
	0.01	0.01	0.00	0.00	0.01	0.01	0.00	0.01	0.01	0.00
13824	360.62	360.62	732.68	1232.22	1341.14	1341.14	2192.78	2786.42	2786.42	3149.93
	0.00	0.00	0.00	0.00	0.00	0.00	0.00	0.00	0.00	0.00
21952	360.61	360.61	732.67	1232.21	1341.10	1341.10	2192.75	2786.35	2786.35	3149.93

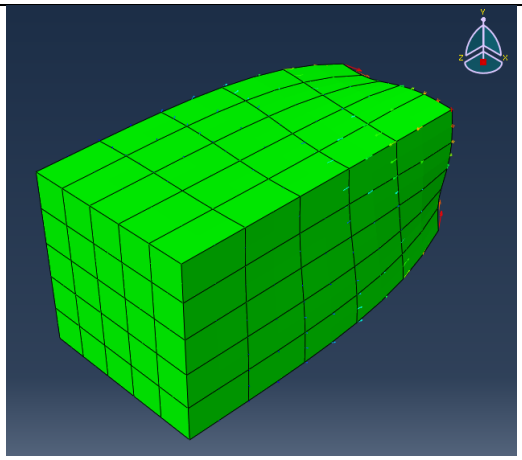
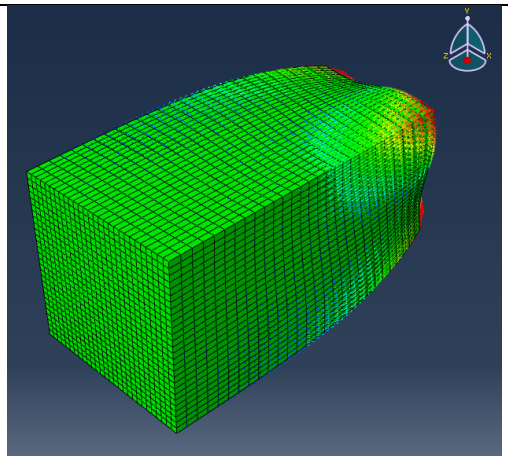
Given the convergence criteria chosen, the 125-element model can be used for further testing if it matches the mode shapes of the reference model and provides an adequate visualisation of them. As confirmed in Table 5-2, there is a good agreement between the shapes produced by either model with respect to mode shape orientation or order of appearance. Therefore, the 125-element model has been chosen as a minimum requirement for further tests.

Table 5-2: Comparison of mode shapes and frequencies for the 125 and 21952 element models

125-Element Model	21952-Element Model
	
Mode 1: 361.27Hz	Mode 1: 360.61Hz
	
Mode 2: 361.27Hz	Mode 2: 360.61Hz
	
Mode 3: 733.96Hz	Mode 3: 732.67Hz

125-Element Model	21952-Element Model
 Mode 4: 1232.9Hz	 Mode 4: 1232.2Hz
 Mode 5: 1344.9Hz	 Mode 5: 1341.1Hz
 Mode 6: 1344.9Hz	 Mode 6: 1341.1Hz

125-Element Model	21952-Element Model
	
Mode 7: 2198.6Hz	Mode 7: 2192.7Hz
	
Mode 8: 2802.5Hz	Mode 8: 2786.4Hz
	
Mode 9: 2802.5Hz	Mode 9: 2796.4Hz

125-Element Model	21952-Element Model
	
Mode 10: 3149.0Hz	Mode 10: 3149.9Hz

5.2.3.2 Effects of Aspect Ratio and Element Type

The aspect ratio in the context of a mesh convergence study is the ratio of length, width, and height of an element within the mesh. Given that the mesh created for the geometry is uniform, all elements have the same aspect ratio that is determined by the number of seeds on adjacent edges.

To investigate the effect of the aspect ratio on the modal results, an 8000-element model is tested with both aspect ratios. One model is meshed with 8000 rectangular elements with 20 seeds per edge and another model is meshed with 8192 cubical elements with 16 seeds on the short sides and 32 on the long side. The difference in number of elements is small enough such that the results, if changed, will be because of aspect ratios and not the number of elements. It was found that the highest percentage difference between those models was 0.0025% for the first 2 modes and it can be concluded that the aspect ratio does not greatly influence the model for the hexahedra (hex) element type used.

The three-dimensional element types offered in the Abaqus app are the hexahedra (hex), triangular prism (wedge), and tetrahedra (tet) types. Through experience and information found in select FE engine documentation (ANSYS Inc, 2023; SIMULIA, 2006, 2019), hex elements are tried first when meshing and the other elements are used only when irregular or curved shapes are present in the model. Given that the specimens are modelled as cuboids, hex elements are used. So far, a quadratic, reduced integration element (C3D20R) has been used in the model as such is the default mesh configuration. Other possibilities are the linear (C3D8) and reduced integration (designated by R) options. To investigate their effects, all 4 options are compared for any differences in eigenfrequencies in Table 5-3 using the model previously compared for aspect ratio. While all the tests took less than 4s each, there is a notable difference in eigenfrequencies produced by the C3D8 group of elements, especially for C3D8R which completely failed. Given that the quadratic elements are similar in computing power, the default C3D20R element is kept as it is the most similar to the reference test of 21952 elements.

Table 5-3: Comparison of Hex element types against EF results

Shape #	**Element Type**			
	C3D8	**C3D8R**	**C3D20**	**C3D20R**
1	365.11	351.233	361.532	361.265
2	365.11	351.233	361.532	361.265
3	716.207	489.277	734.477	733.964
4	1228.59	489.277	1233.25	1232.9
5	1332.14	489.277	1346.01	1344.86
6	1332.14	489.277	1346.01	1344.86
7	2079.29	489.277	2201.11	2198.65
8	2680.44	644.134	2806.24	2802.54
9	2680.44	644.134	2806.24	2802.54

Shape #	Element Type			
	C3D8	C3D8R	C3D20	C3D20R
10	2888.46	693.464	3153.51	3149.04

5.3 Investigation of MOE on Eigenfrequencies

The final step in this preliminary study is the investigation of the effect of varying MOE of the modelled block on the EF vector obtained. A series of linear perturbations were carried on a 125 element with varying MOEs between 10 to 50 GPa in increments of 5 GPa. The resulting EF vectors for each iteration were retrieved. Figure 5-1 shows the variation of EF with respect to the range of investigated MOEs. Table 5-4 shows the EF vectors per iteration for the first 10 modes as the first 10 rows, and the following two rows are the percentage difference between the current and the next eigen frequency, N_{ext} adjacent to the right, and $\Delta_{Next}(\%)$, followed by the percentage difference between the current column to the MOE of 50 GPa column. These values are valid for every frequency as every frequency from a given column has the same percentage difference from its counterpart in the adjacent column.

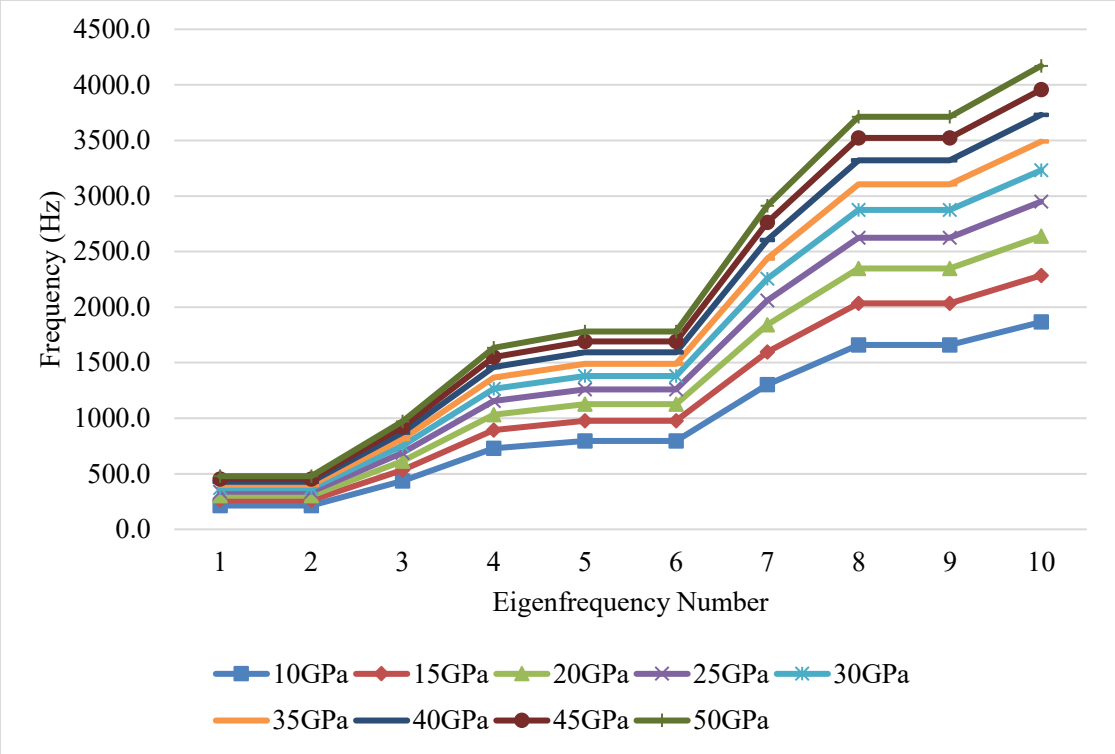


Figure 5-1: Variation of EF with different MOE

Table 5-4: Tabulated values of differences in EF with changing MOEs

	MOE of Model								
Shape #	10GPa	15GPa	20GPa	25GPa	30GPa	35GPa	40GPa	45GPa	50GPa
1	214.0	262.1	302.6	338.4	370.7	400.3	428.0	454.0	478.5
2	214.0	262.1	302.6	338.4	370.7	400.3	428.0	454.0	478.5
3	434.8	532.5	614.8	687.4	753.0	813.4	869.5	922.3	972.2
4	730.3	894.4	1032.8	1154.7	1264.9	1366.3	1460.6	1549.2	1633.0
5	796.6	975.7	1126.6	1259.6	1379.8	1490.4	1593.3	1689.9	1781.3
6	796.6	975.7	1126.6	1259.6	1379.8	1490.4	1593.3	1689.9	1781.3
7	1302.4	1595.1	1841.8	2059.2	2255.8	2436.5	2604.7	2762.7	2912.2
8	1660.1	2033.2	2347.7	2624.8	2875.3	3105.7	3320.2	3521.6	3712.1
9	1660.1	2033.2	2347.7	2624.8	2875.3	3105.7	3320.2	3521.6	3712.1
10	1865.3	2284.6	2638.0	2949.4	3230.9	3489.7	3730.7	3957.0	4171.0
Δ_{Next}(%)	18.4	13.4	10.6	8.7	7.4	6.5	5.7	5.1	-
Δ_{Abs50}(%)	55.3	45.2	36.8	29.3	22.5	16.3	10.6	5.1	-

The goal of this exercise was to investigate the range of EF expected during testing, as used in Chapter 3 and 4. The nature of the variation of EF vectors with respect to changing MOEs is more relevant in the model updating sections to follow. The relationship between MOE and eigenfrequency is a monotonic increase across the entire MOE range and across all ten modes: higher MOE produces higher eigenfrequencies, with a growing apparent gap at higher modes. This phenomenon is quite intuitive if the beam fundamental frequency formula (Blevins, 1979) is used as reference indicating that the MOE is proportionally related to the fundamental frequency.

The apparent fan out indicated in Figure 5-1 is a magnitude effect and the actual difference between eigenfrequencies at higher MOE iterations, as indicated by Table 5-4, decreases as higher MOEs are used. The range of MOEs to be used in model updating requires practical experience more so than numerical validation, since the specimens cannot be tested nor is the dataset obtained from experimentation complete.

5.4 Conclusions of Preliminary Studies

The preliminary FE analyses established the base model to be used, manages the expectations for the experimental studies and provides a guide range in the model updating step. The latter being crucial in building self guided reference checks in the sense of what is an acceptable range, in the absence of physical (destructive) test data. The model carried forward to be updated is a 3D solid extrusion of varying MOE, a Poisson's ratio of 0.2, a pinned bottom (short) face boundary condition (B.C.) and the minimum mesh density of 125 elements, with 1000 elements or more preferred for visualisation. The aspect ratio was found to be not a concern in contrast to the element

formulation for which C3D8R is to be avoided and C3D20R employed for computational efficiency. Higher MOEs were found to generate higher magnitudes of eigenfrequency vectors. It can therefore be inferred that ASR-induced stiffness losses should manifest as reduced natural frequencies.

5.5 The Finite Element Model Updating (FEMU) Process- Introduction

The FEMU process developed herein is built from the commercially available FE suite from Dassault Systèmes in the form of the Abaqus- Isight pair, and follows the patterns surveyed in Section 2.6. the Hypermesh pre-processing software was also investigated and was found to be equally adequate. Isight was preferred since complex mesh updating operations were not needed. The premise of the process is the iterative updating of the input parameters of an FE model, the MOE in this case, to obtain relevant outputs. For this study, the main outputs considered is the set of eigenfrequencies. Should the test data have yielded a more robust set of modal information, the mode shapes could have also been requested from the FE engine for MAC validation.

The implementation uses two Isight components: an optimisation component that holds the optimiser, the parameter mappings, and the convergence criteria, and an Abaqus component that holds the FE model file. Within each iteration of the optimiser, Isight passes parameter values to Abaqus, Abaqus runs the linear-perturbation analysis at those values, and the resulting eigenfrequencies are passed back to Isight for objective-function evaluation. The main interface used in Isight, shown in Figure 5-2 demonstrates the Isight modelling implementation. The objective function is the root-mean-square frequency residual, defined later in this section (equations 5-1 through 5-3).

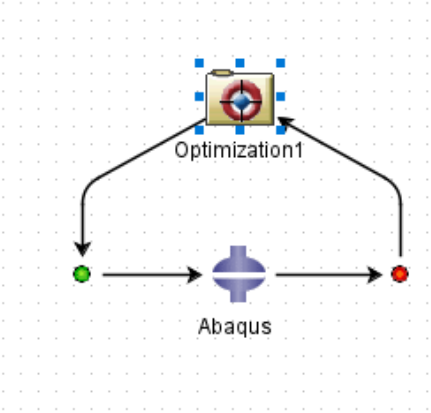


Figure 5-2: Overview of Isight components.

Post-processing of the optimisation results was performed in Microsoft Excel and MATLAB outside of Isight. This pipeline was workable for the present exploration but is the source of most of the analyst time spent on the FEMU step; Section 6.3 recommends a future MATLAB-integrated workflow that would compress the analyst time by approximately an order of magnitude relative to the present setup.

The goal of this chapter is to investigate whether the finite element model produces at the start of this chapter can be updated to predict the deterioration of the concrete (specimens) through means of updating its MOE by correlating experimental natural frequencies with the modelled eigenfrequencies. In doing so, two levels of models were produced and their results compared to choose the best one for this framework. The model levels are as follows:

- Level 1: a model using a single MOE.
- Level 2: a model made with 2 MOE regions arranged in a skin enveloping a core of the specimen. The combination of MOEs is found through algorithmic optimisation to match the experimental natural frequencies.

This level of model is further sub-divided into level 2.1 whereby the core and enveloping skin are distributed in a 50-50 ratio; level 2.2 whereby the core and skin have varying thicknesses; and level 2.3 where the skin does not envelope the core but instead is made to be on top of a bottom primary partition.

Section 5.6 describes the search for a suitable optimiser algorithm that was used in the optimiser Isight component while Section 5.7 describes the models used in more detail. Section 5.8 describes how the FEMU process was implemented through the use of the optimiser and the results are shown in Section 5.9

5.6 Finding a Suitable Algorithm

Three convergence-related Isight optimisers were shortlisted for the present work, plus the Target Solver process component as a non-optimiser, direct approach baseline. The four candidates are summarised below.

The Large-Scale Generalised Reduced Gradient algorithm (LSGRG) is a direct numerical method built on a reduced-gradient implementation. At each iteration the algorithm steps in the direction of steepest decrease of the residual; convergence is rapid when the local landscape of the objective function is well-behaved, but the algorithm is vulnerable to local-optima entrapment. LSGRG is suitable for non-linear, continuous design spaces, which describes the present problem.

The Evolutionary Optimisation algorithm (EVOL) is a self-adaptive, mutation-based algorithm. It maintains a population of candidate solutions, applies probabilistic operators that resemble biological mutation to the population at each generation, and selects survivors against the residual. EVOL is suitable for non-linear, possibly

discontinuous spaces and is less prone to local-optima entrapment than gradient methods, at the cost of substantially more iterations to converge.

Pointer is a combination algorithm that switches between strategies, numerical and exploratory, based on a runtime assessment of the structure of the problem. Pointer first explores the parameter space broadly to identify candidate regions of low residual, then refines locally using a gradient-like step. Pointer is suitable when the structure of the problem is not known in advance, which is the case for the FEMU problem at this specimen scale.

Target Solver, in contrast to the three optimisers above, is a process component restricted to constant input value modifications until either an acceptable result or the number of specified iterations has been reached. It has no concept of local-optima exploration and cannot handle multi-parameter or multi-target problems. It is included in the comparison as a baseline rather than as a serious candidate.

The chosen algorithms were tested on a level 2 model of a specimen optimised against two targets, natural frequency NF1 of 288 Hz, and NF5 of 1080 Hz. This pair of natural frequencies were taken directly from the EFDD estimator of block A Basketball without any averaging across estimators. The fifth frequency was taken in a best approximation based on mode shapes. The algorithms were evaluated according to execution speed, result accuracy and result precision. The speed tested is the total time for the algorithm to converge to a set of solutions. The result accuracy is hereby defined having the least error with respect to the specified input targets (288 and 1080 Hz). Error was quantified using two methods, the percentage difference, as it is the most intuitive,

and the Bishop's error metric (Bishop, 2021). The equations of the functions, as applied, are presented in the next set of equations, followed by application notes.

$$\%\Delta = \sum_{n=1}^{N} \left| \left\{ \frac{t_n - f(x_n, w)}{t_n} \right\} \right| * 100 \tag{5-1}$$

$$E_w = \frac{1}{2} \sum_{n=1}^{N} \{ f(x_n, w) - t_n \}^2 \tag{5-2}$$

$$E_{rms} = \sqrt{\frac{2E_w}{N}} \tag{5-3}$$

Where t_n is the target value being optimised to. N is the total number of points. $f(x_n,w)$ is the value of the function at point x_n and with function coefficients, vector w. the vector w has been included to be consistent with the source for Equations (5-2) and (5-3). Equation (5-1) is a basic formulation of the percentage difference between two numbers. However, to accommodate uneven (±) differences across function and target values, the absolute value (magnitude) of the difference is taken across function points. The target value is set to be the denominator across all iterations and runs.

Equation (5-2) is the sum of squares of errors between the function values and target values. Equation (5-3) is the root mean square (rms) of the error function and is chosen for comparing functions with different numbers of targets. Using the rms value of the error function gives a standardised error quantifier across varied sizes of data comparison in addition to being on the same relative scale as the target value, with its

units. The E_{rms} has been used throughout as only one input natural frequency is considered.

The precision of the results is defined for this study as the placement of the result found within the globality of the MOE range. Figure 5-3 shows the behaviour of the algorithms on the block A level 2 model on the skin MOE. The vertical lines are colour coded to the specific algorithms and show the best result. The globality of the MOE range explored is best demonstrated by the Pointer and EVOL algorithms which continue to throw estimates within the MOE range even after an acceptable result is found. This ensures that local optimas are not selected at the expense of increased execution times.



Figure 5-3: Variation of algorithm performance for block A level 2 skin MOE optimisation

The result of this weeding test all rested on the behaviour demonstrated in Figure 5-3. Pointer and EVOL took the most time for completion at 60 and 33 minutes each while Target solver and LSGRG took 15 and 23 minutes. The range explored, in descending order were the EVOL, Pointer, LSGRG and the Target Solver algorithms. The E_{rms} errors for the algorithms in order were 1.4, 1.9, 24.2 and 1.4 respectively.

The choice made was to use the Pointer followed by the LSGRG algorithms back-to-back to combine the globality of the search range of Pointer with the local refinement of LSGRG. Demerits for EVOL and Target Solver were the extended compute time and complex parameter inputs, and the high error of results respectively.

5.7 FE Models

This section presents the models in more detail and provides an explanation for their use. The models are sectioned in terms of the number of MOEs they use, as explained at the start of the chapter.

5.7.1 Level 1: Single MOE Model

The Level 1 model, shown in Figure 5-4, is a single-material block of dimensions 380 by 380 by 710 mm (15 by 15 by 28”), modelled as homogeneous and isotropic with a single MOE that the FEMU step iteratively modifies. The boundary condition is pinned on one short face. The density is 2 350 kilograms per cubic metre; the Poisson's ratio is 0.2; the mesh is 1 000 C3D20R elements via edge seeding.

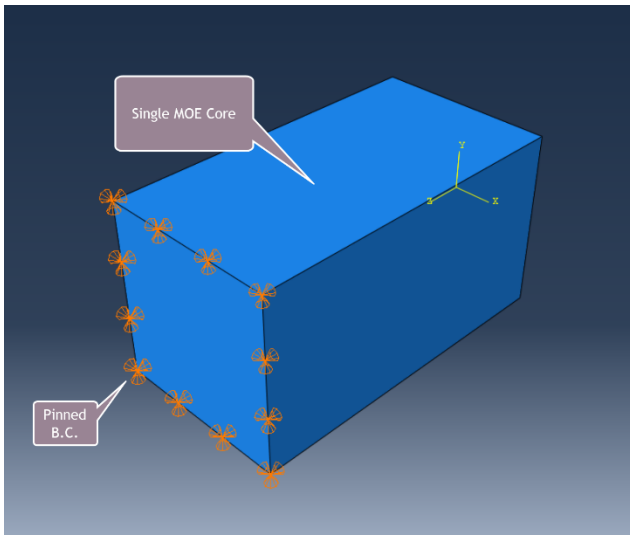
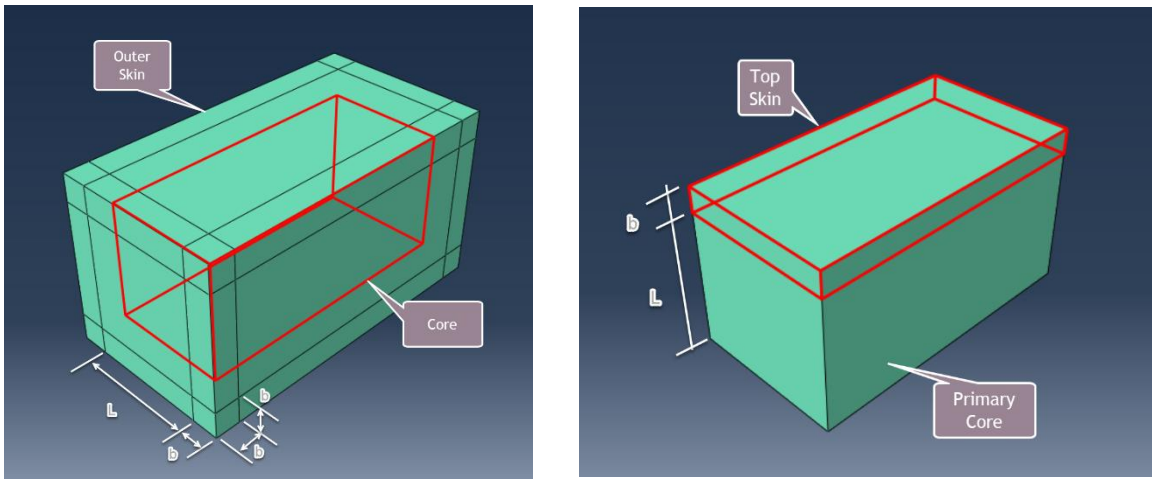


Figure 5-4: Level 1 Single MOE model with boundary conditions shown

5.7.2 Level 2: Skin vs Core Model

The level 2 model partitions the specimen from level 1 into a skin (envelope) region and a core (interior), each with a separate MOE. This partitioning is based on the reasoning derived from ASR literature surveys, that there exists a moisture gradient from the exterior to the core of a concrete specimen which causes a differential ASR reaction since ASR requires a threshold of about 80% relative humidity to occur. The differentiation of the skin and core is made to emulate such a behaviour onto the specimens tested. Two variants of the Level-2 model are considered: a symmetric variant in which the skin surrounds a centred core shown in Figure 5-5 (a), and an asymmetric variant, shown in Figure 5-5 (b), in which only the top surface (the surface with the most direct moisture exposure during the specimens' service life) carries a skin layer.



(a) (b)

Figure 5-5: Level 2 models. symmetric variant (a). Asymmetric variant (b).

The dimensions b and L are the skin thickness and core thickness respectively and are varied according to the skin thickness required. Arbitrarily chosen skin thicknesses of 10, 30, and 60 mm were chosen due to the lack of available data concerning skin thicknesses of ASR / Sound concrete boundaries. Three pathways of obtaining this data were used:

- Investigation of literature concerning direct moisture gradients across concrete depths.
- Investigation into literature concerning carbonation in concrete.
- Investigation into freeze thaw damage in concrete.

No specific values for skin thicknesses were obtained for this use case. While carbonation in concrete does provide direct observable values through staining, moisture pattern gradients for the inference of a skin were not possible. Direct moisture gradients were not found to be measured regularly for long term concrete. The values of 10, 30 and 60 mm were based off the observed data on top of block A which had an observed cauliflower expansion (topside) effect of up to 10 mm. The other two values were added

as cross check, i.e., to investigate whether an additional depth would be present even if the physical manifestations were of lesser magnitude.

5.8 Modelling Regime

The modelling efforts are separated into three parts. Part 1 is where a reference data table for inverse lookup is created on the level 1 model, Part 2 is where a single MOE is used on the level 1 model based on the first natural frequency. Parts 1 and 2 of the modelling regimes were meant to be cross comparison of a direct approach as embodied by the data table, against the iterative method of optimisation. Part 3 modelling is where multiple natural frequencies (up to NF 4) were attempted to be mapped to all models in an attempt to use the modelling as an additional placement and validation step to correct the mismatched modes from vibration testing.

5.8.1 Part 1: Data Table Approach

The first and simplest of the modelling approaches is a direct frequency matching technique. The Level 1 single-material model is run with MOE swept in 0.5-gigapascal increments from 10 to 40 gigapascal (61 iterations), and the resulting eigenfrequency set for each MOE value is collected into a data table. The measured natural frequency for a given block is then located in the table, with MOE – frequency values interpolated if needed, and the corresponding MOE value is read off as the recovered modelled value. The full table is included in Appendix C.

The choice of having the MOE increment at 0.5GPa intervals comes from the sensitivity of the back calculation of the compressive strength as compared to the resolution of the frequencies. A Δ 1MPa in fc' produces a Δ 0.383GPa in MOE whereas

a Δ 1GPa in MOE produces a Δ 2.3MPa in fc'. A Δ 1GPa produces a Δ 10Hz in frequency. Therefore, as user choice, a Δ 5Hz in frequency seems to be more agreeable since a detection algorithm would match the frequency within the closest 5Hz leading to a Δ 0.5GPa iteration change in MOE and consequently an approximately Δ 0.9MPa fc'.

End MOE results for reactive and non-reactive blocks are provided in Table 5-5 and Table 5-6. For each NF, an MOE value was taken from the data table from the closest EF. For example, block A's first NF is 285 Hz, and was compared to the first row of the modelling results table. The closest EF is 283 on run 19, therefore, its MOE value is 17.75 GPa when interpolated. The MOE values highlighted in yellow were derived from interpolation since the NF values exceeded those within the 10 to 40 GPa range. They are also presented in 0.5 GPa increments for consistency with the modelling results. The result from this modelling effort is that NF measured past mode 2 are unreliable given their unrealistic MOE values. Even if expected MOE values are obtained in higher modes, they cannot be used because of the error that mode 3 modes disrupted the order that they appear. Consequently, the modes past mode three have a great uncertainty concerning their order number and cannot be used.

Table 5-5: Part 1 Modelling results, reactive blocks

Block	A	MOE	AN	MOE	F	MOE	R	MOE
Mode 1	285	17.75	231	11.50	191	7.50	271	16.00
Mode 2					216	10.50	296	19.25
Mode 3	1082	59	1172	67.5	1058	57	1147	65
Mode 4	Axial Mode							
Mode 5	1113	19.5	1295	26.5	1172	22	1163	21.5
Mode 6	1186	22.5					1178	22
Mode 7	2032	24.5	1737	18	1933	22	1852	20.5
Mode 8			2054	15.5			2109	16.5
Mode 9								
Mode 10	Axial Mode							

Table 5-6: Part 1 modelling results, non-reactive blocks

Block	AA	MOE	AC	MOE	AB	MOE	AS	MOE
Mode 1	309	21.00	268	15.75	246	13.25	342	25.5
Mode 2	329	23.5			266	15.5	372	30.5
Mode 3	1500	97	1548	101	1549	101	1638	109
Mode 4	Axial Mode							
Mode 5	1567	39	1689	45	1768	49	1837	52
Mode 6	1636	42	1721	46.5			1860	53
Mode 7								
Mode 8								
Mode 9								
Mode 10	Axial Mode							

5.8.2 Part 2: 1 MOE – 1 NF optimisation

The Part 2 modelling operates with the same model from Part 1 but instead of blindly looping MOE input parameters to obtain eigenfrequency vectors, the first natural frequency is used as input, to obtain the MOE as output. The optimisation runs the Pointer – LSGRG pair with 30 minutes of time for Pointer and 50 maximum iterations for LSGRG. The latter did not perform more than three iterations per any given block,

indicating that the Pointer pass landed on an optimum point with a high probability of being a global one. Table 5-7 tabulates the results of this modelling section, along with the objective function and the E_{rms} values. The objective function is Isight's own error metric. The objective function was found to correlate well with the calculated E_{rms} error metric but the later was more well understood given that Isight's error formulation is not explicitly stated. The E_{rms} metric is therefore valid for use.

Table 5-7: Part 2 modelling results

Block	MOE (GPa)	Obj. function	E_{rms}
A	17.80	0.00	0
AA	17.72	24	24.7
AB	13.21	0.30	0.47
AC	15.72	0.09	0.2
AN	11.70	0.01	0
AS	25.63	0.01	0
F	7.99	0.02	0
R	16.10	0.00	0

The Part 2 results agree with Part 1's to within 1 GPa with the exception of block AA where the MOE value for that block is 3.28 GPa lower in Part 2 MOE results.

5.8.3 Part 3: Detailed Simulation Approach

In this section, the NF-EF pairings are made incrementally on all model levels, up to the fourth NF to investigate whether the natural frequency order can be reinstated using model updating or framed differently; whether the higher order natural frequencies could be verified. The types of models differ through symmetry to investigate whether the placement of an MOE differential zone affects the EF set and would produce better

correlation. Due to the number of tasks to be submitted to Isight, the modelling and iteration times were halved from those used in Part 2.

The models used are as follows:

- 1 MOE model- Level 1 model
- 2 MOE models – Level 2 model
    - Symmetric, core surrounded by varying small skin thickness.
        - 10mm skin
        - 30mm skin
        - 60mm skin
    - Asymmetric, only a top layer of skin is added to the model.
        - 10mm skin
        - 30mm skin
        - 60mm skin

The frequencies to be mapped are taken from Chapter 4 and fed for the iterations on a per number of mapped frequencies basis. For example, block A has its modes 1,3,5,6 as 285, 1082, 1113, and 1186 Hz. For the iteration EF1, mode 1 is mapped on the FE model. For iteration EF 1-2-3-4, the FE model's modes 1, 3, 5, and 6 are mapped as per the natural frequencies. Each model is assigned a combination of two MOE, chosen arbitrarily as 10 GPa for the skin and 20 GPa for the core.

Compared to Part 1 and 2 modelling, the third part produced MOE results for 6 more models in addition to 3 more NF-EF mode pairings. While the results for the Part 1 and 2 modelling efforts are straightforward, Part 3 modelling results need to be cleared, specifically in terms of which model MOE are to be used and for which block. This done firstly by evaluating the pairings to answer whether such models can correct the ambiguity of the test data, and secondly by evaluating the models.

The evaluation of the frequency pairings was done using an E_{rms} heatmap of all models and pairings, quickly indicating than all pairings past the second one are highly erroneous and are to be discarded. This is shown as the high error bands (red regions) in

Figure 5-6 for any of the mode pairs past EF 1-2. A few other observations can be made on the heatmap whereby the 1 MOE model tested has lower overall errors, the magnitude difference between the first and last two frequency pairs are in the order of 10 times larger, and the second frequency pair errors are generally twice as big as for the first pair. While the last statement is not overly general, it is especially apparent for blocks A, AN, F, and AA, with those for block AC having the reverse effect in observed errors.

The evaluation of the models is presented in Figure 5-7 graphically. The unexpected outcome of its inspection is that the models are not the stronger differentiating factor in errors; the blocks themselves are. Are the error bands are spread out along rows; it indicates that some frequency pair are harder to optimise for. This in turns indicates that EF 1 and EF 1-2 pairings are not well optimised for this modelling framework.

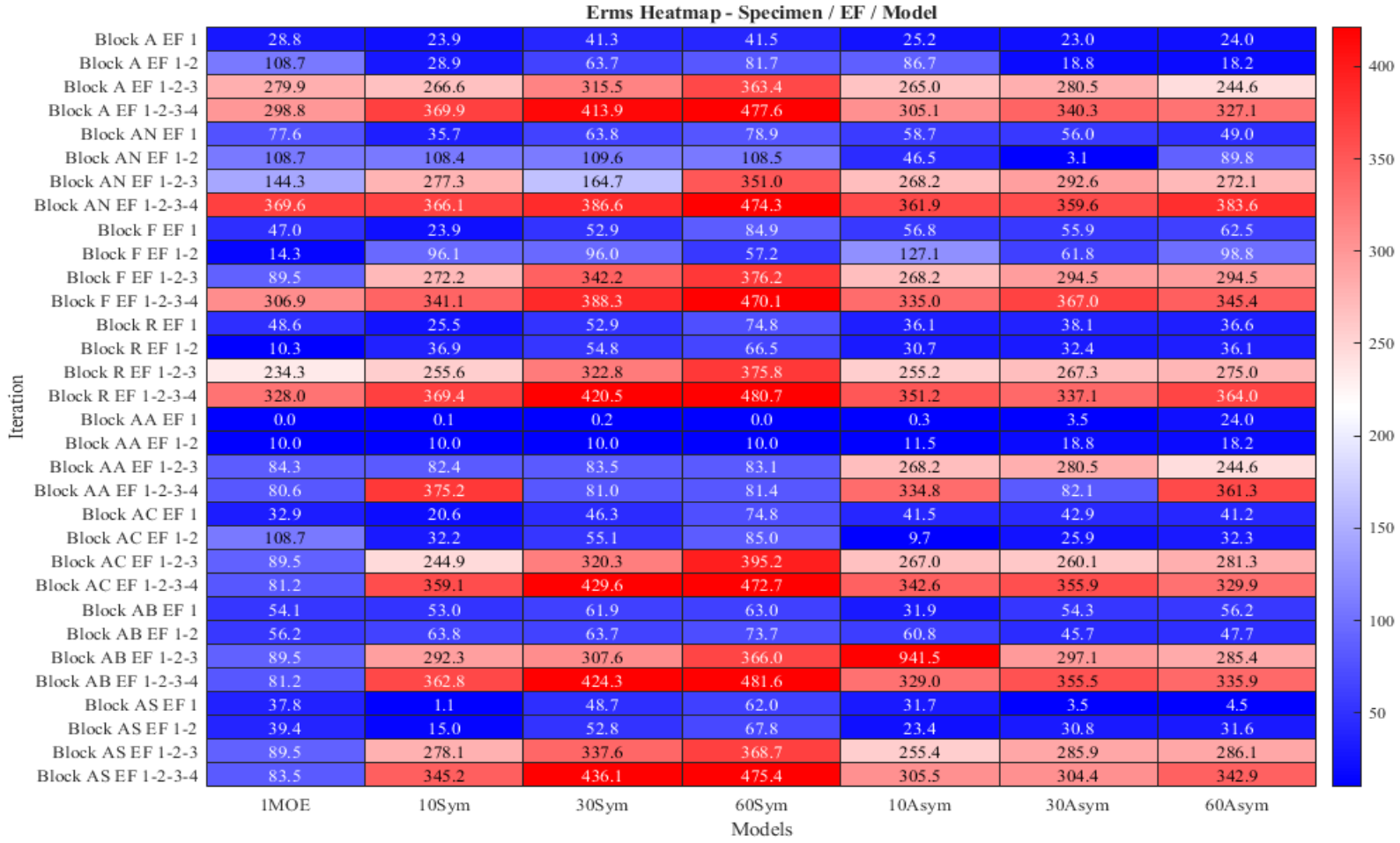


Figure 5-6: Erms Heatmap for Part 3 Modelling results

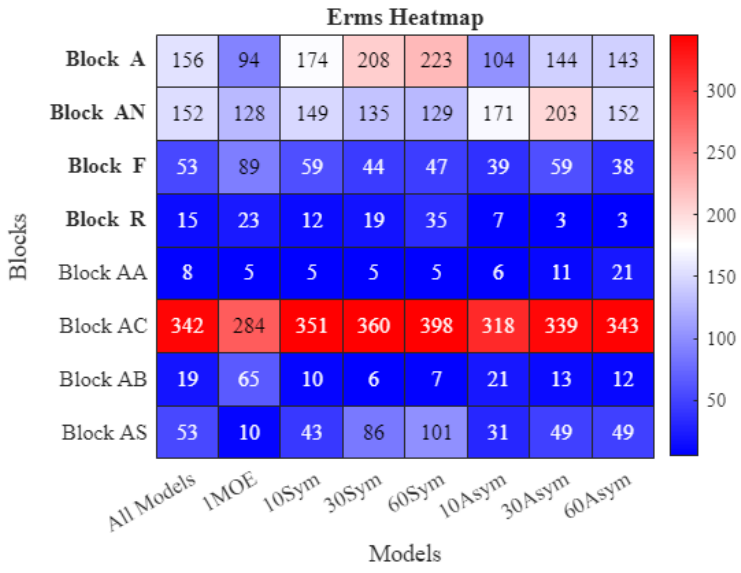


Figure 5-7: Erms heatmap for Level 3 modelling for first two mode pairs

Consequently, the results of the Part 3 modelling are presented in Table 5-8, and were obtained by taking the best fit data from any model for each block. The data is given for both 2 MOE and 1 MOE models and is arranged as follows. The first column (Spc.) lists the block name, and the 2 MOE model, error, skin and core MOEs are provided. Then the difference between the skin and core MOE is given for plausibility comparison. The last two columns provide the error and MOE values for the 1 MOE models. The reactive block names have been bolded for differentiation. Two features of Table 5-8 require comment; the relatively high error of block F, and the consistency of skin to core MOE differences across blocks.

While the data for block F was the least erroneous of all models, it is highly likely that the optimiser was trapped in a local optimum. Block F's high residual is documented here for completeness; it is not used as a basis for any quantitative claim. The difference between the 2 MOE values, for skin and core MOE, from Part 3 modelling were in the

range of -11.2 (-3.4) to -12.0 GPa for symmetric models and -11.9 to -12.8 GPa for asymmetric models. For the symmetric models, the -3.4 GPa difference has been bracketed as it seems to be an outlier on the block AA model. This suggests a weak pattern for which there is a different MOE region as proposed by the ASR gradient mechanism within concrete. However, there is no clear delineation between reactive and nonreactive blocks based on the 2 MOE results.

Table 5-8: Part 3 results: Best fit 2 MOE pairing per block

Spc	Model Chosen	Error (Hz)	MOE skin (GPa)	MOE core (GPa)	diff. (GPa)	1MOE Error (Hz)	1MOE (GPa)
A	60 mm Asym	0.0	9.4	22.2	-12.8	4.8	17.2
AN	60 mm Sym	0.9	9.4	20.6	-11.2	0.4	11.7
F	60 mm Sym	33.0	8.7	20.7	-12.0	71.0	15.0
R	30 mm Asym	0.1	10.0	22.2	-12.2	10.6	14.9
AA	60 mm Sym	0.0	20.1	23.5	-3.4	0.0	20.9
AC	60 mm Asym	0.2	7.9	19.8	-11.9	73.9	25.6
AB	60 mm Sym	0.4	11.0	21.9	-10.9	117.1	28.9
AS	10 mm Asym	1.3	13.8	26.5	-12.7	4.8	26.4

5.9 Combined Results and Discussion

The combined results of all modelling parts are presented in Table 5-9. Additional data are provided, namely the fundamental frequency, expansion strain, and rank, with rank 1 being the block with most expansion. This table forms the basis of the result comparison in this section.

Table 5-9: Combined modelling results

	A	**AN**	**F**	**R**	AC	AA	AS	AB
Natural Frequency (Hz)	285	231	191	271	268	309	342	246
Expansion (mm/mm)	0.61	0.50	0.49	0.33	0.00	-0.01	-0.02	-0.10
Expansion rank	1	2	3	4	5	6	7	8
Part 1 MOE	17.75	11.5	7.5	16	15.75	21	25.5	13.25
Part 2 MOE	17.8	11.7	7.99	16.1	15.72	17.72	25.63	13.21
Part 3 MOE								
1MOE (MOE)	17.2	11.7	15.0	14.9	25.6	20.9	26.4	28.9
Skin MOE	9.4	9.4	8.7	10	7.9	20.1	13.8	11
Core MOE	22.2	20.6	20.7	22.2	19.8	23.5	26.5	21.9

Across the 1 MOE model results on the part 1 and 2 modelling, all specimens agreed to within 1 GPa except for block AA for which the difference was 3.28 GPa. The single MOE data from the part 3 modelling agreed for blocks A and AN but diverged for the other blocks. This raises concerns for the validity of that specific modelling part.

The 1 MOE Part 1 approach seems to be the appropriate model for the data. Part 2 1 MOE models may have been chosen as well, however, as shown graphically on Figure 5-8, there is one diverging point, block AA which seems to be an optimiser error. A line of best fit has been drawn on the figure, and it is expected that Part 1 modelling would agree with it, since those results were built on an MOE increment data table. The only deduction from this is that the MOE-EF relationship is clear for the first NF. The precision of the results is in no way validated through this deduction for any of the models.

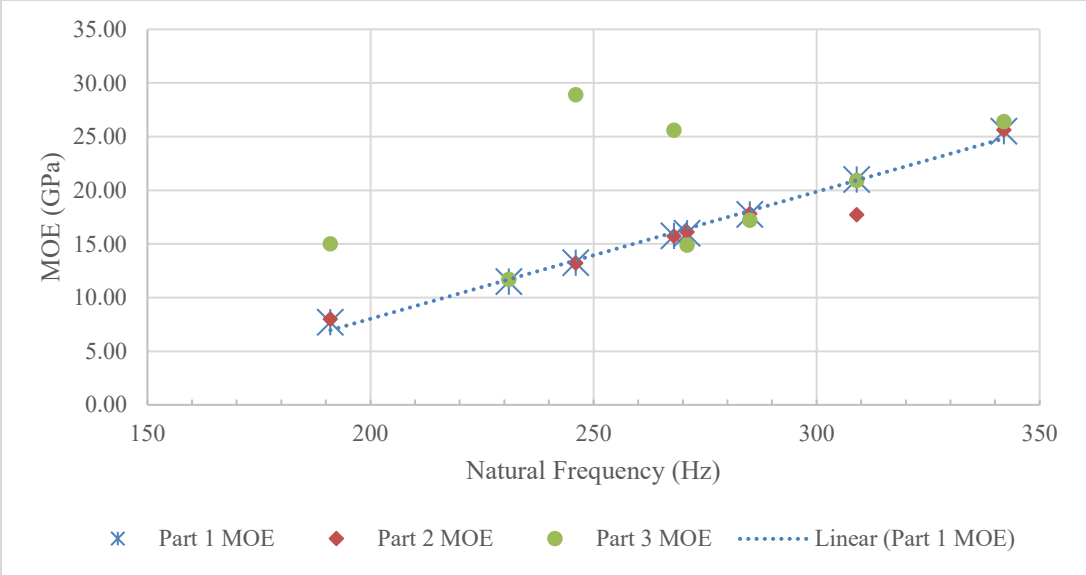


Figure 5-8: Relationship between NF and 1 MOE values from all modelling parts

Following are reasons proposed in favour of 1 MOE models as opposed to the 2 MOE models. The first argument is that the recovered MOE values for the single MOE model are physically plausible for aged normal strength concrete and are consistent with the range of values reported in literature (Ahmed et al., 2003; Giaccio et al., 2008).

A second argument is that the reactive and nonreactive groups show a directional difference, albeit a weak one. The reactive blocks of Part 1 modelling have recovered MOE values of 7.50, 11.50, 16.00, and 17.75 GPa with a group mean of 13.2 GPa while the nonreactive blocks have recovered values of 13.25, 15.75, 21.00, and 25.5 GPa giving a group mean of 18.88 GPa. The range of MOE values between the two groups overlap, with block AB, a nonreactive block of 13.25 GPa falling in the reactive MOE range, and blocks R and AC falling within 0.25 GPa of each other while they are reactive and nonreactive respectively. It can therefore be inferred that the weak correlation is either due to the small sample size, optimiser errors or mix design artefacts. The fact that MOE

does not correlate to ASR might be pushed forward but this study does not make this claim.

Thirdly, the 2 MOE model results do not show any directional difference. The skin to core differences vary between -10.9 to -12.8 GPa except for block AA at -3.4 GPa. The mean skin MOEs for the reactive and nonreactive are 9.38 and 13.2 GPa while the mean core MOEs are 21.43 and 22.93 GPa. While the 4 GPa difference in skin MOE might hint as a delineation, the 1.5 GPa core MOE difference is too weak to draw a conclusion. Combined with an irregular 1 MOE result set from Part 3 modelling, the entire part is disregarded.

The simplest model from Part 1 is therefore the most appropriate model when the dataset is limited for FE engine input. The simplest model maps the single reliable target NF1 to a single output MOE through a fully determined one to one relationship. There is no entrapment issue on this data table since there is no optimisation. As more reliable measured natural frequencies become available, through the experimental improvements proposed in Section 6, the level 2 and level 3 models become physically meaningful, since the inverse problem becomes appropriately constrained. With the present data, however, the Part 1 with level 1 model is the only level at which the inversion is well-posed. The primary limitation to this section is that the models could not be tested, therefore, these MOE values are non verifiable.

The concise result of this chapter was the provision of a set of MOE values for each block. They are presented in Table 5-10 and are arranged in descending order with respect to expansion with the reactive blocks bolded. The fist NF is provided from Chapter 4, and the MOE values recovered from the Part 1 modelling works in the

previous sections are provided in the last column. As mentioned in the previous section, there is no direct correlation between MOE and expansion strain, i.e., there is no demonstration that the recovered MOE values are indicative of ASR damage. Figure 5-9 shows the first measured frequency plotted against strain on the primary axis, while the recovered MOE from the Part 1 modelling plotted against strain on the secondary axis. The linear mapping between the input NF1 and resulting MOE is evident from both plotted series while the intersection of reactive compared to nonreactive specimens on both frequency and MOE is shown.

Table 5-10: MOE result table with strain and EF1 data

Block	Aggregate	Cement	Alkali Content (%)	Strain (mm/mm)	F1(Hz)	MOE (GPa)
A	Mactaquac Greywacke	Brookfield	0.91	0.610	285	17.75
AN	Springhill #3 quarry	Dragon	1.25	0.498	231	11.50
F	Springhill #3 quarry	Brookfield	0.91	0.493	191	7.50
R	Springhill #3 quarry	Brookfield	1.25	0.329	271	16.00
AC	Springhill #3 quarry	Mix	0.62	-0.002	268	15.75
AA	Springhill #3 quarry	Mix	0.75	-0.014	309	21.00
AS	Springhill #3 quarry	St. Mary's	0.50	-0.022	342	25.50
AB	Springhill #3 quarry	Mix	0.50	-0.102	246	13.25

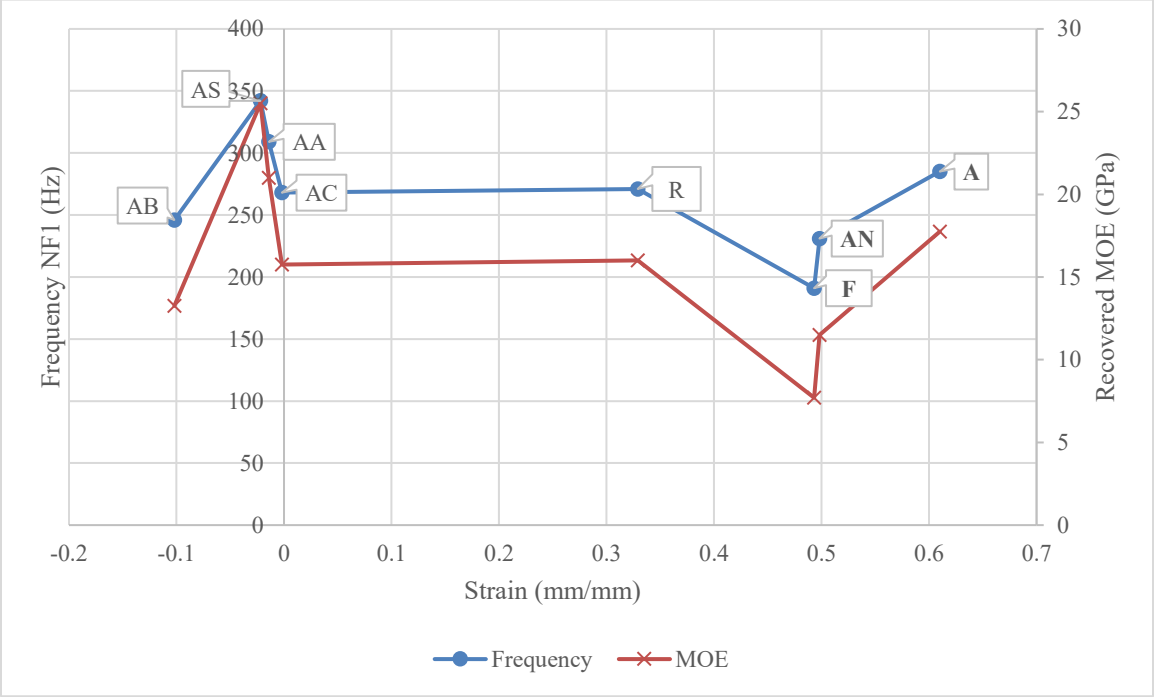


Figure 5-9: NF1 - MOE to strain map

5.10 Discussion

5.10.1 Models

In the process to find a proper model and optimisation process to correlate measured first frequencies to MOE, single and double MOE models were used. The two MOE model were used to correlate ASR gradient progression within concrete to the FE model. Multi MOE models such as the one shown in Figure 5-10 were also considered for this study. It shows an FE model partitioned in such a way along its sides that 27 MOE regions would be created within the solid which would be available for the solver to change the MOE values. The length, width and depth of the model, labelled as L W and H, were intended to be parametrised and changed by the solver as well. This model

could not be realistically used with the current experimental dataset as for a number of outputs far greater than the number of inputs, the results would be implausible, due to the problem being under constraint, on top of being unverifiable. However, this model is the logical next step for higher order model (towards mesoscale modelling) once better experimental data in the form of longer NF vectors and mode shapes are obtained. The challenge therein would be to tune the model with respect to the number of partitions to compromise between model complexity, result accuracy and run times, as noted in the literature survey.

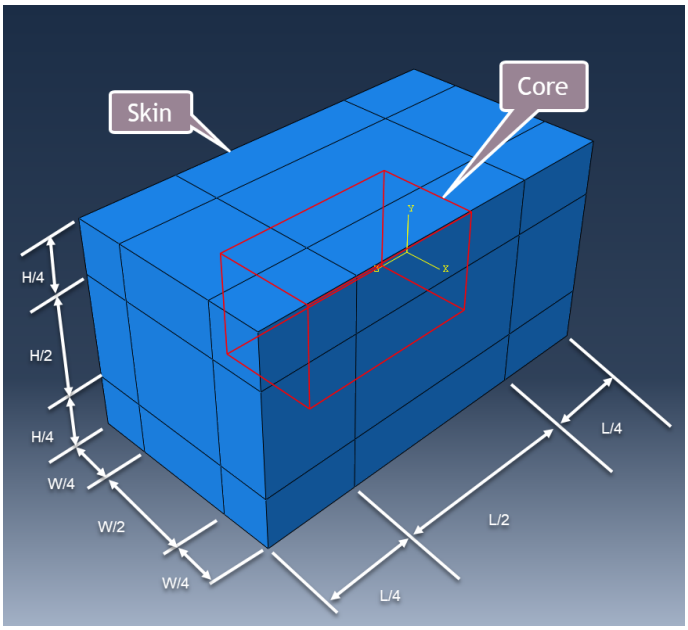


Figure 5-10: Multi MOE model

The use of this type of model would have allowed the proper usage of Part 3 modelling whereby the NF vectors could be paired for more than one pairing (EF to NF), thereby cross validating out of order modes. However, the limitation remains in the lack of material test capability to verify the MOE results.

5.10.2 What the FEMU Step Contributes

The raw frequency comparison in Section 4.5 with an R^2 of 0.226 against expansion strains, shows a weak delineation between reactive and nonreactive specimens. Moreover, the small sample size does not have enough of a statistical ability for any claim. The FEMU step does not change the modal ranks of the measured frequencies since the data table approach or the other FE models are a linear transformation of NF1 to MOE. It therefore cannot improve reactivity classification for the population beyond what the frequencies already show. This is clearly demonstrated in Figure 5-9 whereby the MOE recovered is directly related to NF1.

What the FEMU step offers is a change of property. It converts a measured quantity, the first frequency of the specimen, which is dependant on the sample dimensions, material and boundary properties, into a concrete property value, the MOE. The latter can then be compared directly as a function of time, or as a proxy of ASR progression, should the actual block MOE be obtained and the values presented in this chapter be confirmed; the confirmatory tests being crucial to this framework, but not possible.

The broader value of this FEMU step at this scale is not in the specimen population claim of determining reactive against nonreactive specimens. Even if such a defensible claim was proved, it would have been voided because of the small specimen population. This study, upon material test verification, will provide a framework for the MOE of concrete specimens, without having to go through the lengthy constraints of

ASTM C215, which places limits on specimen size and excitation characteristics as the dynamic modulus obtained is based of empirical formulae.

The thesis demonstrates a reproducible, documented procedure for converting a measured first natural frequency into a recovered effective stiffness, which becomes fully meaningful the moment a baseline measurement at casting is available for comparison against subsequent measurements. That is the comparative-monitoring-framework contribution that the thesis defends, and it is the contribution that motivates the road map for future work in Chapter 6.

5.10.3 Process Recommendations

Several process recommendations are proposed as a result of the work performed in this chapter and are formalised in Section 6. First, the data table approach is the preferred method when test data yields only the first frequency. It is direct and does not suffer from optimiser errors such as entrapment nor under execution setups.

Second, the iterative Pointer – LSGRG optimiser approach is most appropriate when two or more reliable modes are available, or a Multi MOE model is justified. Under those conditions, the data table approach is less powerful since the pivot between two of more frequency may change the optimised MOE for a more representative one compared to the data table.

Third, one of the most important findings in terms of using the solver is to re-initialise the model before launch. Iterative seeding is a tuning hazard and was identified to be a source of error in the Part 3 modelling works and shown in the 1 MOE model.

Since the same model was used back-to-back for each model, the last saved MOE value was reused by the solver as initial guess which most likely poisoned the 1 MOE data.

Finally, a Matlab based pipeline is recommended. Data acquisition, processing and FE engine control is possible through Matlab, although it will take significant effort to match ARTeMIS's analysis capabilities, it would greatly shorten the analysis time which would be better spent on optimiser compute time.

5.11 Summary and Conclusion

This chapter delivered three things: an FE model, an optimisation strategy, and a set of FE recovered MOE result for each block, along with a rationale for the chosen data and limitations as to what the data means.

The FE configuration was established as a 1000 element C3D20R mesh with material properties as a 0.2 Poisson's ratio and density of 2350 kg/m^3, pinned on a short side and with hex elements. The relationship between MOE and NF was found to be monotonic, with constant difference across all values of a frequency vector between adjacent MOE columns. This FEMU framework stands on this monotonicity, without it, the MOE inversion from NF would not be possible and the FEMU recovered values would have no physical interpretation.

The reactive and nonreactive specimen show a slight delineation based on their group MOE mean, 13.2 vs 18.88 GPa respectively. However, the range of MOEs for both specimen types overlap and the sample size of 4 per group make it impossible for any statistical claim. This is further restricted by not being able to verify the recovered MOE data through specimen material testing. The study was not

designed or resourced to deliver a statistically validated population comparison; it was designed to establish whether the pipeline can be built and run at this specimen scale, and to identify the conditions under which it produces physically interpretable output. On those terms, it succeeds: the pipeline runs end to end, the recovered stiffnesses are physically plausible and directionally consistent with the known reactivity classification. The data-completeness threshold is a documented, transferable design principle for future work at this scale: one reliable natural frequency per block supports a well-conditioned single-MOE recovery, while two or more free parameters against one reliable target does not.

The two-MOE pairing returns consistent skin-to-core MOE differences in the −11 to −13 gigapascal range for seven of the eight blocks (Block AA being an outlier), but does not separate reactive from non-reactive populations, as expected for an under-constrained inverse problem. Multi-MOE (above 2 MOE) models were investigated and not pursued on the same grounds.

The conclusion from this chapter is that with the specimen material testing limitation, this process can still be verified formally if population wise ASR differentiation is not sought but instead inter specimen properties are monitored across time. In essence, with a baseline (cast time preferred) from with to compare the recovered frequencies and MOEs, multiple tests would indicate their respective changes with respect to expansion strains and therefore with respect to ASR.

The roadmap for the process extension such as the use of different equipment and or processes, built from the lessons learnt in Chapters 3 through 5 is laid in Chapter 6.

6 Study Wise Conclusions and Summary

This chapter integrates the experimental work, modal analysis, and finite element model updating presented in Chapters 3 through 5 to evaluate the feasibility of FEMU with modal data as a comparative diagnostic tool for ASR damage in concrete. The two research questions stated in Chapter 1 are revisited at the close of the chapter:

- Is modal testing able to differentiate ASR reactivity within concrete, and if so, which of operational or experimental modal analysis is better suited?
- Is finite element model updating capable of incorporating modal test results to provide a measurement of ASR degradation within concrete specimens?

The work distinguishes itself from the surveyed literature in three respects: the specimens tested are mature, with approximately nineteen years of exposure and near-complete to fully complete expansion; the modal analysis pipeline contains a direct test comparison between operational and experimental modal analysis on the same specimens; and FEMU is applied with the dynamic modulus of elasticity as an ASR damage proxy. The remainder of the chapter summarises the experimental findings, evaluates the FEMU process as implemented, sets out study-wide recommendations, identifies the limitations bounding the results, and outlines future work.

6.1 Summary of Experimental Findings

The experimental programme established that modal testing is feasible on ASR-affected concrete specimens of non-standard geometry and weight, with data quality driven primarily by test setup, instrumentation, and excitation regime. A pinned-free boundary condition was arrived at through iteration on free-free, fixed, and pinned-

pinned alternatives, and the OMA accelerometer locations were harmonised with the EMA hammer impact points to permit direct comparison between the two test routes at the node level.

Of the modal data sought, only the first natural frequency was reliably identified across the full specimen set spanning 191 hertz (Block F) to 342 hertz (Block AS). The mirror second mode was identified for five of the eight blocks (AA, AB, AS, F, and R); modes three and beyond did not survive cross-validation. OMA performed better at lower frequencies, particularly at the first mode, while EMA performed better above approximately one thousand hertz; the majority of actionable data came from OMA. A definitive ranking of OMA over EMA cannot be made on the basis of this study alone, because the EMA campaign was not conducted with the broadband shaker or sledgehammer instrumentation that would have given it a fair chance.

The relationship between the first measured natural frequency and the corresponding expansion strain returned a linear regression coefficient of determination of 0.226. The reactive group (191–285 Hz) and the non-reactive group (246–342 Hz) overlap across the 246-to-285-hertz band with four blocks in the overlap region, precluding any classification of an individual specimen on the basis of its first frequency alone.

The FE modelling work returned recovered MOE values for all eight specimens through three modelling parts. Part 1 (data-table inversion on the single-MOE Level 1 model) and Part 2 (single-MOE optimisation against the first natural frequency) agreed to within one gigapascal across all specimens except Block AA, where the Part 2 value differed from Part 1 by 3.28 GPa. Part 3, which attempted to pair multiple natural

frequencies against the FE eigenfrequencies on Level 1 and Level 2 models, returned single-MOE values that diverged from Parts 1 and 2 for most specimens. The Part 1 single-MOE recovered values are 17.75, 11.50, 7.50, and 16.00 GPa for the reactive blocks (group mean 13.2 GPa) and 15.75, 21.00, 25.50, and 13.25 GPa for the non-reactive blocks (group mean 18.88 GPa). A weak directional difference between the two groups is present; the ranges overlap and the sample size is insufficient to support statistical claims.

6.2 Evaluation of FEMU Process and Conclusions

6.2.1 The FEMU Process

The FEMU process is implemented with a linear elastic isotropic model and incorporated some meso scale considerations with the Part 3 modelling, although the results were inconclusive for those models. The Pointer – LSGRG algorithm pair was selected after a series of trials for its combined global and local search regions. The E_{rms} error metric was found to be adequate to compare models across Isight solver and loop (data table) models.

The progression from Part 1 to 3 for model updating was motivated by the need to investigate whether the measured frequency results could be rearranged via model updating EF vectors, and how Part 1 results did not match any modal frequency vectors from any blocks, leading to the use of other models. Part 1 and 2 confirmed that single MOE – NF pair optimisation produces representative MOE results but single MOE throughout the specimen was questionable, leading to the development of the 2 MOE model to better model ASR gradient through concrete. However, this hypothesis could

not be tested using available experimental data. The only reliable modal data was the first frequency as obtained rom Chapter 4. Higher modes were either missing, not observable, inconsistent with other estimator for validation, or paired with mode shapes too unreliable for confirmation. Part 3 optimised against EF1, EF1-2, EF1-2-3, and EF1-2-3-4 targets, but past EF1-2 the optimiser was matching FE eigenfrequencies to measured frequencies whose identification was uncertain. Even the EF1-2 pairing was dropped due to comparatively higher error between the latter and EF1 pairing, leaving only the NF1 pairing reliable across all modelling parts, with Part 1 model results being the chosen one.

The Isight–Excel–MATLAB data chain used in this study was functional but cumbersome and time consuming for between-app transfers. Isight was effective for setting up the model and the optimisation framework, but data handling had to be performed outside it in Microsoft Excel and MATLAB. Error calculation across vectors of changing length, comparison plots across specimens, and the integration of model outputs with measured data all proved cumbersome and were ultimately moved to MATLAB. This data-handling cost is a limitation of the chosen toolchain rather than of the FEMU process itself and motivates the integrated-pipeline recommendation that follows in Section 6.3.

6.2.2 Study Conclusions

The following conclusions are drawn from the entire exploratory study. The simplest model is the most appropriate one for this dataset. The single MOE level 1 model paired with the first measured frequency through the reference data table provides representative MOE readings for the specimens and are least prone to algorithmic errors.

Even though the Part 2 modelling approach was also reliable, it had small errors caused by the solver computation and setup constraints which led to the choice of the data table over it. The recovered Part 1 MOE values are physically plausible for aged normal-strength concrete and consistent with the range of values reported in the literature for ASR-affected mixes. The data completeness threshold made visible by this study is a documented, transferable design principle for future work at this specimen scale: one reliable natural frequency per block supports a well-conditioned single-MOE recovery, while two or more free parameters against one reliable target does not.

Modal testing at this specimen scale supports a comparative evaluation rather than a direct assessment of ASR. Direct differentiation of ASR reactivity from the first natural frequency alone is not supported by the present data ($R^2 = 0.226$ against expansion strain) and is unlikely to be achievable at field-specimen scale without a baseline measurement at the point of casting. The practical implication is that vibration-based ASR assessment in the form developed here is the longitudinal monitoring of a specimen, structure, or member against a reference state, either its own past state or a controlled reference specimen, rather than the absolute classification of a specimen based on a single measurement.

The answers to the two research questions stated in Chapter 1 and reiterated at the beginning of Chapter 6, are offered as follows.

ASR reactivity cannot be reliable differentiated between specimens based on single measurements. The data obtained was not enough to truly establish a definitive delineator between reactive and nonreactive specimens with a strong enough statistical claim, even for this small specimen size. While OMA was proven to be more reliable in

detecting modal frequencies in this experiment, EMA will not be discredited based on unfair instrumentation with respect to OMA; the available hammer was just not enough to properly excite the required bandwidth. Even for OMA, noise present, even in the isolated heavy flooring of the laboratory, was heavily detrimental to Ambient and Forced Ambient (Basketball) measurements.

As to the FE model updating process, it has been demonstrated that a simple enough model can be employed to recover MOE values based on the limited data, NF1 for each specimen. The value of MOE is however limited to a single, uniformly distributed property over the entire model. Multi MOE models were simply not able to properly reach optimised values with the limited dataset. In addressing the degradation part of the inquiry, it was found that it could be done if the study would not limit itself to one measurement per specimen, but instead use comparative tests with respect to a baseline measurement, preferably as casting time, as a datum for further tests which would then be able to be used a damage proxy for ASR progression or assessment.

The final conclusion of this study is that this type of exploratory tests cannot be performed on non-testable specimens. The confirmed FE output values, in this case, the MOE, need to be able to be tested and confirmed to ensure that the FEMU results are precise.

6.3 Recommendations

The recommendations of this study are in three aspects; the experimentation phase, the data analysis, and the model updating. They fill specific gaps that the literature

survey did not address: the absence of standardised guidance on testing procedures or comparative cross method testing, and on estimator and validating techniques.

For the experimentation, a preliminary FE analysis should be performed before instrumentation, and the measurement plan should locate accelerometers at nodes where mode shapes can be fully captured. Input energy and frequency content should be assessed for both modal-test routes: the input for OMA needs to be verified for broadband excitation and randomness, while for EMA the instruments imparting energy need to be tested to confirm they cover the full range of energies required for the modes investigated. For a more rigorous OMA - EMA comparison than this study could provide, OMA should be conducted with triaxial accelerometers paired with broadband random ambient excitation, and EMA with heavier impact sledgehammers or modal shakers paired with a roving accelerometer setup. Both methods need to be given their best instrumentation conditions to be fairly compared. For data analysis and modal identification, the use of a complete ARTeMIS suite or similar is strongly advised. The tools relied on most heavily in this project were the multiple estimators used for cross-validation of modes by frequency and the animation tool used for visualisation and validation of modes by shape; these should be available to the novice tester from the outset of any similar campaign.

For modelling and the FEMU process overall, modelling controls should be investigated as thoroughly as resources allow, including algorithm selection and optimisation method. The selection of error metrics for two plus matching should incorporate the Erms metric for its dimensional consistency with the target frequencies. Integrated modelling is highly recommended, total data management of models, inputs,

and outputs within the same software. A future implementation using a unified MATLAB pipeline through the Abaqus2Matlab interface, with GPU acceleration where applicable, would compress the analyst time by approximately an order of magnitude relative to the present setup. The Matlab (or programmatical equivalent) pipeline would cut the inter-app data transfer which was found to be the most cumbersome aspect of this research. Matlab is being recommended in this case over a pure programming language due to its robustness in instrumentation 'talk" capabilities, i.e., Matlab could very well interact with the sensors and collect data, just as ARTeMIS. This would be quite hard to implement using pure programming language.

The most consequential conclusion of this study is the adoption of comparative testing as opposed to single measurement points. The realistic application of vibration-based ASR assessment, as performed in this study, is the change in the measured concrete properties with respect to time, rather than the classification of a specimen on a snapshot measurement. It is noted that there are too many uncontrolled factors arising from the environmental exposed concrete that may affect the vibration response, and comparative studies are recommended because of those. Snapshot measurements could have be used if purpose made, controlled specimens were used instead.

6.4 Limitations

This study was bound by four main limitations. This first is the specimen population. The number of specimens tested was well below what is considered a statistically relevant population (n=30 at least). When grouped, the 8 specimens are halved which further drives down the significance of the work performed.

The second is the non-destructive constraint on the specimens which prevented the FEMU obtained MOE values from being validated. The MOE results were cross validated as best they could within the modelling parts and optimisation metrics, with analyst experience being the final check for plausible results, but in the absence of test data, the MOE values are representative and not definitive.

The third is the availability of instrumentation. The principal limitation here was the number of accelerometers, which forced a compromise of measuring two faces properly and leaving the other two faces to extrapolation in ARTeMIS through slaved-node motion. The available excitation to the specimen, either in OMA or EMA configurations in terms of input excitation quality or hammer respectively was not optimum. Consequently, mode shapes of sufficient quality for inclusion in the model-updating step were not produced, reducing the correlation data available to FEMU. Combined with the implementation restrictions of OMA and EMA on specimens of this size and weight, the number of natural frequencies reliably extracted per specimen was reduced to one. This single-NF limitation is the root cause of the Part 3 modelling failure and the multi-MOE model discard and constrains the resolution at which FEMU could be performed regardless of algorithmic choices.

The fourth is the model used. The FE model assumes a linear perfectly isotropic material. The ASR effects on concrete associated with stress fields, preferred crack direction and gel pressure has to been investigated fully on the model used though preliminary small-scale tests based on thermal loads as strain approximations yielded no changes with respect to the perturbation step results. The boundary condition modelled was the most practical of the configurations investigated and the pinned condition was

assumed to model the specimen on its face properly. There exists a small uncertainty with respect to the specimen gyrating, wobbling, or shifting based on its uneven faces, which has not been thoroughly investigated, though these effects might prove to be negligible.

6.5 Future Works

The recommended future works are presented split in short and long term endeavours. The first being performed on the presently tested specimens, and the latter being performed on purpose made specimens.

6.5.1 Immediate Follow-up Tests

The natural frequencies of the specimens should be measured again after enough time has passed for the expansion plot to register further ASR progression, which would be at the next expansion recording time. This would be especially relevant for block A which was still not fully stopped expanding at the time of tests. A change in the reactive blocks' natural frequencies, with the non-reactive blocks acting as controls, would indicate whether modal frequencies are sensitive to ongoing ASR progression on these specific specimens. Care should be taken to ensure desiccation effects do not interfere with the results. Ideally the baseline for comparative monitoring would be at zero strain, but since that point has long passed for the present blocks, the next-best option is to use the current measurements as the baseline for a comparative second round. This step alone would convert the present cross-sectional dataset into a two-point longitudinal one for each specimen. Due to the non-destructive nature of the blocks because of their long-term study, it is expected that the would be available for destructive testing as soon as the specimens stop expanding, and the mix design data is obtained from them. At that point,

it would be the most ideal time for vibration and FEMU process tests since the MOE validation could occur.

6.5.2 Second Campaign on Purpose Cast Specimens

The MOE values recovered through FEMU could not be validated against laboratory tests because the specimens could not be destructively tested. A powerful remediation would be to cast specimens specially made for MOE test data. An added benefit to having purpose cast specimens, would be that in the process of obtaining the MOE, the compressive or splitting tensile strength could also be obtained with would add further verification data points to the FEMU process.

The most important contribution to having purpose made specimens would be the ability to take measurements at various points of the S-curve of ASR expansion which would in turn provide data on the vibration property of the concrete with varying rates of ASR expansion. This would culminate in an ability to take a set of measurements of similar concrete and pinpoint as to where the ASR progression is, with respect to the S-curve of expansion. Practically, this translates in the ability to predict when the ASR expansion might slow or stop, and this is a decisive advantage in structural asset management.

Finally, the specimens are recommended to be benchtop sized rather than the 200 kg unwieldy specimens tested. Smaller specimens allow the safer investigation of free-free boundary conditions, cut down the time for instrumentation, testing and transportation, and require a much lesser footprint in laboratory. Furthermore, input excitation on both the operational and experimental side become more controlled and

require less expensive apparats in terms of shakers or hammers, with smaller specimens. The biggest advantage to small specimens for a new campaign would be when the reaction is accelerated with immersion or spraying with alkali solution such as sodium hydroxide, which is much safer when done on smaller scales.

Finally, the ASTM C215 standard could be used as an independent cross reference with such specimens. This would provide another layer of verification on the frequency measurement and the MOE value.

6.5.3 Modelling Extensions

The two modelling directions identified in Chapter 5 become accessible with a second test campaign and improved test data. The first is the multi-MOE class of models, which were discarded in the present study for non-uniqueness given the single reliable NF available.

The second is the inclusion of combined expansion effects in the FE model. The present FEMU process treats ASR expansion (via DEMEC measurements) and modal frequency as two parallel observations empirically correlated through the updated MOE. A combined model would instead use the measured expansion as an input, applied as a direct strain or a thermal induced expansion, and ask whether the resulting residual stress and geometric distortion accounts for some portion of the frequency change beyond what MOE reduction alone explains. This is a stronger physical model because it treats two manifestations of the same underlying phenomenon as coupled rather than independent. The principal data requirement is volumetric strain information, which the four-point surface DEMEC measurements of the present study cannot provide; a benchtop campaign

with internal strain instrumentation or multi-face expansion tracking would supply the necessary inputs.

6.6 Avenues of Research and Application

Three broader avenues for this type of process were identified over the course of this study. The first is the implement of the CTMR models to large scale structures complemented with vibration testing. Such models could be made to auto update themselves automatically with vibration test data (OMA outputs), rather than the manual stress-strain measurements currently used. While a comparative baseline of the newly commissioned structure would be preferred, an in-service state as baseline could be investigated.

Performance testing of concrete mixes against ASR risk is a second avenue: current test methods, even accelerated ones, are lengthy, and the comparative framework would shorten ASR risk assessment to a sequence of modal measurements over a controlled exposure period rather than a long-duration expansion measurement. The development cost of such a test would be substantial, but the principle is supported by the present work.

The third avenue is the evaluation of prefabricated concrete products such as slabs and beams, which can be compared directly against a reference sample drawn from the same production batch. Prestressed elements introduce additional complications such as concrete damage, strand debonding, and differential stress zones must be separable in the FE model, but the framework developed here is a natural starting point.

These avenues are multidisciplinary and substantial, but the methodological infrastructure established by this thesis provides the foundation from which they can be approached.

Bibliography

Ahmed, T., Burley, E., Rigden, S., & Abu-Tair, A. I. (2003). The effect of alkali silica reactivity on the mechanical properties of concrete. *Construction and Building Materials*, *17*(2), 123–144. https://doi.org/10.1016/S0950-0618(02)00009-0

ANSYS Inc. (2023). *3 Steps to Improve FEA Models*. https://www.ansys.com/blog/how-to-improve-fea

ASTM. (2018). *C1293 Standard test method for determination of length change of concrete due to alkali-silica reaction* (ASTM Standard C1293-18a). www.astm.org

ASTM. (2020). *Standard test method for determination of length change of concrete due to alkali-silica reaction* (ASTM Standard C1293-20a).

ASTM. (2021). *Standard Test for Potential Alkali Reactivity of Aggregates (Mortar-Bar Method)*.

Avitabile, P. (2014). *Modal space - Back to Basics*. University of Massachusetts Lowell. https://doi.org/10.1111/ext.12142

Barbosa, F., & Cremona, C. (2002). *Identification Modale de Structures sous Sollicitation Ambiante : Volume 1 - Théorie et Applications Identification Modale de Structures sous Sollicitation Ambiante : Volume 1 - Théorie et Applications* (Vol. 1). Laboratoire Central des Ponts et Chaussées.

Barbosa, R. A., Hansen, S. G., Hansen, K. K., Hoang, L. C., & Grelk, B. (2018). Influence of alkali-silica reaction and crack orientation on the uniaxial compressive

strength of concrete cores from slab bridges. *Construction and Building Materials*, *176*, 440–451. https://doi.org/10.1016/j.conbuildmat.2018.03.096

Batel, M. (2002). Operational modal analysis - Another way of doing modal testing. *Sound and Vibration*, *36*(8), 22–27.

Bazant, Z. P., & Steffens, A. (2000). Mathematical model for kinetics of alkali-silica reaction in concrete. *Cement and Concrete Research*, *30*(3), 419–428. https://doi.org/10.1016/S0008-8846(99)00270-7

Beaman, N. (2005). *Prevention of Expansion due to Alkali Silica Reaction in Concrete Containing Reactive Aggregates from Mactaquac*. University of New Brunswick.

Bérubé, M. A., Durand, B., Vézina, D., & Fournier, B. (2000). Alkali-aggregate reactivity in Québec (Canada). *Canadian Journal of Civil Engineering*, *27*(2), 226–245. https://doi.org/10.1139/l99-076

Bishop, C. (2021). *Pattern Recognition and Machine Learning*. Springer. http://research.microsoft.com/⁄cmbishop

Blevins, R. (1979). *Formulas for Natural Frequency and Mode Shape*. Van Nostrand Reinhold.

Brandt, A. (2011a). Multiple-input Frequency Response Measurement. In *Noise and Vibration Analysis: Signal Analysis and Experimental Procedures* (14). Wiley. http://ebookcentral.proquest.com/lib/unb/detail.action?docID=792461.

Brandt, A. (2011b). Single-input Frequency Response Measurements. In *Noise and Vibration Analysis: Signal Analysis and Experimental Procedures* (13). Wiley. http://ebookcentral.proquest.com/lib/unb/detail.action?docID=792461.

Brinker, R., & Andersen, P. (2004). *Method for Vibration Analysis.* (Patent US6, 6779404B1).

Brinker, R., & Ventura, C. E. (2015). *Introduction to Operational Modal Analysis*. Wiley.

Caetano, E., & Cunha, A. (2004). Experimental and numerical assessment of the dynamic behaviour of a stress-ribbon footbridge. *Structural Concrete*, *5*(1).

Chen, H.-P., & Ni, Y.-Q. (2018). Modal Analysis of Civil Engineering Structures. In *Structural Health Monitoring of Large Civil Engineering Structures* (Number March 2021, pp. 91–121). Wiley. https://doi.org/10.1007/978-1-4939-0767-0

Comby-Peyrot, I., Bernard, F., Bouchard, P. O., Bay, F., & Garcia-Diaz, E. (2009). Development and validation of a 3D computational tool to describe concrete behaviour at mesoscale. Application to the alkali-silica reaction. *Computational Materials Science*, *46*(4), 1163–1177. https://doi.org/10.1016/j.commatsci.2009.06.002

Covioli, J. V., & Coppotelli, G. (2019). Experimental and operational modal analysis in support of modal model updating - A test case. *8th IOMAC - International Operational Modal Analysis Conference, Proceedings*, (October), 283–293.

CSA. (2005). *A864-00 R2005*. CSA Group.

CSA. (2019a). *Potential Expansivity of aggregates (procedure for length change due to alkali aggregate reaction in concrete prisms at 38C* (A23.2-14A).

CSA. (2019b). *Test method for detection of alkali silica reactive aggregate by accelerated expasnion of mortar bars* (A23.2-25A).

CSA Group. (2019). *A23.1:19/A23.2:19 Concrete materials and methods of concrete construction / Test methods and standard practices for concrete* (2019th ed.). CSA Group. www.csagroup.org

Cunha, Á., & Caetano, E. (2006). Experimental modal analysis of civil engineering structures. *Sound and Vibration*, *40*(6), 12–20.

Demerchant, D. P., Fournier, B., & Strang, F. (2000). Alkali-aggregate research in New Brunswick. *Canadian Journal of Civil Engineering*, *27*(2), 212–225. https://doi.org/10.1139/l99-077

Dewesoft. (2021). *What is Modal Analysis: The Ultimate Guide*. https://dewesoft.com/daq/what-is-modal-analysis#structural-dynamics-bridges-buildings

Dimri, A., & Chakraborty, S. (2024). Damage identification of reinforced concrete slabs using experimental modal testing and finite element model updating. *Structures*, *67*. https://doi.org/10.1016/j.istruc.2024.107023

Esposito, R., & Hendriks, M. A. N. (2019). Literature review of modelling approaches for ASR in concrete: a new perspective. *European Journal of Environmental and Civil Engineering*, *23*(11), 1311–1331. https://doi.org/10.1080/19648189.2017.1347068

Esposito, R., & Hendriks, M. A. N. N. (2012). A review of ASR modelling approaches for finite element analysis of dams and bridges. *14th International Conference on Alkali Aggregate Reaction*, (May 2015), 1-10 BT-International conference on alkali-aggr.

http://www.icaar2012.org/Home_Page.html%5Cnhttp://resolver.tudelft.nl/uuid:93bcc82f-da4b-4703-ad7a-2704f0de518e

Fournier, B., & Bérubé, M. A. (2000). Alkali-aggregate reaction in concrete: A review of basic concepts and engineering implications. *Canadian Journal of Civil Engineering*, *27*(2), 167–191. https://doi.org/10.1139/l99-072

Giaccio, G., Zerbino, R., Ponce, J. M., & Batic, O. R. (2008). Mechanical behaviour of concretes damaged by alkali-silica reaction. *Cement and Concrete Research*, *38*(7), 993–1004. https://doi.org/10.1201/9780203756768-5

Gillott, J. E., & Swenson, E. G. (1969). Mechanism of the alkali-carbonate rock reaction. *Quarterly Journal of Engineering Geology and Hydrogeology*, *2*(1), 7–23.

Girardi, M., Padovani, C., Pellegrini, D., Porcelli, M., & Robol, L. (2020). Finite element model updating for structural applications. *Journal of Computational and Applied Mathematics*, *370*, 112675. https://doi.org/10.1016/j.cam.2019.112675

Grattan-Bellew, P. E., Mitchell, L. D., Margeson, J., & Min, D. (2010). Is alkali-carbonate reaction just a variant of alkali-silica reaction ACR = ASR? *Cement and Concrete Research*, *40*(4), 556–562. https://doi.org/10.1016/j.cemconres.2009.09.002

Guggenberger, J. (2009). Model updating using operational data. *4th European Automotive Simulation Conference*, (July).

Guo, S., Dai, Q., Chang, L., Hu, Y., Xie, X., Si, R., & Wang, J. (2019). Kinetic analysis and thermodynamic simulation of alkali-silica reaction in cementitious materials. *Journal of the American Ceramic Society*, *102*(3), 1463–1478. https://doi.org/10.1111/jace.15961

He, J., & Fu, Z.-F. (2001). *Modal Analysis*. Butterworth Heinmann. web.b.ebscohost.com

Islam, M. S., & Ghafoori, N. (2015). Relation of ASR-induced expansion and compressive strength of concrete. *Materials and Structures/Materiaux et Constructions*, *48*(12), 4055–4066. https://doi.org/10.1617/s11527-014-0465-6

Islam, M. S., & Ghafoori, N. (2018). A new approach to evaluate alkali-silica reactivity using loss in concrete stiffness. *Construction and Building Materials*, *167*, 578–586. https://doi.org/10.1016/j.conbuildmat.2018.02.047

Langley, W. S. (2000). Alkali-aggregate reactivity in Nova Scotia. *Canadian Journal of Civil Engineering*, *27*(2), 204–211. https://doi.org/10.1139/cjce-27-2-204

Leger, P., Cote, P., & Tinawi, R. (1996). Finite element analysis of concrete due to alkali-aggregate reactions in dams. *Computers and Structures*, *60*(4), 601–611.

Li, Z., Afshinnia, K., & Rangaraju, P. R. (2016). Effect of alkali content of cement on properties of high performance cementitious mortar. In *Construction and Building Materials* (Vol. 102, pp. 631–639). https://doi.org/10.1016/j.conbuildmat.2015.10.110

Magalhães, F., & Cunha, Á. (2011). Explaining operational modal analysis with data from an arch bridge. *Mechanical Systems and Signal Processing*, *25*(5), 1431–1450. https://doi.org/10.1016/j.ymssp.2010.08.001

Malone, C., Zhu, J., Hu, J., Snyder, A., & Giannini, E. (2021). Evaluation of alkali–silica reaction damage in concrete using linear and nonlinear resonance techniques. *Construction and Building Materials*, *303*. https://doi.org/10.1016/j.conbuildmat.2021.124538

Maruyama, I., Sasano, H., Nishioka, Y., & Igarashi, G. (2014). Strength and Young's modulus change in concrete due to long-term drying and heating up to 90 °c. *Cement and Concrete Research*, *66*, 48–63. https://doi.org/10.1016/j.cemconres.2014.07.016

Marzouk, H., & Langdon, S. (2003). The effect of alkali-aggregate reactivity on the mechanical properties of high and normal strength concrete. *Cement and Concrete Composites*, *25*(4–5), 549–556. https://doi.org/10.1016/S0958-9465(02)00094-X

Mbarek, A., Del Rincon, A. F., Hammami, A., Iglesias, M., Chaari, F., Viadero, F., & Haddar, M. (2018). Comparison of experimental and operational modal analysis on a back to back planetary gear. *Mechanism and Machine Theory*, *124*, 226–247. https://doi.org/10.1016/j.mechmachtheory.2018.03.005

Mohammadi, A., Ghiasvand, E., & Nili, M. (2020). Relation between mechanical properties of concrete and alkali-silica reaction (ASR); a review. *Construction and Building Materials*, *258*, 119567. https://doi.org/10.1016/j.conbuildmat.2020.119567

Munir, M. J., Abbas, S., Qazi, A. U., Nehdi, M. L., & Kazmi, S. M. S. (2018). Role of test method in detection of alkali-silica reactivity of concrete aggregates. *Proceedings of Institution of Civil Engineers: Construction Materials*, *171*(5), 203–221. https://doi.org/10.1680/jcoma.16.00058

Na, O., Xi, Y., Ou, E., & Saouma, V. E. (2016). The effects of alkali-silica reaction on the mechanical properties of concretes with three different types of reactive aggregate. *Structural Concrete*, *17*(1), 74–83. https://doi.org/10.1002/suco.201400062

NB Power. (2016). *Considering the future of Mactaquac*.

Orlowitz, E., & Brandt, A. (2017). Comparison of experimental and operational modal analysis on a laboratory test plate. *Measurement: Journal of the International Measurement Confederation*, *102*, 121–130. https://doi.org/10.1016/j.measurement.2017.02.001

Pan, J., Feng, Y. T., Wang, J. T., Sun, Q. C., Zhang, C. H., & Owen, D. R. J. (2012). Modelling of alkali-silica reaction in concrete: A review. *Frontiers of Structural and Civil Engineering*, *6*(1), 1–18. https://doi.org/10.1007/s11709-012-0141-2

Pan, T., Chen, C., & Yu, Q. (2018). Microstructural and multiphysics study of alkali-silica reaction in Portland cement concrete. *Structural Concrete*, *19*(5), 1387–1398. https://doi.org/10.1002/suco.201700164

PCB Piezotronics. (2004). *Model 626B02 Industrial ICP ® Accelerometer Installation and Operating Manual*. https://www.pcb.com/imi-sensors

PCB Piezotronics. (2025). *Installation and Operating Manual ICP, Impact Hammer Model 086D20*. https://www.pcb.com/products?m=086d20

Poole, A. B. (2017). Introduction, Chesmistry and Mechanisms. In A. Poole & I. (RSK E. L. Sims (Eds.), *Alkali Aggregate Reaction in Concrete, A World Review* (pp. 38–65). Taylor and Francis Group.

Poprawa, G., Salamak, M., Pradelok, S., & Lazinski, P. (2017). Operational Modal Analysis in Model updating of a truss Railway Bridge. *7th International Operational Modal Analysis Conference*, 9–18.

Rainieri, C., & Fabbrocino, G. (2008). Operational Modal Analysis: overview and applications. *Strategies for Reduction of the Seismic Risk*, 29–44.

Revoredo, D. H. F., Nobrega, A. C. V., Carneiro, A. M. P., & Marciano, J. E. A. (2021). A Review Predictive Mathematical Modelling of Alkali-Silica Reaction in Concrete: evolution, current understanding and the knowledge gaps. *Research, Society and Development*, *10*(11). https://doi.org/10.33448/rsd-v10i11.19810

Ribeiro, D., Calçada, R., Delgado, R., Brehm, M., & Zabel, V. (2012). Finite element model updating of a bowstring-arch railway bridge based on experimental modal parameters. *Engineering Structures*, *40*, 413–435. https://doi.org/10.1016/j.engstruct.2012.03.013

RILEM. (2000). RILEM TC 106-AAR: alkali-aggregate reaction. In *Materials and structures* (Vol. 33, Number June).

Rogers, C. A. (1993). Alkali-aggregate reactivity in Canada. *Cement and Concrete Composites*, *15*(1–2), 13–19. https://doi.org/10.1016/0958-9465(93)90035-8

Rogers, C., Grattan-Bellew, P. E., Doug Hooton, R., Ryell, J., & Thomas, M. D. A. (2000). Alkali-aggregate reactions in Ontario. *Canadian Journal of Civil Engineering*, *27*(2), 246–260. https://doi.org/10.1139/l99-073

Roy, S. T. R., & Morrison, J. A. (2000). Experience with alkali-aggregate reaction in the Canadian prairie region. *Canadian Journal of Civil Engineering*, *27*(2), 261–276. https://doi.org/10.1139/l99-068

Sahin, A., & Bayraktar, A. (2014). Forced-vibration testing and experimental modal analysis of a steel footbridge for structural identification. *Journal of Testing and Evaluation*, *42*(3). https://doi.org/10.1520/JTE20130166

Sanchez, L. F. M., Multon, S., Sellier, A., Cyr, M., Fournier, B., & Jolin, M. (2014). Comparative study of a chemo-mechanical modelling for alkali silica reaction

(ASR) with experimental evidences. *Construction and Building Materials*, *72*, 301–315. https://doi.org/10.1016/j.conbuildmat.2014.09.007

Saouma, V. (2013). Numerical Modelling of AAR. In *Numerical Modelling of AAR*. CRC Press, Taylor and Francis Group. https://doi.org/10.1201/b16353

Saouma, V. E., Martin, R. A., Hariri-Ardebili, M. A., & Katayama, T. (2015). A mathematical model for the kinetics of the alkali-silica chemical reaction. *Cement and Concrete Research*, *68*, 184–195. https://doi.org/10.1016/j.cemconres.2014.10.021

Saouma, V., & Perotti, L. (2006). Constitutive model for alkali-aggregate reactions. *ACI Materials Journal*, *103*(3), 194–202. https://doi.org/10.14359/15853

Schrötter, M., & Hagara, M. (2013). The Results Comparison of Experimental and Operational Modal Analysis of a Fixed Cantilever. *American Journal of Mechanical Engineering*, *1*(7), 190–193. https://doi.org/10.12691/ajme-1-7-7

Sehgal, S., & Kumar, H. (2016). Structural Dynamic Model Updating Techniques: A State of the Art Review. *Archives of Computational Methods in Engineering*, *23*(3), 515–533. https://doi.org/10.1007/s11831-015-9150-3

Shi, Z., Shi, C., Wan, S., & Ou, Z. (2017). Effect of alkali dosage on alkali silica reaction in sodium hydroxide activated slag mortars. *Construction and Building Materials*, *143*, 16–23.

Shrimer, F. H. (2000). Experience with alkali-aggregate reaction in British Columbia. *Canadian Journal of Civil Engineering*, *27*(2), 277–293. https://doi.org/10.1139/l99-058

Shrimer, F. H. (2005). Progress in the Evaluation of Alkali-Aggregate Reaction in Concrete Construction in the Pacific Northwest, United States and Canada. *U.S. Geological Survey Bulletin 2209-K*, 11.

Siegert, D., Multon, S., & Toutlemonde, F. (2005). Resonant frequencies monitoring of alkali aggregate reaction (AAR) damaged concrete beams. *Experimental Techniques*, *29*(6), 37–40. https://doi.org/10.1111/j.1747-1567.2005.tb00245.x

Sims, I., & Poole, A. (Eds.). (2017). *Alkali Aggregate Reaction in Concrete A world Review*. CRC Press, Taylor and Francis Group.

SIMULIA. (2006, March 1). *ABAQUS V6.6 Documentation*. ABAQUS User Manual. https://classes.engineering.wustl.edu/2009/spring/mase5513/abaqus/docs/v6.6/books/usi/default.htm?startat=pt06ch41s01s04.html

SIMULIA. (2019, July 9). *Getting started with Abaqus* [Video recording]. https://www.youtube.com/watch?v=zdR9mc39KWo&list=PL_Z4wsnQjTNGg6gWNL4mmbScM2OdV05U1

Stanton, T. E. (1940). Expansion of concrete through reaction between cement and aggregate. *American Society of Civil Engineers*, 1781–1811.

Steve McDonald. (2016). *Operational Modal Analysis , Model Updating and Seismic Analysis of a Cable-Stayed Bridge* [Master's Thesis]. University of British Columbia.

Structural Vibration Solutions. (2025). *Modal Complexity Factor*. https://svibs.com/resources/ARTeMIS_Modal_Help_v7/webframe.html#Generic%20Complexity%20Plot.html

Tänzer, R., Jin, Y., & Stephan, D. (2017). Effect of the inherent alkalis of alkali activated slag on the risk of alkali silica reaction. *Cement and Concrete Research*, *98*(February), 82–90. https://doi.org/10.1016/j.cemconres.2017.04.009

Towner, R. L., & Band, J. L. (2012, June 14). An Analysis Technique/Automated Tool for Comparing and Tracking Analysis Modes of Different Finite Element Models. *53rd AIAA/ASME/ASCE/AHS/ASC Structures, Structural Dynamics and Materials Conference*. https://doi.org/https://doi.org/10.2514/6.2012

Ventura, C. E., Brinker, R., & Andersen, P. (2001). Damping Estimation by Frequency Domain Decomposition. *IMAC 19: A Conference on Structural Dynamics*, 698–703.

Yurtdas, I., Chen, D., Hu, D. W., & Shao, J. F. (2013). Influence of alkali silica reaction (ASR) on mechanical properties of mortar. *Construction and Building Materials*, *47*, 165–174. https://doi.org/10.1016/j.conbuildmat.2013.04.046

Appendix A: Instrumentation

Table of Contents

This appendix contains the following tabulated information, arranged as follows

Page Number	Data
158	A-1: Instrumentation Layout: Diagram showing the OMA and EMA sensor layout.
159	A-2: Apparatus List. List of all apparatus used in the experiments.
162	A-3: Experimental Procedure: Collection of experimental notes developed for the specimen instrumentation.
173	A-4: Hammer Tip Selection

A-1: Instrumentation Layout

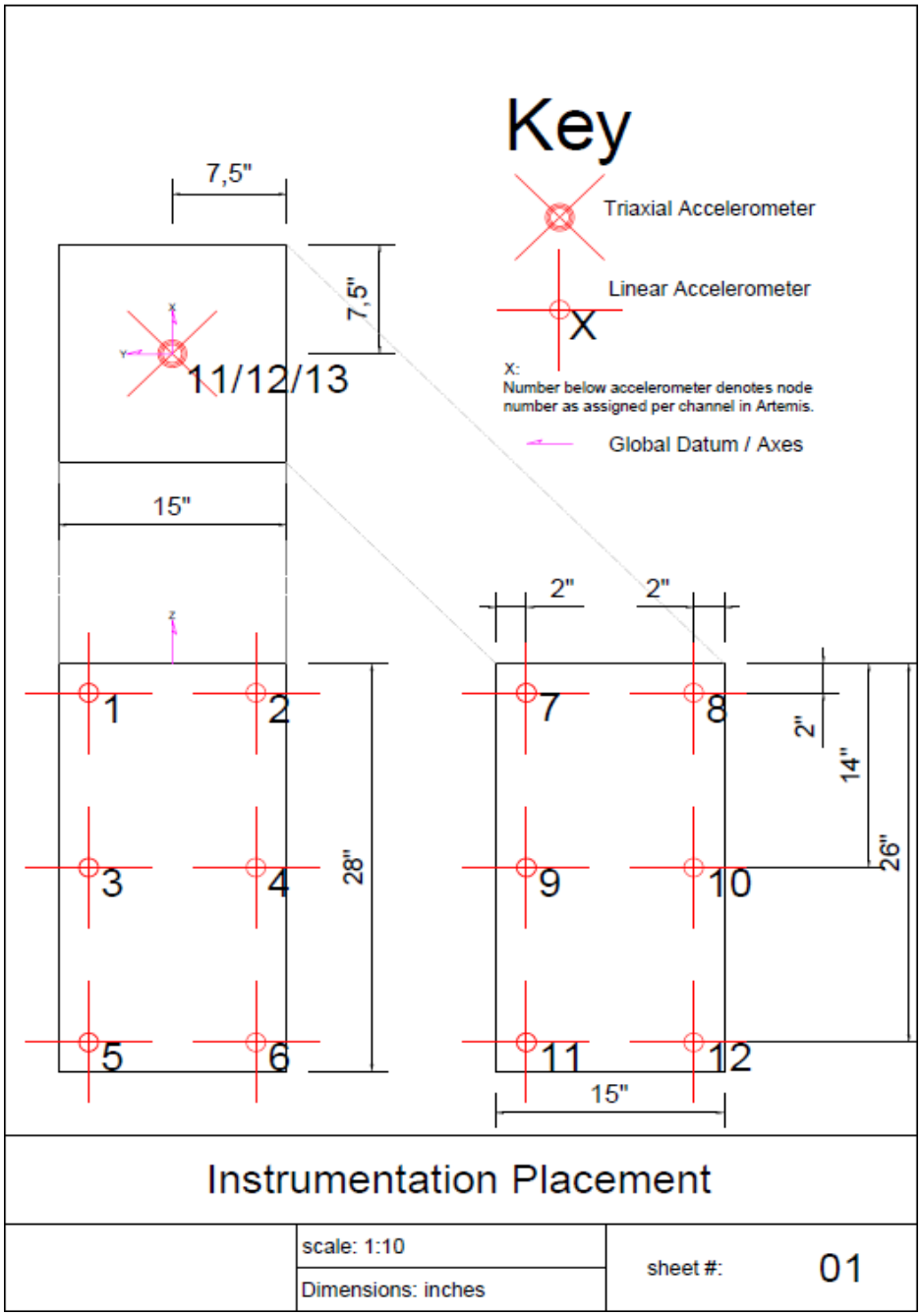


Figure A1: Sensor layout on specimens

A-2 Equipment and Software Inventory

The sensors used in this campaign are listed in Table A1. The DEMEC gauge is also listed for completeness. The excitation hardware is listed in Table A2, the data acquisition hardware in Table A3, the mounts and consumables in Table A4 and the list of software in Table A5.

Table A1: Sensor inventory

Item	Manufacturer	Model	Count
Uniaxial Accelerometer	PCB Piezotronics	626B02	12
Triaxial Accelerometer	PCB Piezotronics	626A32	1
DEMEC gauge	Mayes Instruments	500 mm gauge	1

Table A2: Excitation hardware

Item	Manufacturer	Model	Notes
Short-Sledge Impact Hammer	PCB Piezotronics	086D20	-
Hammer tips	PCB Piezotronics	Hard, Medium, Soft, Super-Soft	Medium tip selected for testing
Manual OMA excitation	-	Standard basketball	Used for forced ambient tests

Table A3: Data acquisition inventory

Item	Manufacturer	Model	Notes
Primary DAQ	National Instruments	cDAQ 9189	Used for blocks A, AA, AS, AN under OMA, and for all EMA testing across all blocks. Sample rate 10.24 kHz; 4 V drive
DAQ input modules	National Instruments	NI-9232	4 modules of 3 channels each

Item	Manufacturer	Model	Notes
Earlier DAQ chassis	Crystal instruments	Spider-80	Used for OMA testing of blocks R (16 kHz), F, AC, and AB (12.8 kHz) prior to the cDAQ transition.

Table A4: Mounts and consumables

Item	Specification	Source
Accelerometer Mounting Pads	Custom-machined 304 stainless steel discs, Ø 35 by 10 mm, with centre-threaded blind hole matched to the accelerometer mounting bolt	Fabricated in-house.
Coupling Fluid	Hyprez OS Type 4 Lubricant	Materials laboratory stock
Mounting Adhesive	Rezi-Weld structural epoxy	Selected based on previous mounting trials.
Specimen Moisture Control	Untreated burlap	Used to limit desiccation during laboratory storage.

Table A5: Software inventory

Item	Vendor	Version	Purpose
Modal Analysis Platform	Structural Vibration Solutions	ARTeMIS Modal Pro	OMA and EMA estimator suite. Data collection.
FE Engine	Dassault Systèmes	ABAQUS 2022	Linear Perturbation eigenfrequency analysis
Model Updating	Dassault Systèmes	Isight 2022	Pointer and LSGRG optimisation; Abaqus parameter passing

Item	Vendor	Version	Purpose
Numerical computation and validation	Matlab	Matlab R2023a	Cross-power spectrum and SVD validation; cross-MAC; mode-shape plotting. Isight data post processing.
Spreadsheet post processing and document preparation	Microsoft	Office 365	Error metric tabulation, record keeping. Thesis preparation.

A-3: Experimental Procedures

This section provides more information that is specific to the instrumentation of the blocks. This section was developed as part of the study because such techniques are mostly experiment specific and are not reported in literature. It is hoped that this section provides guidance for concrete surface instrumentation. Figure A2 shows a schematic of a typical accelerometer on the concrete surface. Each of the various points labelled 1 through 4 were identified as needing special consideration due to the non-destructive nature of the testing.

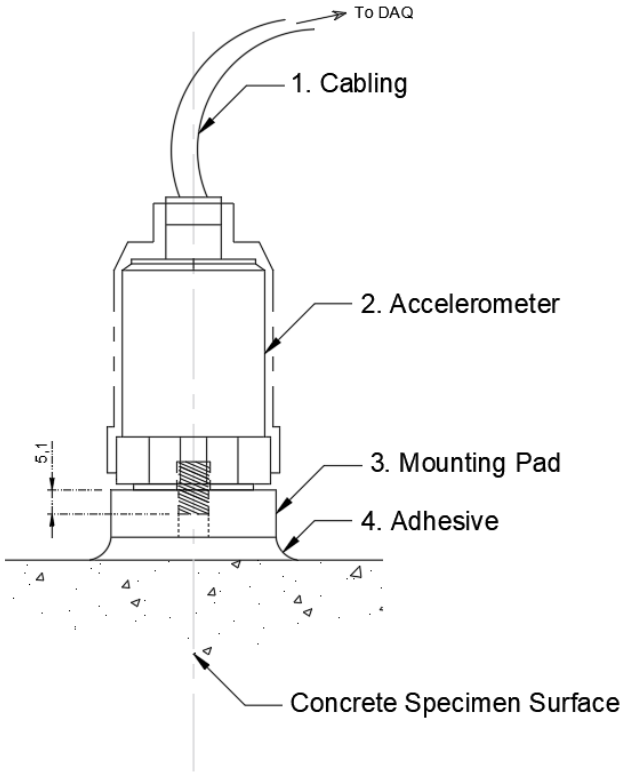


Figure A2: Experimental considerations

1. Cabling

The cables used to connect the accelerometers to the NI-DAQ are standard shielded coaxial cables supplied by the accelerometer manufacturer. They are approximately 10’ long and have BNC connectors on either side for the linear accelerometers and a special four socket connector for the triaxial accelerometer. Even though they are shielded internally, some precautions were taken for minimising the introduction of noise in the system as recommended by the manufacturer’s operating instructions(PCB Piezotronics, 2004). The cables were uncoiled as much as possible to avoid heating effects and they were kept as far away as possible from electrical sockets, machinery or other electronic devices.

The available driving voltages from the DAQ (Data Acquisition system) used were either two or four volts. The higher one was used even though through tests there were no observable differences in the two voltages in terms of PSD. The higher driving voltage was used.

2. Accelerometer Specifications

The accelerometers used in this experiment are the model 625B02 uniaxial accelerometers and the 629A32 triaxial accelerometer from PCB Piezotronics. The DAQ originally used was from Crystal Instruments Spider 80 but was later switched to the cDAQ from NI instruments mounted with four 3-channel NI-9232 input modules. All accelerometer channels have a maximum deviation of ±3.5% (the maximum at 12kHz of the z axis channel of the triaxial accelerometer). From the OEM manual (PCB Piezotronics, 2004), the following usage instructions and information were obtained and their application given:

a) Mounting Method

The type of mount used to connect the accelerometer to the specimen affects the high frequency response of the measurement while generally unaffecting the low frequency response. The deviation with respect to mounting methods is shown in Figure A3.

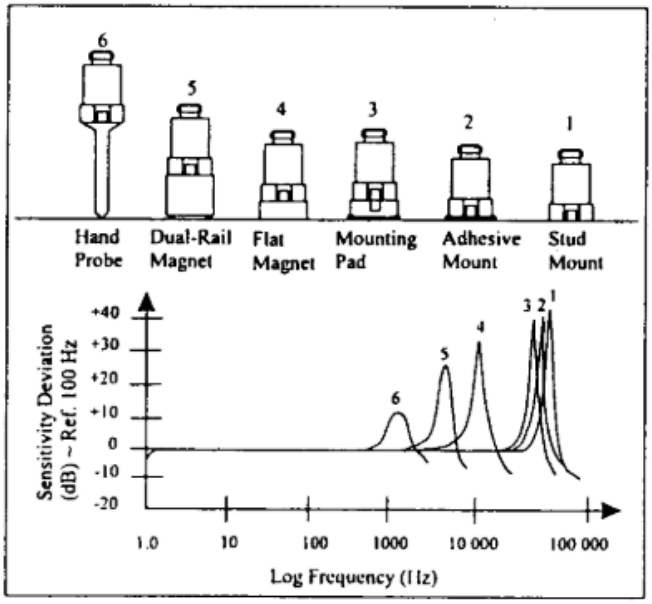


Figure A3: Accelerometer - mounting type deviations (PCB Piezotronics, 2004)

The choice of mount is influenced by two factors: what the specimen can accommodate without being damaged and how wide do the wanted frequency range for the measurement need to be. Since an increased frequency range is a better measurement, since it increases the Nyquist frequency, the choice resides directly on the mounting methods. Mounting by magnet is impossible on direct concrete, hand probing is also unachievable, the three best options are considered. Stud and adhesive mounts would damage the specimen or the accelerometer respectively, so the mounting pad method was chosen. This allowed for vibration recording at the full range of the accelerometer at 12-

16 kHz on the Crystal Instruments spider-80 DAQ as opposed to 10.4kHz recorded/ sampling frequency on the c DAQ.

Accelerometer pads were prepared from 304 stainless steel from a previous experiment for use in concrete immersed in sodium hydroxide. These pads are shown in Figure A4, and measure 35 mm in diameter and 10 mm in thickness. They have a threaded hole in the centre to accommodate the accelerometer bolt. The diameter was made to match the accelerometer diameter while the thickness was limited to handling, either manually or with wrenches. The pads were made to be as small as possible to minimise uneven weights on the specimens and mass loading, a phenomenon whereby the mass on the instrumentation changes the specimen response through changed mass distribution.



Figure A4: Typical Mounting Pad

b) Mounting Torque and Surface preparation

The recommended mounting torque to fix the accelerometer to any type of mounts is from two to five foot-pounds of torque. This was tested using a torque wrench

and found to be within range of hand tightening the accelerometers; therefore, the accelerometers were tightened by hand. The torque wrench was also found to damage the top of the mounting pads, which disfavoured the former even more.

Between the accelerometer and the mounting pad, the manufacturer recommends using a thin film of coupling fluid to improve vibration transmission by filling in voids and gaps caused by microscopic defects. The coupling fluid used was a machining lubricating oil readily available in the materials laboratory, the Hyprez OS Type 4 lubricant. It was found to be easily applied and cleaned off.

c) Adhesive

The adhesive used for fixing the accelerometer pads to the concrete surface needed to be compatible with the materials (steel and concrete), stiff to transmit vibration and not act as a damper, and removable. The only common available adhesive for steel and concrete is epoxy resin and between the available choice of common household epoxy (gorilla glue clear epoxy) and Rezi weld structural grade epoxy, a small experiment was performed as shown in Figure A5 to find out which would be better. 3M mounting tape was also included in the experiment. It was found that the mounting tape, while suitable for most applications, was inadequate for this type of old concrete since it would absorb surface dust and not stick properly. The gorilla glue was found to be less stiff than the Rezi weld epoxy upon testing both side by side with hammer impacts on a pad and left a residue upon removal. The structural epoxy was chosen as adhesive.



Figure A5: Adhesive experiment on a surplus concrete beam.

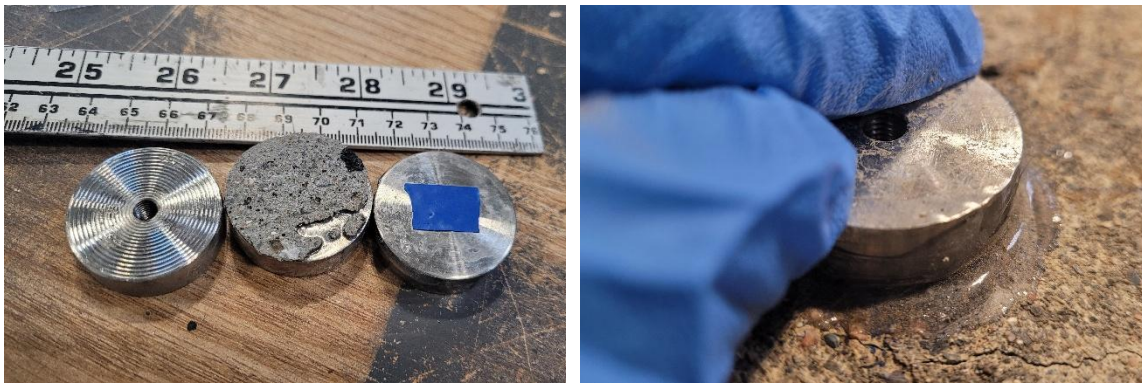
The other factor is the removal of the adhesive from the concrete and the pads. Another experiment was conducted to test which applicable method would be suitable. Shown in Figure A6 are three types of investigated methods: from left to right are universal solvent, paint thinner in part (a), and direct blow shown in part (b). For the solvents to work, they had to be applied consistently around the edges or dripped into the threaded hole to contact the adhesive. This proved to be very time consuming compared to the direct blow since it took 15 to 45 minutes for the solvent to work compared to the few seconds it took to impact the pads progressively till lift off. The solvent also left a residue on the concrete which smeared upon removal and is not acceptable for these specimens. Smearing of the adhesive over a large surface area would act as a waterproof barrier and cause differential water uptake and discharge of the specimen.



(a) (b)

Figure A6: Adhesive removal experiment. Solvents in (a), Torque in (b).

Furthermore, to prevent the resin from entering the threaded hole and permanently fixing the accelerometer to the mounting pad, a small piece of tape shown in Figure A7 (a) was used to block of the hole on the adhesive side which reduced the solvent contact area. However, the direct blows sometimes removed part of the concrete surface, shown on the second pad in Figure A7 (a). It was found that instead of impacting the pads, torquing them was better since it either left the adhesive on the concrete or on the pad. A meniscus that is well formed, such as in Figure A7 (b) also helped in the clean break off the bond.



(a) (b)

Figure A7: Accelerometer pad removal

The accelerometer bolts are brass inserts and are around 7mm across and only have a protrusion of up to 5mm from the accelerometer. It was found that these tips can get damaged easily, especially the starting threads, by any burrs on the accelerometer pads and to help against it and ensure proper installation, the pads were filled and re-threaded prior to use on each specimen. Shown in Figure A8 (a), the pads were threaded using both a bolt and a thread cutter matching the accelerometer studs; the inclusion of the bolt in the process ensured no metallic residue interfered and damaged the accelerometer studs. The adhesive was removed from under the pads by chiselling and direct impact with a steel mallet as shown in Figure A8 (b). The latter also shows the effect of improper removal of the pads from the specimens. Chips of concrete may become lodged onto the pads and break off, thereby damaging the specimens. This happened and was caught onto trial concrete and was corrected with the torquing method of removal.



(a) (b)

Figure A8: Accelerometer pad cleanup step. Rethreading procedure shown in (a) and residue removal in (b).

d) Concrete specimen

The adhesive on the concrete surface was removed by chiselling and light filling as this proved to be the best option. Grinding and heat application were investigated but heavy grinding heated up the epoxy resin which caused foul smelling particulates to be released which were pervious to welding and chemical respiratory masks. Heating alone necessitated too much time for the adhesive to break down, and the surrounding concrete

was judged to be too hot, risking thermal cracking. Through careful horizontal chiselling and sanding, the surface loss on the specimens was on average, less than a millimetre.

The primary consideration for the concrete in terms of mounting the accelerometers was the concern that the epoxy would solidify in the concrete cracks. Removal of the adhesive and/or mounting pad with the adhesive might lift off cracked concrete or cause severe spalling. These are ASR specimens and therefore present may cracks which cannot be avoided by the mounting pad locations. This problem was solved using wax as shown in Figure A9. For marking out the locations of the mounting pads, a blue lead pencil (Steadler's 2mm carbon blue lead) was used, and it was found to be suitable for masking the cracks since it is water washable, easily sanded on concrete and did not stick to the epoxy resin because of its waxy consistency.

Finally, the last concern for the concrete specimens were their drying rates in the laboratory as compared to their outside exposure site conditions. The laboratory space was air conditioned and of lesser humidity than outside. Therefore, in order to prevent excessive drying out compared to their annual cyclic moisture exchange, the specimens were covered in wet burlap to stop desiccation during the test process.

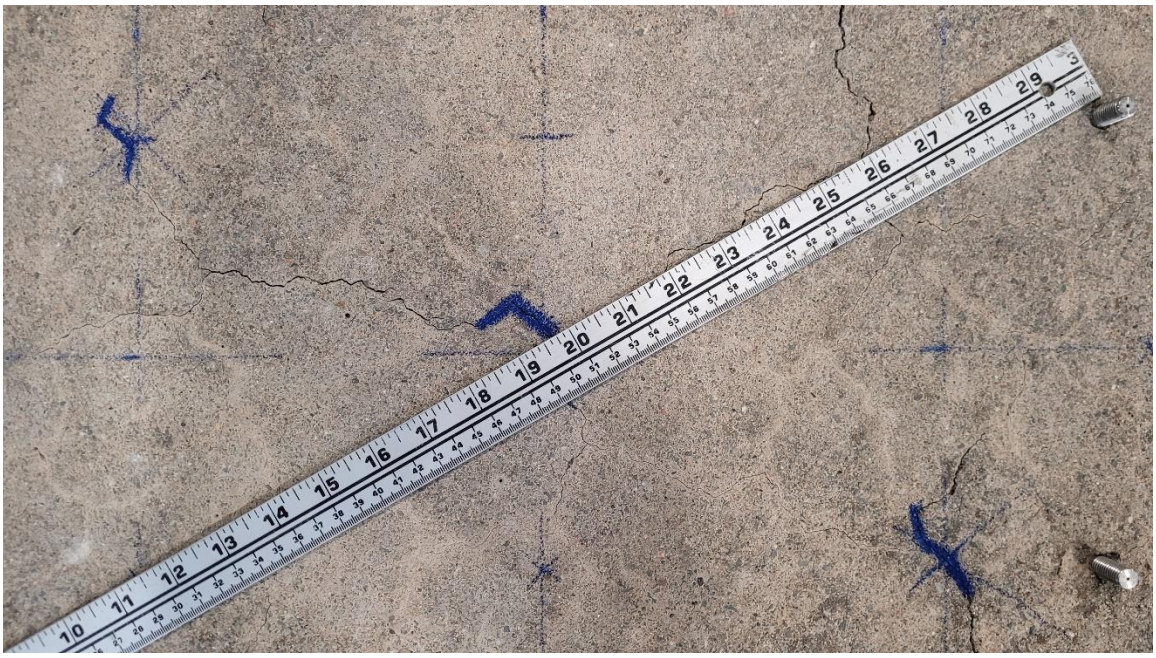


Figure A9: Crack protection of the concrete specimens.

A-4: Hammer Tip Selection

This section serves as the presentation of the test carried out to find the best suited hammer tip to be used in the study. Shown in Figure A10 are the response curves of the hammer with different tips as provided by the manufacturer. They are provided as the response based on impacts on a stiff steel mass which is not insightful for this study as the response on concrete is expected to be very different due to the large gap between their stiffnesses.

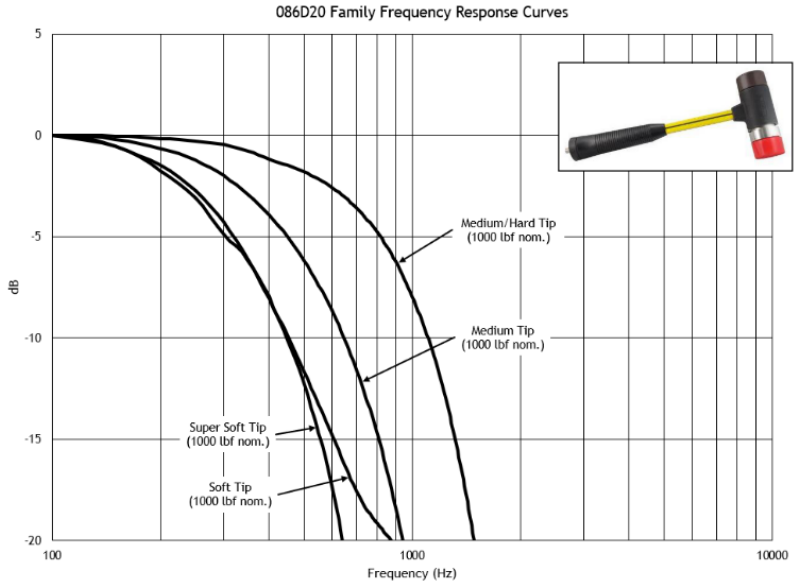


Figure A10: Impact hammer response curves on steel mass (PCB Piezotronics, 2025)

The pre-test was conducted on block AA with the triaxial accelerometer on the centre of the top face on a stand-up setup on the heavy concrete floor. For each tip, the hammer was impacted on one point, the top left corner, for 6 successful impacts, i.e., no double hits and proper excitation captured in the selected window. A typical acceleration-time plot of the x direction (direction of travel of the hammer upon impact) is shown in

Figure A11. The x direction data is the x axis channel of the triaxial accelerometer. The data window of 1.6s was chosen based on the damp out of the vibration by 0.8s on all blocks with some outlier shocks present at 1.2s.

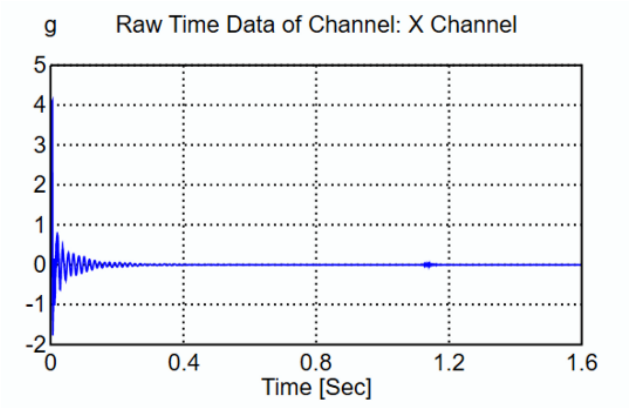


Figure A11: Accelerometer time data window for hard tip

The test was carried out for all hammer tips at a specified trigger level of 400 and 5000 N. this was done to investigate whether the force applied would result in a better signal capture or introduce more noise with respect to the block moving and wobbling on the floor. A trigger of 5 kN was initially chosen since the reference frequency response curves were given at 1000 pounds force of nominal impact force, equating to about 4.4 kN of impact force.

Table A6 provides the spectral densities of the hammer with respect to tip hardness and trigger level while Table A7 shows the spectral densities for the output x channel. All plots in these tables have for their y axis a decibel magnitude scale and for their x axis a linear frequency scale. In simpler words, Table A6 shows the fast Fourier transform (FFT) of the hammer whereas Table A7 shows the FFT of the x axis of the triaxial accelerometer.

The distinction to make while comparing the hammer spectral densities is that the transfer of energy appears to be fairly consistent for all tips and impact force with the majority of the excitation occurring in the sub 2000 Hz region with a significant drop off around the 1100 Hz region. One would therefore assume that the impacted energy would be distributed in the sub 1100 Hz region, but the output spectrums are used instead.

The output spectrums reveal that for the region below 1100 Hz, there is no peaks that could be picked. the soft and super soft output spectrum were found to be loosely inversely proportional with respect to impact energy and spectrum noise. Hard and medium tips provided cleaner output spectrums with the 5000 Hz trigger while the soft and super soft tips provided a cleaner output spectrum in the 400 N trigger test.

Table A6: Hammer Spectral Densities

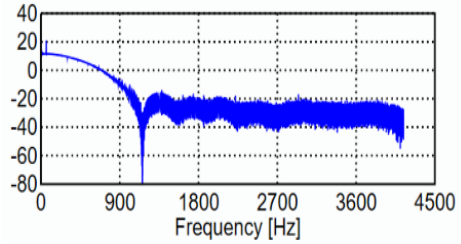
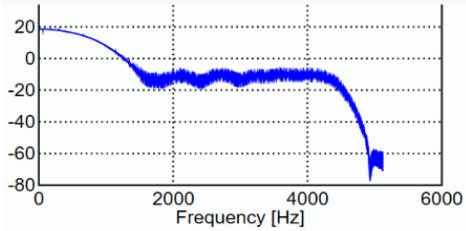
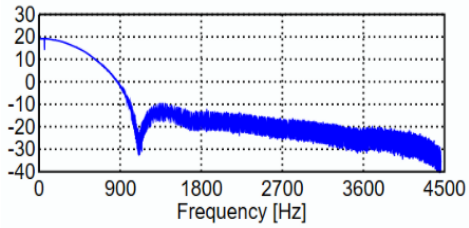
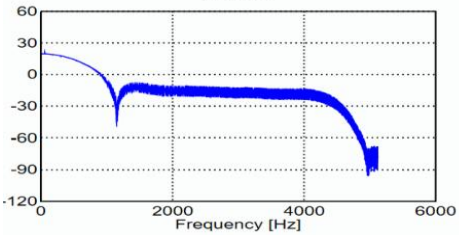
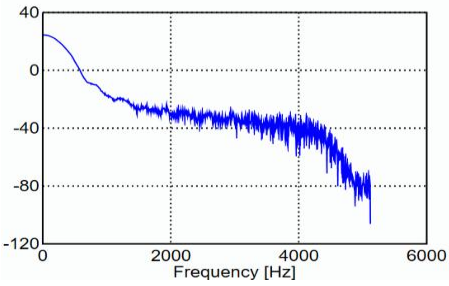
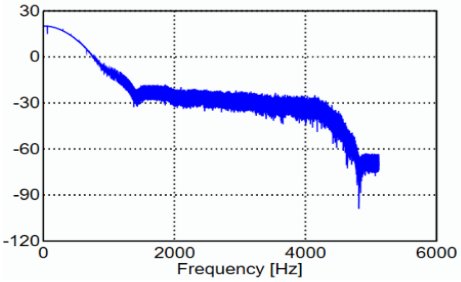
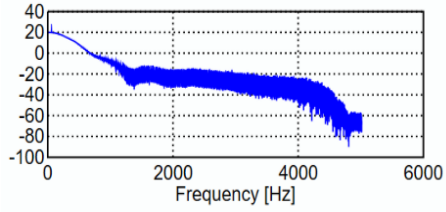
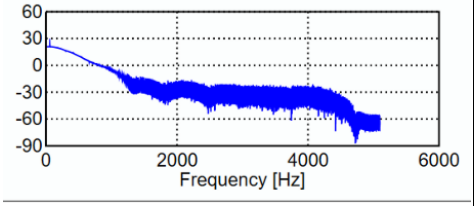
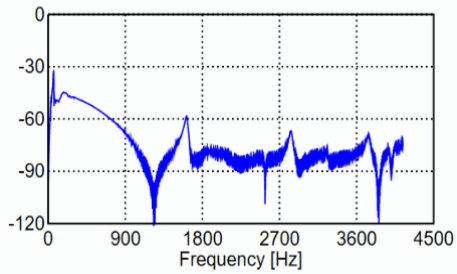
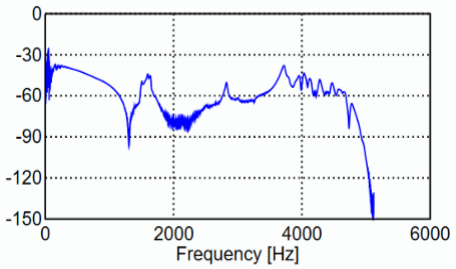
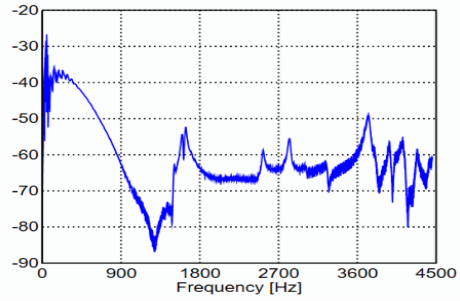
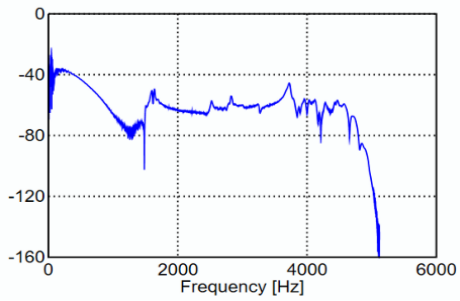
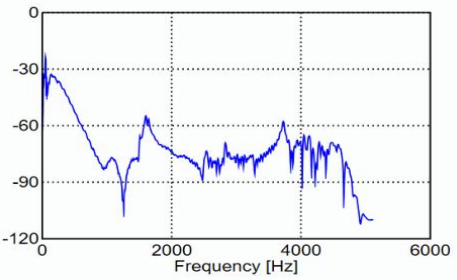
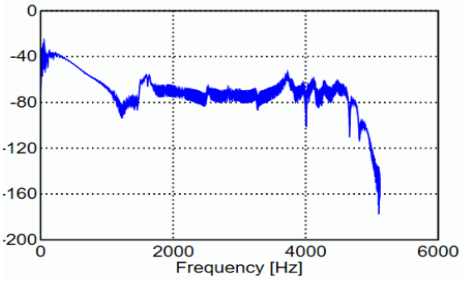
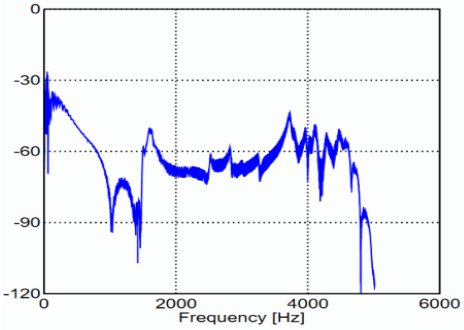
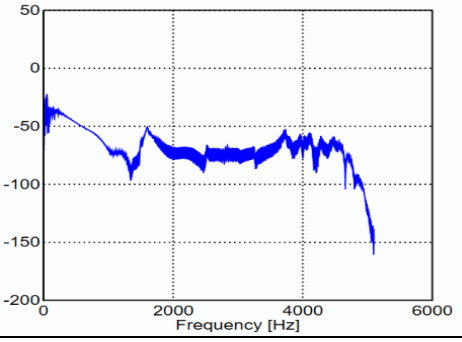
Tip Hardness	Low Energy 400 N Trigger	High Energy 5000 N Trigger
Hard		
Medium		
Soft		
Super Soft		

Table A7: X-channel spectral densities

Tip Hardness	Low Energy 400 N Trigger	High Energy 5000 N Trigger
Hard		
Medium		
Soft		
Super Soft		

On top of using the spectrums as information to make a tip choice, there is also the experimentation side. The hard tip was found to be too cumbersome to use as the double hits were uncontrollable. The soft and super soft tips were physically exhausting to use; the amount of physical exertion required, combined with the awkward user position for impacts made them significantly harder to use than the harder counterparts.

The clear decision was to use the medium tip since in terms of input excitation, there were no significant difference across all tips, and it offered a usable output spectrum.

Gradually incrementing the trigger level was found the best way to calibrate the hammer trigger level to firstly reduce or eliminate double hits and to properly impart readable energy to the specimen, i.e., properly excite the specimen such that the resonant frequency peaks are identified on screen by the user. Combined with the fact that normal operation of the hammer resulted in impact forces in the region of 1000 N, the trigger was set to 1200 N. Throughout the tests, it was observed that the blocks were more prone to shifting based on the amount of force applied across which nodes.

Topmost nodes were impacted with a more controlled grip on the hammer, and the range of impact force were around 1500 N to limit perceived movements and shifting of the entire block while bottom nodes were impacted with forces of up to 5000 N with a clear output spectrum and no perceived shifting.

The choice of eight impacts per node was made in order to be able to selectively remove any impacts in post processing. This would allow a parametric analysis in terms of number of impacts required for best results, as a counterpart to OMA, where a parametric analysis could be done by taking segments of the 10-minute recordings to

investigate the optimum measurement time. However, both parametric comparisons were dropped due to time constraints. The analysed number of impacts remained at 8.

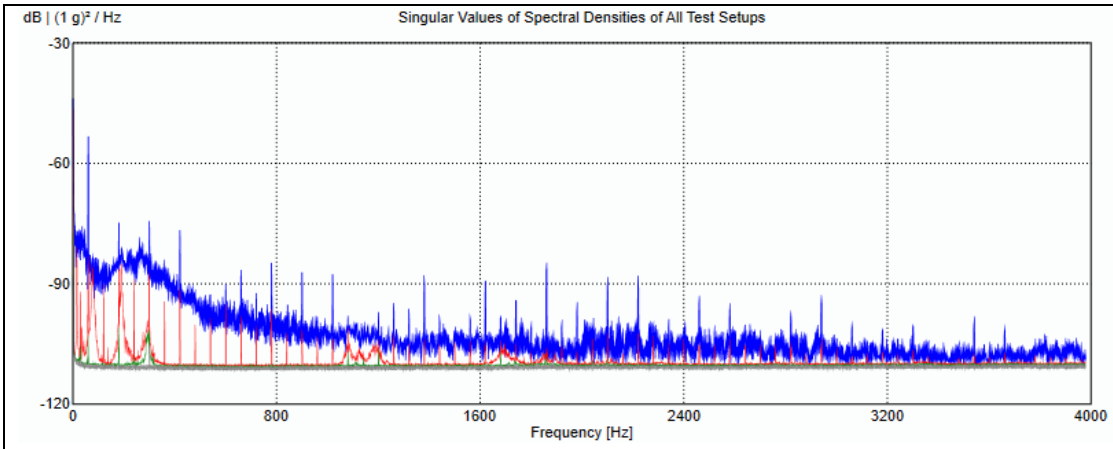
Appendix B: Modal Analysis Results – Block A

This appendix lays out the modal analysis steps data for block A as performed in ARTeMIS. The power spectrums, SVD lines from ARTeMIS are presented along with the attempted validation from Matlab. Following which the user chosen mode shapes are laid out with respect to each analysis method for OMA and EMA the n the frequencies are tabulated. This table shows the individual method frequencies before they are averaged for FE model updating. Mode shapes that are chosen are shown again in the last table with comments and their proposed mode order number as laid out in the preliminary FE analysis.

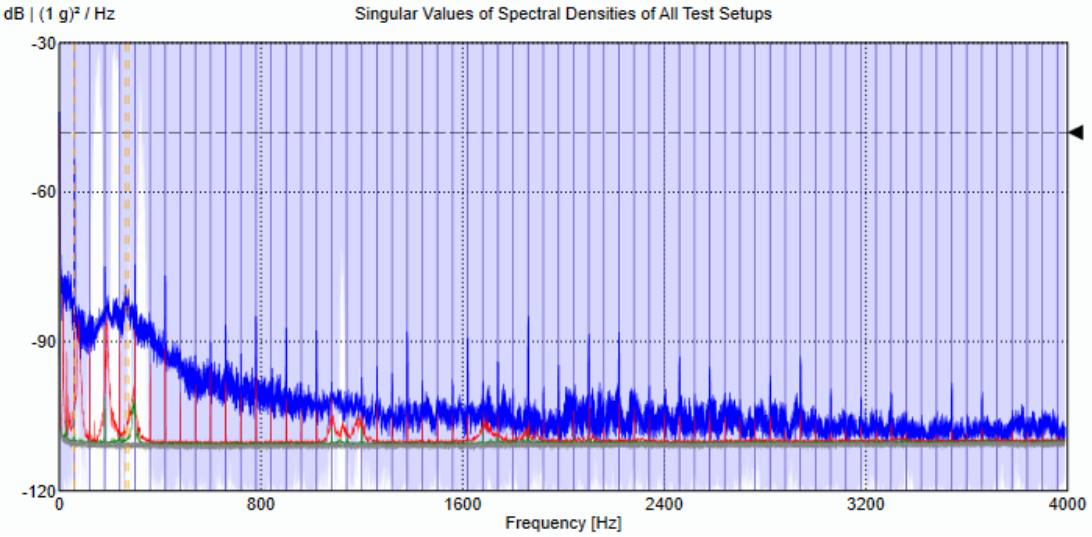
Block A

Power Spectrum Densities

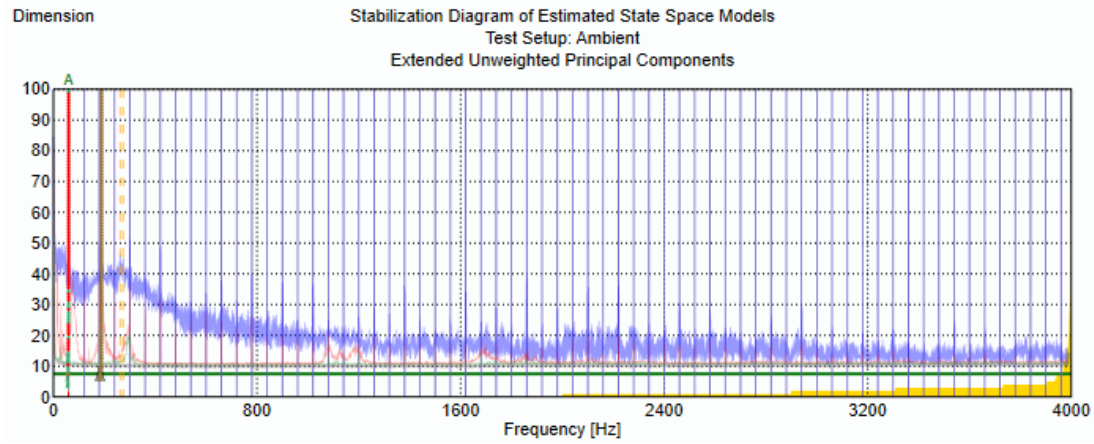
Table B1: Power Spectrum Densities- block A



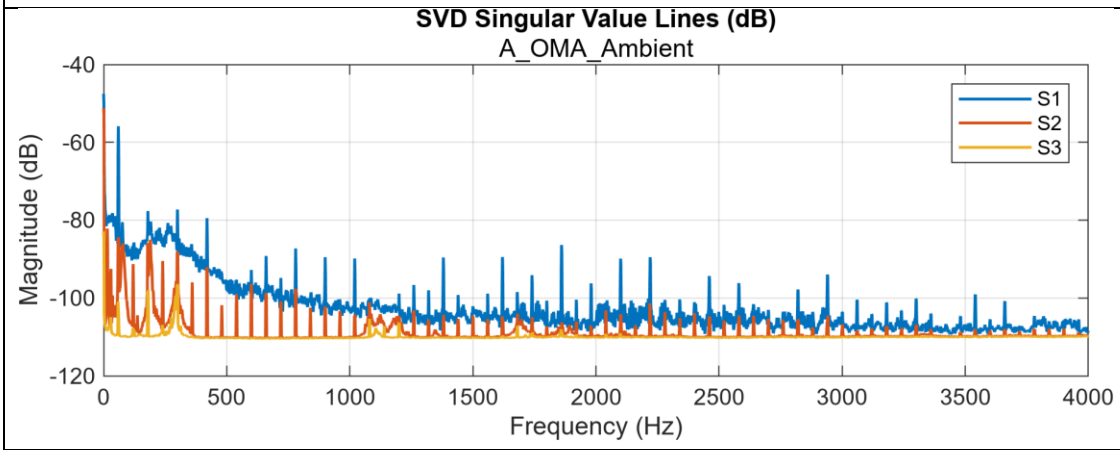
OMA- Ambient Blank Frequency Data



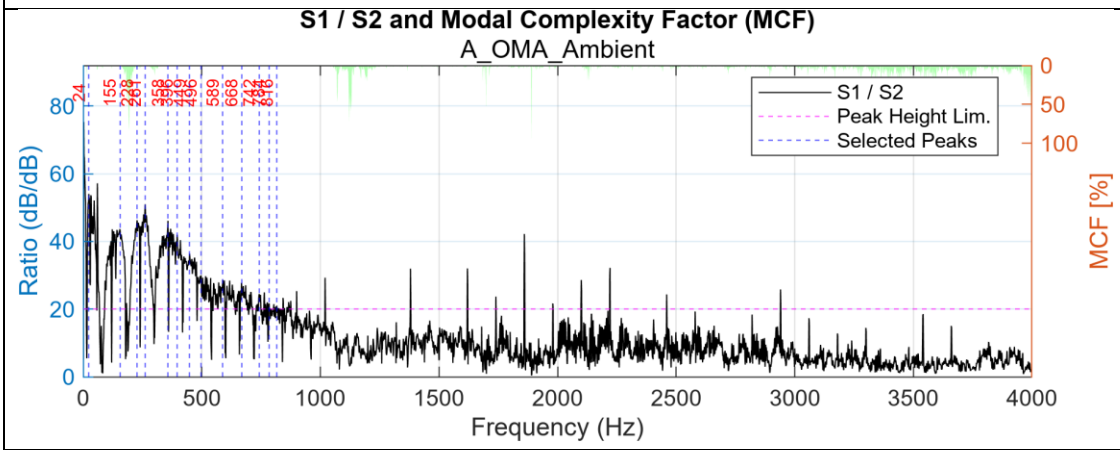
OMA – Ambient Estimator Step EFDD



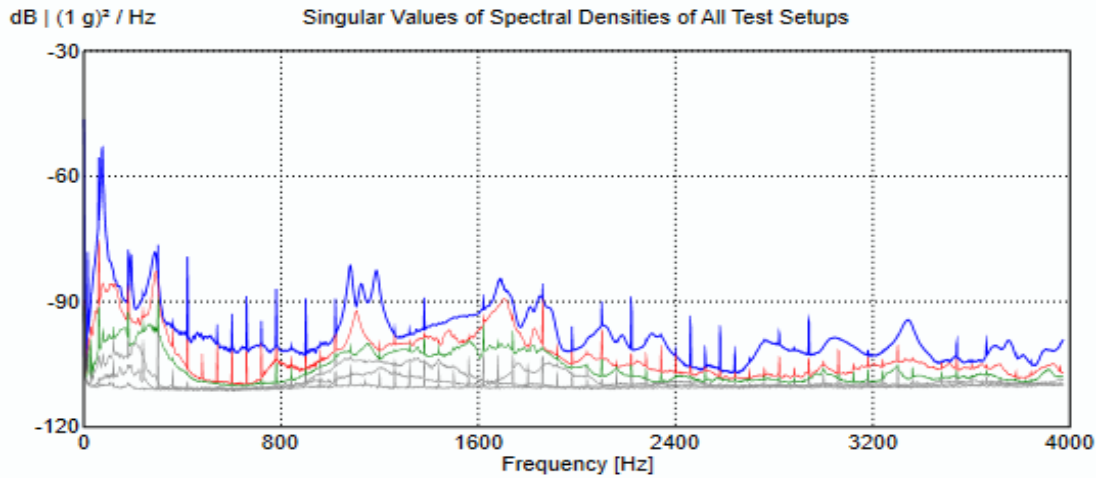
OMA – Ambient Estimator SSI – UPCx



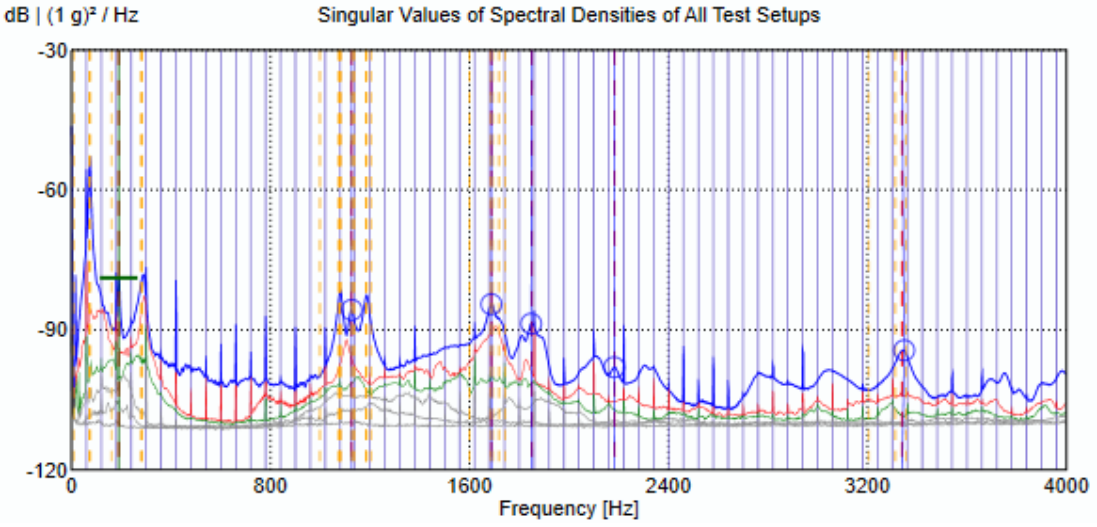
OMA-Ambient SVD plots from Matlab



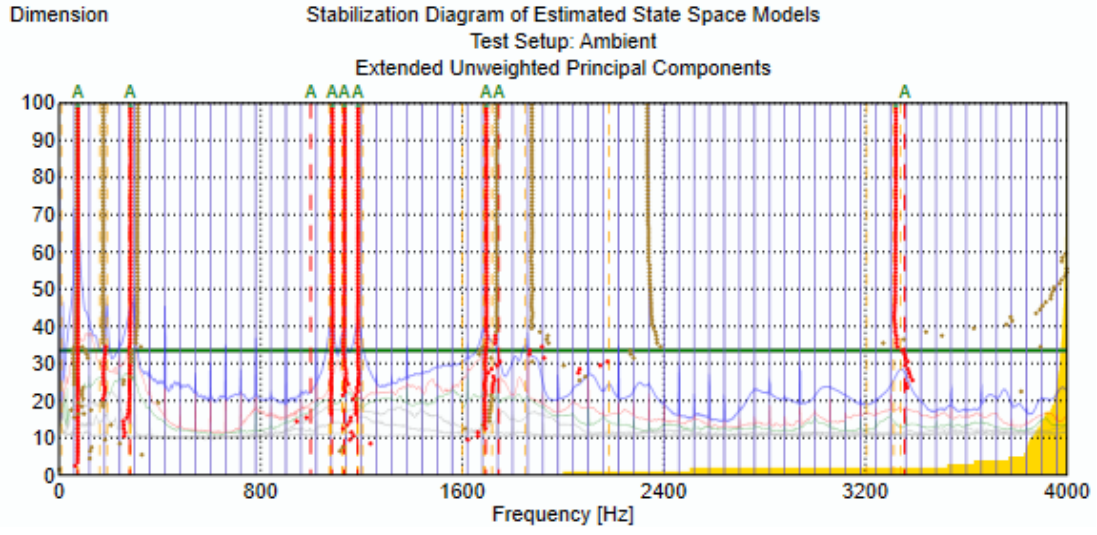
OMA-Ambient S1 over S2 plot from Matlab



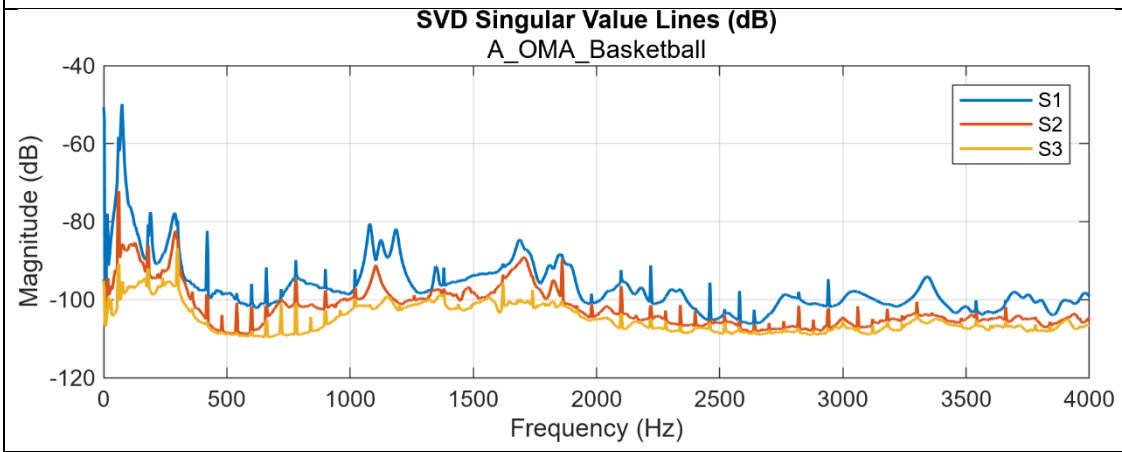
OMA –Basketball Blank Frequency Data



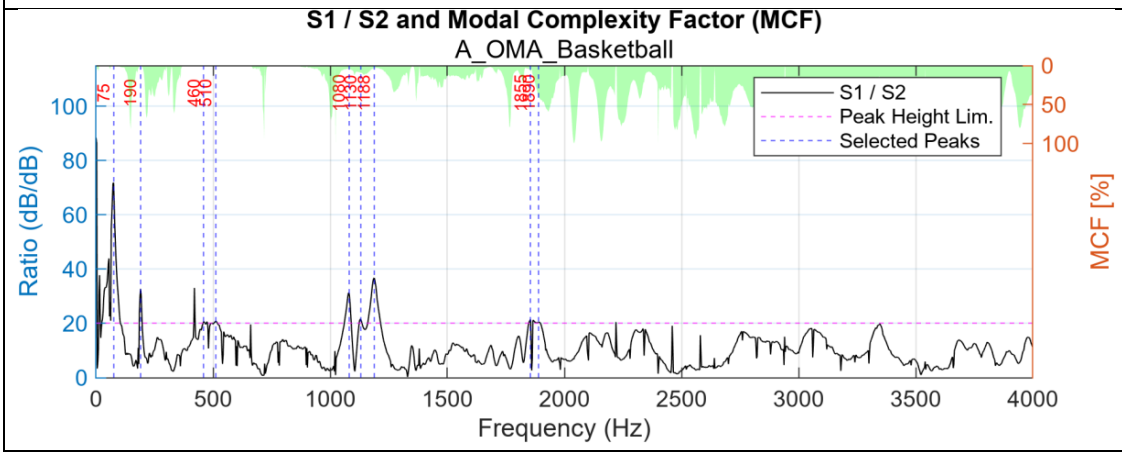
OMA- Basketball Estimator step EFDD



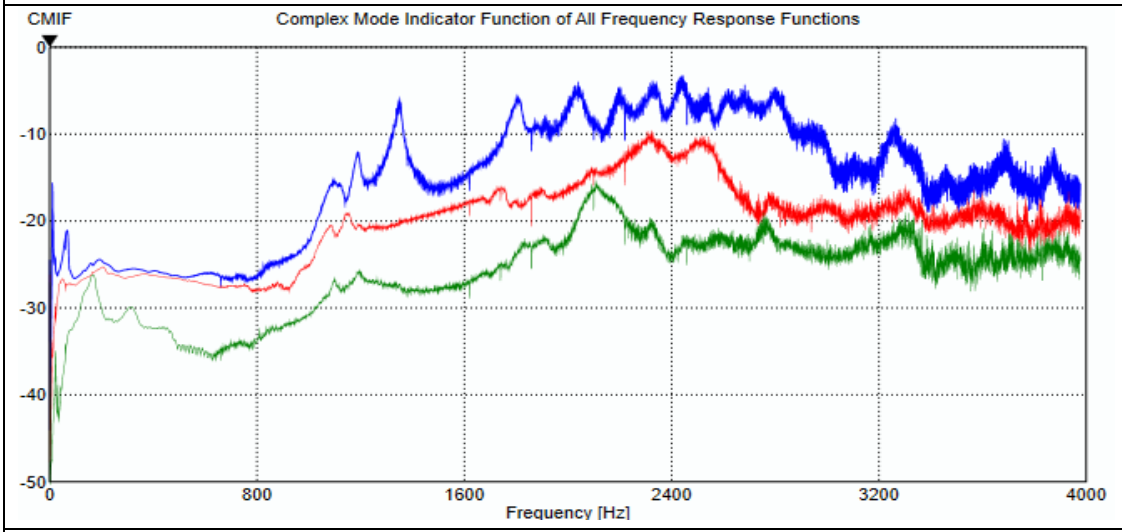
OMA – Basketball SSI-UPCx



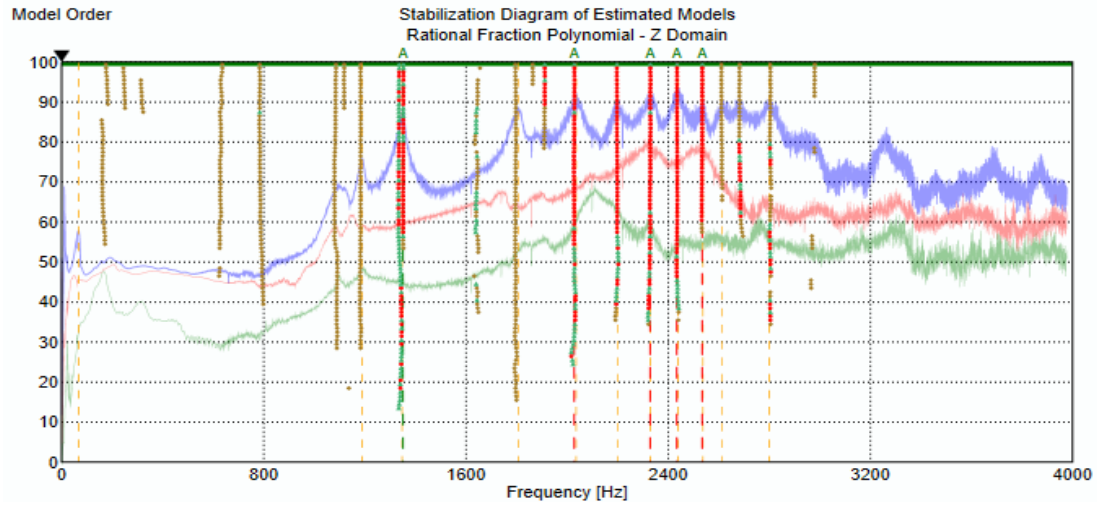
OMA-Basketball SVD plot from Matlab



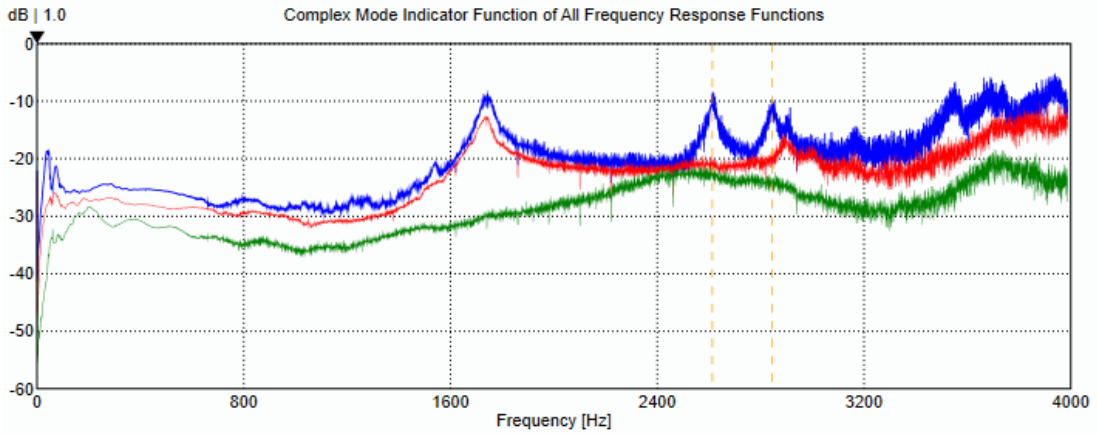
OMA-Basketball S1 over S2 plot from Matlab



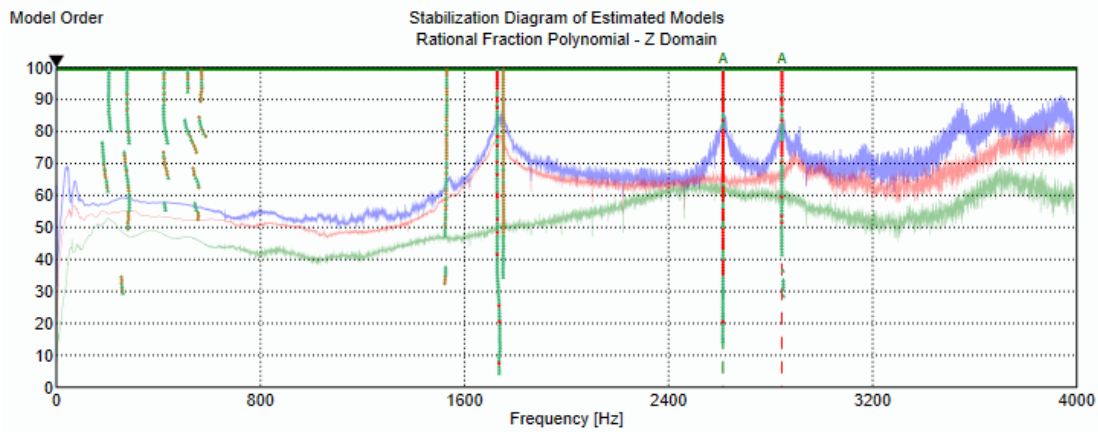
EMA – Hv CMIF



EMA – Hv RFPz



EMA – H1 CMIF



EMA – H1 RFPz

Extracted Modal Parameters

Note that each row of the table corresponds to frequencies within 5% of each other and follow the same general mode shape direction. They are assumed to represent to the same mode across estimators and experiments. Bolded black values represent those values confirmed through the Matlab S1 over S2 plots, within 5 Hz. Red values represent SSI estimates not visually present as a peak on the SVD plots.

Table B2: Combined estimator selection Table for block A

	Ambient			**Basketball**						**EMA Hv**						**EMA H1**					
	SSI-UPCx			EFDD			SSI-UPCX			CMIF			RFPz			CMIF			RFP-z		
	F (Hz)	ξ (%)	C (%)	F (Hz)	ξ (%)	C (%)	F (Hz)	ξ (%)	C (%)	F (Hz)	ξ (%)	C (%)	F (Hz)	ξ (%)	C (%)	F (Hz)	ξ (%)	C (%)	F (Hz)	ξ (%)	C (%)
1	59	8.99	8.26							66	2.25	42.55									
2							74	1.11	0.27							72	1.40	35.40			
3				**190**	**1.58**	**0.27**															
4				288	1.25	38.42	281	3.55	2.12												
5							999	61.46	37.71												
6				**1081**	**0.88**	**4.68**	1083	1.14	6.86												
7				**1126**	**0.85**	**9.16**				1101	0.18	79.08									
8							1131	2.54	7.08												
9				**1186**	**0.91**	**8.31**	1185	2.01	2.69	1188	0.72	53.00									
10										1347	0.75	4.97	1351	0.20	32.28						

	Ambient			**Basketball**						**EMA Hv**						**EMA H1**					
	SSI-UPCx			EFDD			SSI-UPCX			CMIF			RFPz			CMIF			RFP-z		
	F (Hz)	ξ (%)	C (%)	F (Hz)	ξ (%)	C (%)	F (Hz)	ξ (%)	C (%)	F (Hz)	ξ (%)	C (%)	F (Hz)	ξ (%)	C (%)	F (Hz)	ξ (%)	C (%)	F (Hz)	ξ (%)	C (%)
11				1688	0.57	1.96	1694	2.08	4.33							1541	0.33	59.38			
12				**1851**	**0.64**	**5.35**	1745	6.16	24.94	1809	0.22	56.10				1742	0.22	33.69			
13										2036	0.51	20.86	2028	0.65	17.29						
14				2183	0.51	46.29				2199	0.04	54.92									
15										2328	0.31	27.48	2329	0.36	36.35						
16										2439	0.24	24.29	2434	0.48	27.94						
17										2537	0.18	25.89	2535	0.28	16.81						
18										2614	0.14	67.97				2615	0.19	27.59	2613	0.33	26.21
19										2801	0.23	32.16				2844	0.08	38.35	2844	0.21	29.78
20				3339	0.65	16.98	3356	2.90	21.52												

Mode Shapes

The presentation of the mode shapes follows a naming convention as follows:

X1-X2-X3-X4

Where:

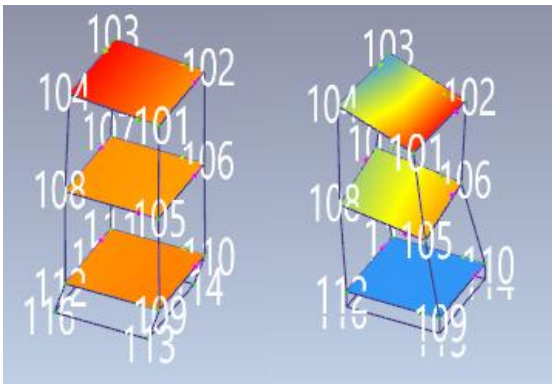
X1 is the block name.

X2 is the experiment type; Am for OMA Ambient, B for OMA Basketball. H1 and Hv are for EMA.

X3 is the method of analysis. EF for EFDD, x for UPCx, C for CMIF, z for RFPz.

X4 is the mode shape order as from the first column in the Extracted Data table.

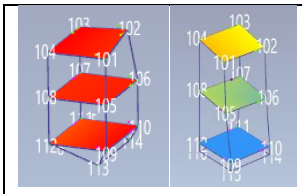
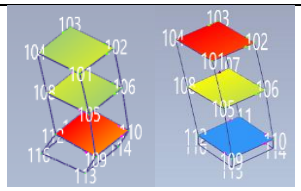
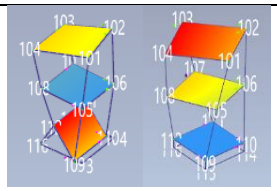
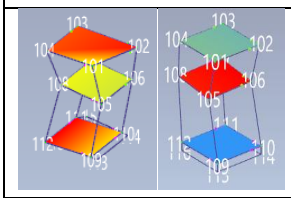
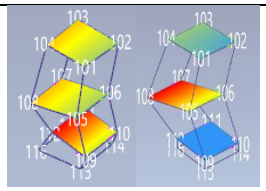
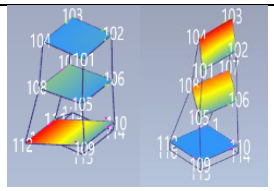
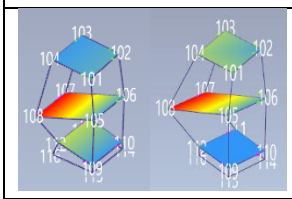
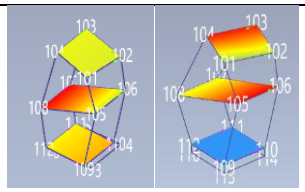
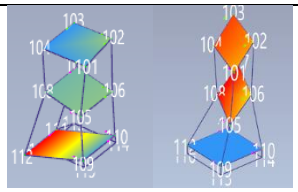
An example of the presentation of mode shapes is given for OMA – Ambient shape 1 whereby the Raw Shape (OG) is given to the left and the Fixed Shape (RBR) is provided to the right.

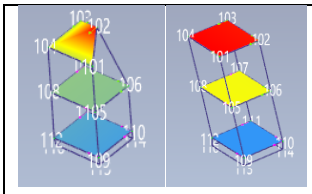
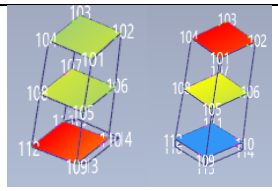
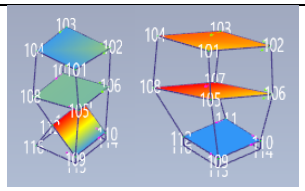
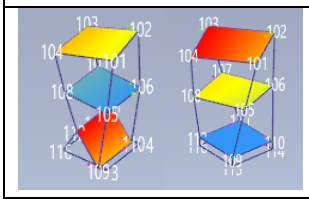
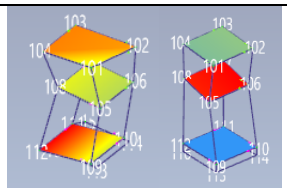
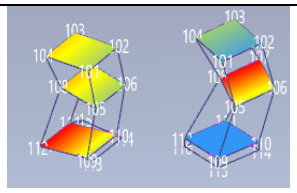
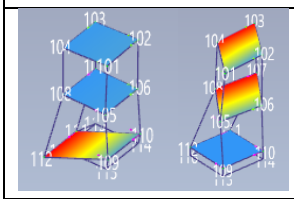
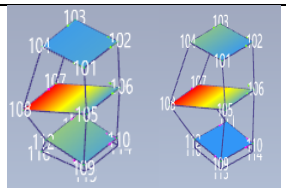
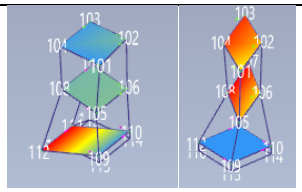


A-Am-x-1

OMA – Basketball

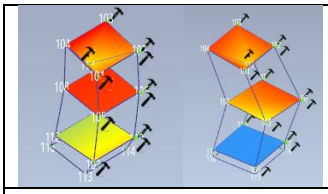
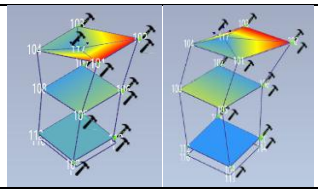
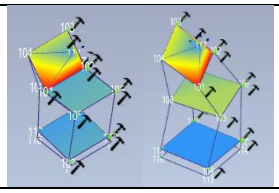
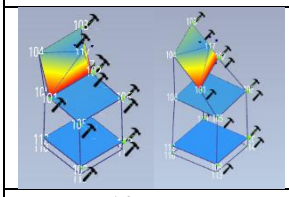
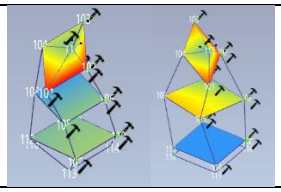
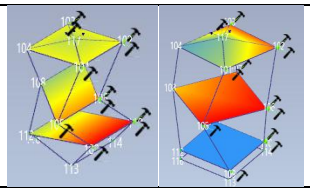
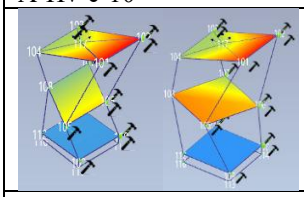
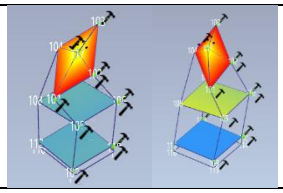
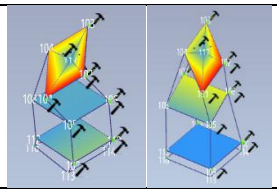
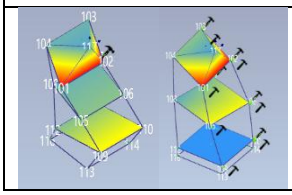
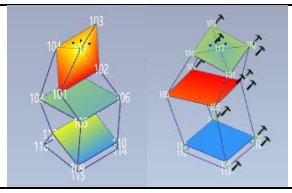
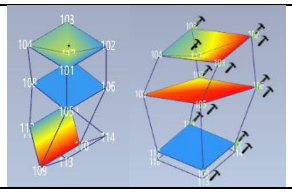
Table B3: Pre-selection of OMA Basketball mode shapes

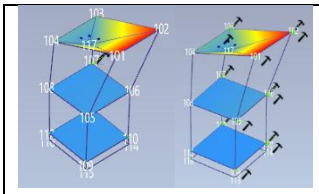
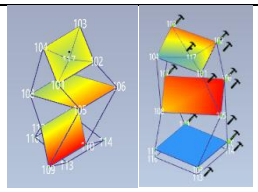
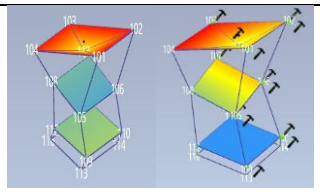
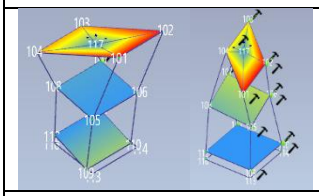
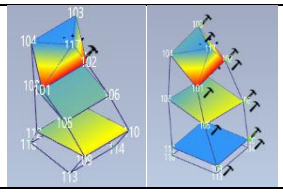
		
A-B-EF-3	A-B-EF-4	A-B-EF-6
		
A-B-EF-7	A-B-EF-9	A-B-EF-11
		
A-B-EF-12	A-B-EF-14	A-B-EF-20

		
A-B-x-2	A-B-x-4	A-B-x-5
		
A-B-x-6	A-B-x-8	A-B-x-9
		
A-B-x-11	A-B-x-12	A-B-x-20

EMA – Hv

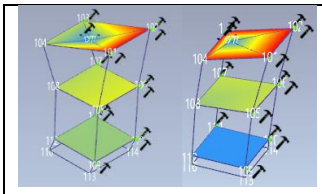
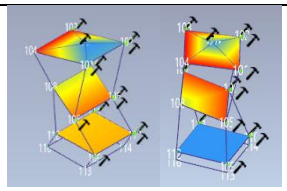
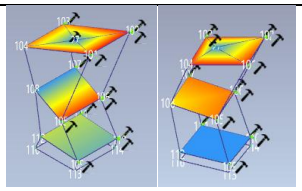
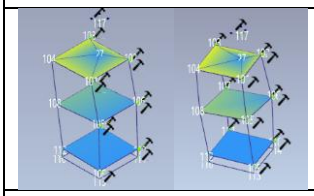
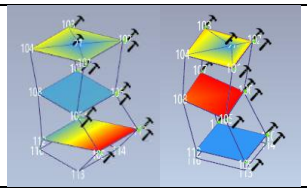
Table B4: Pre-selection of EMA – Hv Mode shapes

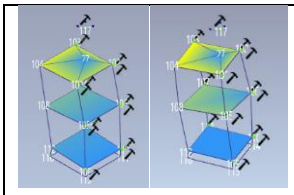
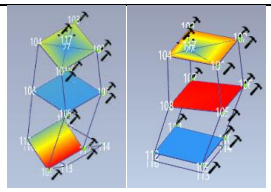
		
A-Hv-c-1	A-Hv-c-7	A-Hv-c-9
		
A-Hv-c-10	A-Hv-c-12	A-Hv-c-13
		
A-Hv-c-14	A-Hv-c-15	A-Hv-c-16
		
A-Hv-c-17	A-Hv-c-18	A-Hv-c-19

		
A-Hv-z-10	A-Hv-z-13	A-Hv-z-15
		
A-Hv-z-16	A-Hv-z-17	

EMA – H1

Table B5: Pre-selection of EMA H1 mode shapes

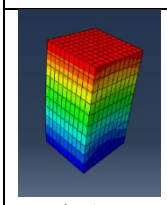
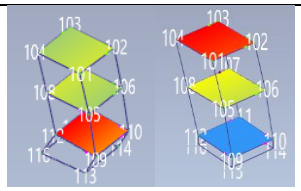
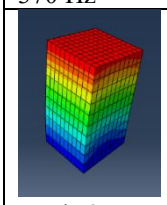
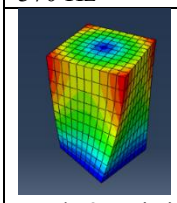
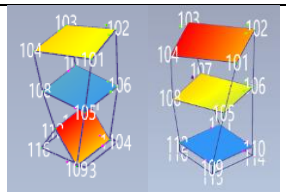
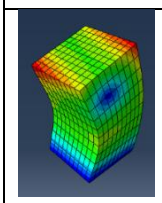
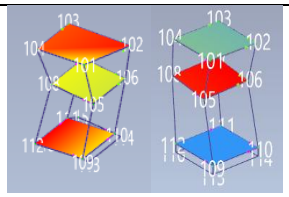
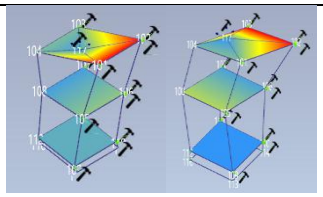
		
A-H1-c-2	A-H1-c-11	A-H1-c-12
		
A-H1-c-18	A-H1-c-19	

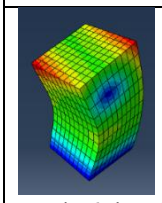
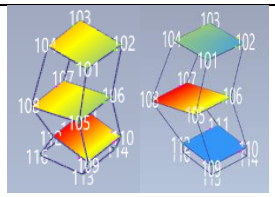
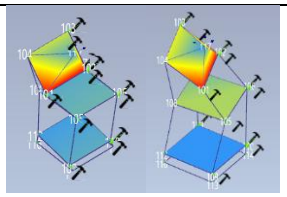
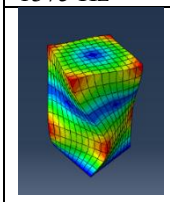
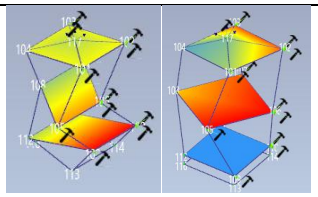
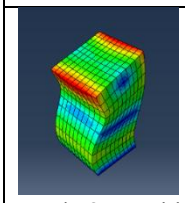
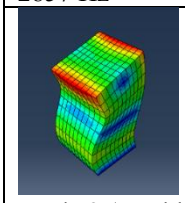
	
A-H1-z-18	A-H1-z-19

Selected Results

Note that mode 4: Axial Elongation and mode 10: Face Warping have been excluded. There are no reliable z axis measurements in the experiments to be able to confirm these modes.

Table B6: Selected mode Table

Target FE Mode Shape 30 GPa Model	OMA Shape and Ref. Frequency	EMA Shape and Ref. Frequency	Comments
 Mode 1: cantilever 370 Hz	 A-B-EF-4 288 Hz		
 Mode 2: cantilever (M) 370 Hz			
 Mode 3: twisting 750 Hz	 A-B-EF-6 1081 Hz		*low confidence because of higher-than-expected frequency and proximity to Mode 5.
 Mode 5: bending 1375 Hz	 A-B-EF-7 1126 Hz	 A-Hv-c-7 1101 Hz	

Target FE Mode Shape 30 GPa Model	OMA Shape and Ref. Frequency	EMA Shape and Ref. Frequency	Comments
 Mode 6: bending (M) 1375 Hz	 A-B-EF-9 1186 Hz	 A-Hv-c-9 1188 Hz	
 Mode 7: twisting 2247 Hz		 A-Hv-c-13 2036 Hz	Similar mode shapes are present around this one. This decreases the confidence of this mode for analysis.
 Mode 8: Double Bending 2857 Hz			
 Mode 9:(Double Bending (M) 2857 Hz			

Appendix C: Level 1 Data Table

This appendix holds the table of Level 1 modelling results. The table contains the set of eigenfrequencies for the specific block geometry used in this study on a stand-up configuration, for MOE in the range of 10 to 40 GPa in increments of 0.5 GPa. Mirror (degenerate) modes are highlighted in blue font. The MOE is highlighted in yellow. The back calculated compressive strength of concrete is also provided as reference.

Table C1: Level 1 Reference Data Table

Run Number	1	2	3	4	5	6	7	8	9	10	11
fc' (MPa) (CSA formula)	5	5	6	7	7	8	8	9	10	10	11
MOE (GPa)	10.0	10.5	11.0	11.5	12.0	12.5	13.0	13.5	14.0	14.5	15.0
EigenFreq 1	214	219	224	229	234	239	244	248	253	257	262
EigenFreq 2 - Mirror	214	219	224	229	234	239	244	248	253	257	262
EigenFreq 3	434	444	455	465	475	485	494	504	513	522	531
EigenFreq 4	729	747	765	782	799	815	831	847	863	878	893
EigenFreq 5	794	814	833	851	870	888	905	922	939	956	972
EigenFreq 6 - Mirror	794	814	833	851	870	888	905	922	939	956	972
EigenFreq 7	1298	1330	1361	1391	1421	1451	1479	1508	1535	1562	1589
EigenFreq 8	1649	1690	1730	1769	1807	1844	1881	1916	1952	1986	2020
EigenFreq 9 - Mirror	1649	1690	1730	1769	1807	1844	1881	1916	1952	1986	2020
EigenFreq 10	1861	1907	1952	1996	2039	2081	2122	2162	2202	2241	2279

Run Number	12	13	14	15	16	17	18	19	20	21
fc' (MPa) (CSA formula)	12	13	13	14	15	16	17	18	19	20
MOE (GPa)	15.5	16.0	16.5	17.0	17.5	18.0	18.5	19.0	19.5	20.0
EigenFreq 1	266	270	274	279	283	287	291	294	298	302
EigenFreq 2 - Mirror	266	270	274	279	283	287	291	294	298	302
EigenFreq 3	540	548	557	565	573	582	590	598	605	613
EigenFreq 4	908	922	936	951	964	978	992	1005	1018	1031
EigenFreq 5	988	1004	1020	1035	1050	1065	1080	1094	1109	1123
EigenFreq 6 - Mirror	988	1004	1020	1035	1050	1065	1080	1094	1109	1123
EigenFreq 7	1615	1641	1667	1692	1716	1741	1765	1789	1812	1835
EigenFreq 8	2053	2086	2119	2151	2182	2213	2243	2274	2303	2333
EigenFreq 9 - Mirror	2053	2086	2119	2151	2182	2213	2243	2274	2303	2333
EigenFreq 10	2317	2354	2390	2426	2462	2497	2531	2565	2599	2632

Run Number	22	23	24	25	26	27	28	29	30	31
fc' (MPa) (CSA formula)	21	22	23	24	25	26	27	28	30	31
MOE (GPa)	20.5	21.0	21.5	22.0	22.5	23.0	23.5	24.0	24.5	25.0
EigenFreq 1	306	310	313	317	320	324	327	331	334	338
EigenFreq 2 - Mirror	306	310	313	317	320	324	327	331	334	338
EigenFreq 3	621	628	636	643	650	657	665	672	679	685
EigenFreq 4	1044	1056	1069	1081	1094	1106	1118	1129	1141	1153
EigenFreq 5	1137	1150	1164	1178	1191	1204	1217	1230	1243	1255
EigenFreq 6 - Mirror	1137	1150	1164	1178	1191	1204	1217	1230	1243	1255
EigenFreq 7	1858	1880	1903	1925	1946	1968	1989	2010	2031	2052
EigenFreq 8	2362	2390	2418	2446	2474	2501	2528	2555	2582	2608
EigenFreq 9 - Mirror	2362	2390	2418	2446	2474	2501	2528	2555	2582	2608
EigenFreq 10	2664	2697	2729	2760	2791	2822	2853	2883	2913	2942

Run Number	32	33	34	35	36	37	38	39	40	41
fc' (MPa) (CSA formula)	32	33	35	36	37	39	40	42	43	44
MOE (GPa)	25.5	26.0	26.5	27.0	27.5	28.0	28.5	29.0	29.5	30.0
EigenFreq 1	341	344	348	351	354	357	361	364	367	370
EigenFreq 2 - Mirror	341	344	348	351	354	357	361	364	367	370
EigenFreq 3	692	699	706	712	719	725	732	738	745	751
EigenFreq 4	1164	1176	1187	1198	1209	1220	1231	1241	1252	1263
EigenFreq 5	1268	1280	1292	1305	1317	1328	1340	1352	1364	1375
EigenFreq 6 - Mirror	1268	1280	1292	1305	1317	1328	1340	1352	1364	1375
EigenFreq 7	2072	2092	2112	2132	2152	2171	2190	2210	2229	2247
EigenFreq 8	2634	2660	2685	2710	2735	2760	2785	2809	2833	2857
EigenFreq 9 - Mirror	2634	2660	2685	2710	2735	2760	2785	2809	2833	2857
EigenFreq 10	2972	3001	3029	3058	3086	3114	3142	3169	3196	3223

Run Number	42	43	44	45	46	47	48	49	50	51
fc' (MPa) (CSA formula)	46	47	49	51	52	54	55	57	59	60
MOE (GPa)	30.5	31.0	31.5	32.0	32.5	33.0	33.5	34.0	34.5	35.0
EigenFreq 1	373	376	379	382	385	388	391	394	397	400
EigenFreq 2 - Mirror	373	376	379	382	385	388	391	394	397	400
EigenFreq 3	757	763	769	776	782	788	793	799	805	811
EigenFreq 4	1273	1284	1294	1304	1314	1324	1334	1344	1354	1364
EigenFreq 5	1386	1398	1409	1420	1431	1442	1453	1464	1475	1485
EigenFreq 6 - Mirror	1386	1398	1409	1420	1431	1442	1453	1464	1475	1485
EigenFreq 7	2266	2285	2303	2321	2339	2357	2375	2393	2410	2427
EigenFreq 8	2881	2904	2927	2951	2973	2996	3019	3041	3064	3086
EigenFreq 9 - Mirror	2881	2904	2927	2951	2973	2996	3019	3041	3064	3086
EigenFreq 10	3250	3277	3303	3329	3355	3381	3406	3431	3457	3482

Run Number	52	53	54	55	56	57	58	59	60	61
fc' (MPa) (CSA formula)	62	64	66	68	69	71	73	75	77	79
MOE (GPa)	35.5	36.0	36.5	37.0	37.5	38.0	38.5	39.0	39.5	40.0
EigenFreq 1	402	405	408	411	414	416	419	422	425	427
EigenFreq 2 - Mirror	402	405	408	411	414	416	419	422	425	427
EigenFreq 3	817	823	828	834	840	845	851	856	862	867
EigenFreq 4	1374	1383	1393	1402	1412	1421	1430	1440	1449	1458
EigenFreq 5	1496	1506	1517	1527	1537	1548	1558	1568	1578	1588
EigenFreq 6 - Mirror	1496	1506	1517	1527	1537	1548	1558	1568	1578	1588
EigenFreq 7	2445	2462	2479	2496	2513	2529	2546	2562	2579	2595
EigenFreq 8	3108	3130	3151	3173	3194	3215	3236	3257	3278	3299
EigenFreq 9 - Mirror	3108	3130	3151	3173	3194	3215	3236	3257	3278	3299
EigenFreq 10	3506	3531	3555	3580	3604	3628	3651	3675	3699	3722

Curriculum Vitae

Candidate's full name: Dikshaiye Mathoora

Universities attended (with dates and degrees obtained): University of New Brunswick (B.Sc.E, 2020)

Publications: N/A.

Academic Awards:

2021-22 Esterbauer Civil Engineering Graduate Award

2020-21 Esterbauer Civil Engineering Graduate Award

2019-20 Rudy and Theresa Esterbauer Undergraduate Research Award

2019-20 Louis & Montoura Debly Undergraduate Scholarship

2019-20 Ken Vaughan Memorial Bursary

2019-20 J. Nairn McCaffrey Memorial Scholarship

2019-20 D. Malcolm Jeffrey Memorial Prize

2018-19 John S. Watt Memorial Scholarship

2018-19 J. Nairn McCaffrey Memorial Scholarship

2018-19 Edwin Jacob Special University Scholarship

2017-18 Robin W. Gough Scholarship in Civil Engineering

2017-18 John S. Watt Memorial Scholarship

2017-18 J. Nairn McCaffrey Memorial Scholarship

2017-18 H. E. McKeen Scholarship

2017-18 Charles S. Bennett Memorial Scholarship

2017-18 Allan K. Grimmer Prize

2016-17 UNB Scholarship for Academic Excellence